Vol.40 No.4 2016

Journal

JOURNAL OF THE MAGNETICS SOCIETY OF JAPAN

*Vol.*40 *No.*4 2016

Journal of the Magnetics Society of Japan
Vol. 40, No. 4

Electronic Journal URL: https://www.jstage.jst.go.jp/browse/msjmag

CONTENTS

<Letter>

Theoretical Investigation on Electronic and Magnetic Structures of FeRh

Hidekazu Takahashi, Masaaki Araidai*, Susumu Okada and Kenji Shiraishi*

Graduate School of Pure and Applied Sciences,University of Tsukuba, *1-1-1 Tennodai, Tsukuba, Ibaraki 305-8571, Japan*
*Institute of Materials and Systems for Sustainability, *Furo-cho, Chikusa-ku, Nagoya, 464-8603, Japan*

In order to clarify the mechanism behind antiferromagnetic (AFM)-ferromagnetic (FM) phase transition, we investigate the electronic and magnetic structures of FeRh by using first principles calculations with the GGA + U method. By choosing the appropriate values of the on-site Coulomb interaction (U) of Fe_{3d} and Rh_{4d} electrons, we succeed in explaining the reported AFM-FM phase transition experiments for the first time by obtaining the total energy difference between the AFM and FM states (ΔE). Other physical quantities such as the density of states (DOS) are also consistent with experimental reports.

Key words: magnetic refrigeration, inverse magnetocaloric material, antiferromagnetic-ferromagnetic phase transition, GGA + U method, on-site Coulomb interaction

1. Introduction

Room-temperature magnetic refrigeration technology using magnetocaloric materials (MCMs) has recently gained attention because it is expected to eliminate refrigerants that are greenhouse gases and improve the system efficiency of refrigerators.[1] Various performance-enhancing MCMs such as $La(Fe_xSi_{1-x})_{13}H_y$,[2] MnFe(P,Si),[3] and so on have been found so far. Inverse magnetocaloric materials (IMCMs) such as FeRh[4] and $Mn_{2-x}Cr_xSb$[5] have also been the focus of attention because of the appearance of the 'giant' inverse magnetocaloric effect (IMCE) under a low magnetic field. In particular, FeRh shows a first-order antiferromagnetic (AFM)-ferromagnetic (FM) phase transition at $T_{tr} \approx 320 \sim 370$ K without a magnetic field and exhibits a giant adiabatic temperature change ΔT_{ad} (= 13 K) under 1.95 T. Recent studies suggest that ΔT_{ad} can be increased up to 18 K per 1 T.[6] The appearance of new MCMs and IMCMs that are superior to FeRh is now expected. It is quite important to understand the why ΔT_{ad} is large in FeRh. Moreover, it is essential to clarify the microscopic mechanism behind the AFM-FM phase transition in order to develop new magnetocaloric materials.

Since FeRh was discovered by Fallot in 1938,[7] various experiments[8)-19)] on its physical parameters have been performed, such as the difference between the minimum total energy of the FM state and that of the AFM state (ΔE) related to T_{tr}.[10]

Various theoretical investigations have also been carried out. For example, Kittel proposed the exchange inversion model.[20] There have also been various theories proposed. However, all of these currently remain the subject of debate. Several investigations into electronic and magnetic structures using various band-structure calculation methods have been reported to date.[21)-28)] We should point out here that recent advanced first-principles calculations[26)-28)] are not able to reproduce important physical quantities such as ΔE. In particular, if ΔE calculations are inconsistent with

experiments, its mechanism as an IMCM cannot be clarified. Generally, in alloys containing 3d and 4d transition metals, regard for electronic correlation is known to be important. However, this is not considered in all of the reported calculations, including Refs. (26)-(28). Therefore, we treat this electronic correlation as the on-site Coulomb interaction (U) and examine the effect of U on various physical quantities, particularly ΔE. In this paper, we investigate the electronic and magnetic structures of FeRh and have succeeded in reproducing the AFM-FM phase transition quantitatively for the first time.

2. Calculation Method

In FeRh, which is a CsCl crystal with a simple cubic structure, the magnetic structures in the AFM and FM states are shown in Fig. 1. In order to treat FeRh in both the AFM and FM states, the crystal is considered a face-centered cubic structure with lattice constant $a' = 2a$, where a is the lattice constant in the case of a simple cubic structure. The atomic positions of two Fe atoms are (0.0, 0.0, 0.0) and (0.5a', 0.5 a', 0.5 a'). The atomic positions of two Rh atoms are (0.25 a', 0.25 a', 0.25 a') and (0.75 a', 0.75 a', 0.75 a').
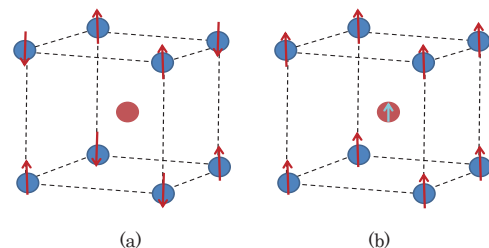

Fig. 1 Magnetic structure of (a) AFM and (b) FM states of FeRh. The blue and violet circles indicate Fe and Rh atoms, respectively. ↑ and ↓ indicate the directions of the magnetic moments.

The Vienna *ab initio* simulation package (VASP) [29),30)] with the projector augmented wave (PAW) method[31),32)] was utilized for performing the first principles

calculations. We used the Perdew-Burke-Ernzerhof exchange-correlation functional[33] with the Hubbard U method (GGA + U)[34] including U and the exchange parameter (J) for each atomic orbital in the materials, as our GGA calculation results such as ΔE (= 31.5 meV/atom) and the magnitude relation of Fe magnetic moment values between the AFM and FM states (3.12µB, 3.18µB) were inconsistent with experimental results. In the calculations, the Dudarev approach, which is only dependent on $U_{eff} = U - J$[35], was adopted. The magnitude of U and J for the Fe3d electron (U_{Fe}, J_{Fe}) and for the Rh4d electron (U_{Rh}, J_{Rh}) were set to (2.0 eV, 1.0 eV) and (1.95 eV, 1.0 eV), respectively so that the obtained physical quantities of the Fe and Rh crystals (lattice constant, bulk modulus and density of states (DOS)) using these U and J were consistent with the reported experiments. The Methfessel-Paxton method[36] was adopted by choosing the width of the smearing $\Delta\sigma$ = 0.05 eV. A plane-wave basis set with an energy cutoff (E_{cut}) of 830 eV and an 11×11×11 Monkhorst-Pack k points mesh[37] was used.[38]

3. Results and Discussion

A comparison of the physical quantities obtained in the present analysis by using the above GGA + U calculation method and those reported in experiments is given in Table I. The calculation results are detailed as follows. First, the relationship between the total energies of the AFM and FM states and the lattice constant is investigated by choosing appropriate magnitudes of U_{Fe} and U_{Rh} to estimate ΔE. The obtained results are shown in Fig. 2. As shown, the AFM state is stable when the lattice constant is small. With increasing the lattice constant, the total energy of the AFM state has a minimum at lattice constant (a_{AFM}) (= 2.99 Å) and the total energy difference between the AFM and FM states becomes smaller. When the lattice constant is increased further, the total energy of the FM state has a minimum at lattice constant (a_{FM}) (= 3.01 Å). Finally, the FM state becomes stable. The obtained values for a_{AFM} and a_{FM} are consistent with the experiment (a_{AFM} = 2.981 Å and a_{FM} = 2.999 Å).[9] It is noted that the obtained value for ΔE (= 2.71 meV/atom)
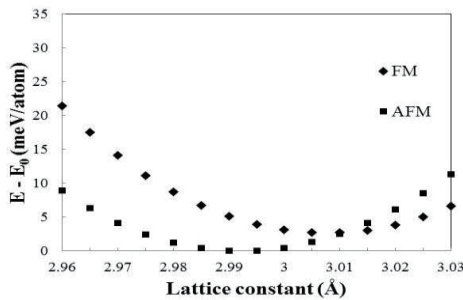

Fig. 2 Total energy versus lattice constant. On the basis of the minimum of the AFM state, the closed squares and the diamonds indicate the total energies of the AFM and the FM states, respectively.

is consistent with the experimental value ΔE (= 2.80 meV/atom).[10]

The other physical quantities that were obtained are detailed as follows. The magnetic moments of the Fe and Rh atoms (m_{Fe}, m_{Rh}) in the AFM and FM states are investigated. The obtained magnetic moments are almost identical to those in the experiments.[11] The obtained m_{Fe} of the AFM state (= 3.31µB) becomes equal to m_{Fe} of the FM state (= 3.31µB), which is slightly different from the tendency obtained by the experiment (m_{Fe} of the AFM state > m_{Fe} of the FM state). In all of the reported calculations[21]-[28], the relationship whereby m_{Fe} of the AFM state < m_{Fe} of the FM state is satisfied. However, in the present work, the magnitude relation of the obtained m_{Fe} values between the AFM and FM states is approaching that of the experiment.

The obtained relationship between the obtained values of m_{Fe} and m_{Rh} of the AFM and FM states and the lattice constant is shown in Fig. 3. With increasing the lattice constant, (i) the change in m_{Fe} is much larger than that in m_{Rh}, (ii) the change in m_{Fe} in the AFM state is larger than that in the FM state, and (iii) the magnitude relation of m_{Fe} values between the AFM and FM states is reversed near the observed lattice constant.
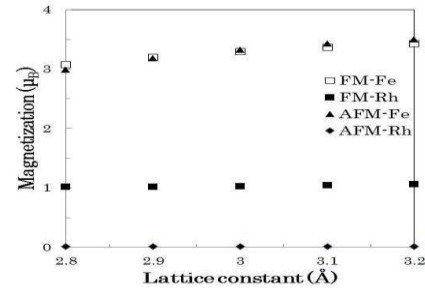
Fig. 3 m_{Fe} and m_{Rh} of the AFM and FM states versus lattice constant.

The critical magnetic field at 0 K ($H_c(0)$) which can provide us with useful information to understand the IMCE of FeRh can be obtained by[22]

$$H_c(0) = \Delta E / (M_{FM} - M_{AFM}), \qquad (1)$$

where M_{FM} and M_{AFM} (= 0 µB) are the magnetization per atom of the FM and AFM states, respectively. The obtained $H_c(0)$ (= 21.6 T) is consistent with the experiments (= 21.2 T ~ 29.7 T).[12],[13],[14] The DOS and the partial density of states (PDOS) near the Fermi level (E_F) of the Fe and Rh atoms of the FM and AFM states were investigated and are shown in Figs. 4(a)-(d) and Figs. 5(a)-(d), respectively. The distribution of DOS near E_F of the FM state shown in Figs. 4(a) and (b) and of the AFM state shown in Figs. 4(c) and (d) are similar to the reported photoemission spectra.[15],[16] In particular, the main peak positions of DOS near E_F are around −5.0 eV to −4.0 eV and around −3.0 eV to −2.0 eV. Moreover, the obtained ratio of DOS at E_F of the FM state and that of the AFM state ($D(E_F)_{FM}$ / $D(E_F)_{AFM}$) (= 4.72) is also consistent with the experiments.[17],[18] The reason the obtained value of $D(E_F)_{FM}$ / $D(E_F)_{AFM}$ is large

is examined by using PDOSs, as shown in Figs. 5(a)-(d), respectively. PDOS at E_F ($PD(E_F)$) of a Fe atom of the FM state for the minority spin state is much higher than that of the AFM state for the minority spin state, while $PD(E_F)$ of an Fe atom for both the AFM and FM states for the majority spin state is low and $PD(E_F)$ of an Rh atom of both the AFM and FM states for the majority spin and minority spin state are also low. Therefore, $D(E_F)_{FM}$ / $D(E_F)_{AFM}$ becomes large due to the large change in the contribution of Fe$_{3d}$ electrons to $D(E_F)$ in the AFM-FM phase transition.

The effect of U on ΔE and m_{Fe} in the AFM and FM states is investigated using PDOS. Comparing Fig. 5(b) with Fig. 5(d), magnetic states of Rh for the AFM and FM states are nonmagnetic and FM states, respectively. When the magnitude of U_{Rh} is increased to 1.95 eV, the nonmagnetic state becomes unstable and the FM state is energetically advantageous. As a result, ΔE becomes smaller compared with the GGA calculation result. From Fig. 5(a) and (c), we can see that the Fe$_{3d}$ band in the majority spin state for the AFM and FM states is almost filled, while that in the minority spin state for the AFM and FM states is inadequately filled. Similar results (not shown) were obtained by the GGA calculation. When the magnitude of U_{Fe} is increased to 2.0 eV, Fe$_{3d}$ band at E_F in the minority spin state moves to the upper energy side, which results in a decrease of the occupied Fe$_{3d}$ PDOS in the minority spin state. This leads to an increase of m_{Fe} in the AFM and FM states and improvement of the magnitude relation of $m_{F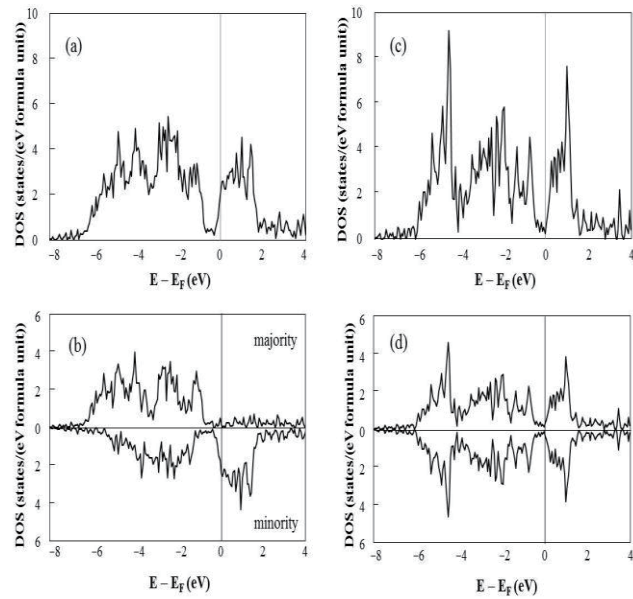e}$ values between the AFM and FM states. From the above results, the effect of U plays a crucial role in discussing the AFM-FM phase transition.

Fig. 4 DOS near E_F of (a) the FM state, (b) the FM state for both the majority spin and the minority spin states, (c) the AFM state, and (d) the AFM state for each of the majority spin and the minority spin states.
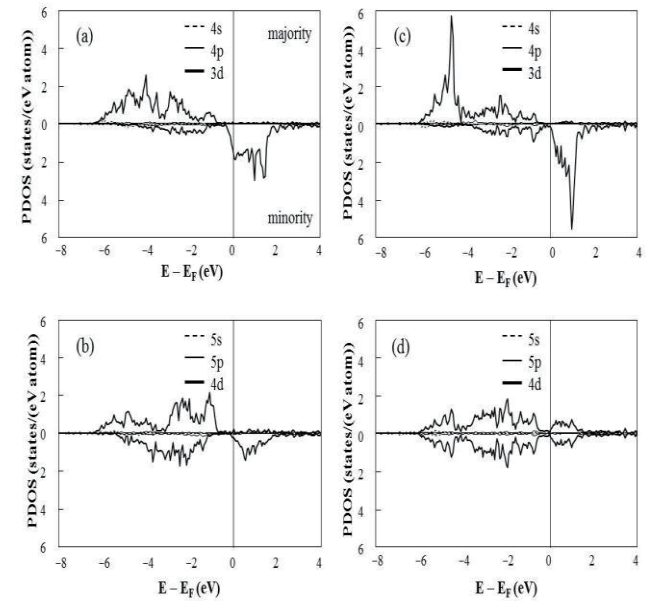
Fig. 5 PDOS near E_F of (a) an Fe atom of the FM state, (b) an Rh atom of the FM state, (c) an Fe atom of the AFM state and (d) an Rh atom of the AFM state.

Table I Comparison of physical quantities obtained in the present analysis using the GGA+U method and those reported in experiments.

	AFM a_{AFM} Å	FM a_{FM} Å	ΔE meV	AFM m_{Fe} μB	AFM m_{Rh} μB	FM m_{Fe} μB	FM m_{Rh} μB	$H_c(0)$ T	$D(E_F)_{FM}$ / $D(E_F)_{AFM}$	γ_{FM}/γ_{AFM}[i]	AFM B_{AFM}[ii] GPa	FM B_{FM}[iii] GPa
present work	2.99	3.01	2.71	3.31	0	3.31	1.04	21.6	4.72		195.7	210.6
Ref. (8)	2.987	2.997										
Ref. (9)	2.981	2.999										
Ref. (10)			2.80							2.41	142±14	133±20
Ref. (11)				3.30	0	3.17	0.97					
Ref. (12)								23.4				
Ref. (13)								29.7				
Ref. (14)								21.2				
Ref. (17)										3.75		
Ref. (18)										5.95		
Ref. (19)											142	158

i) Ratio of Sommerfeld coefficient γ of the FM state and that of the AFM state (γ_{FM}/γ_{AFM}),
ii) Bulk modulus of the AFM state (B_{AFM}), iii) Bulk modulus of the FM state (B_{FM})

The band structures of the AFM and FM states are investigated and are shown in Figs. 6(a)-(c), respectively. The two band structures are considerably different. In particular, in the FM state, the number of branches crossing the Fermi surface in the minority spin state is higher than that in the majority spin state. In the AFM state, a hole pocket appears at the center of the Γ point.
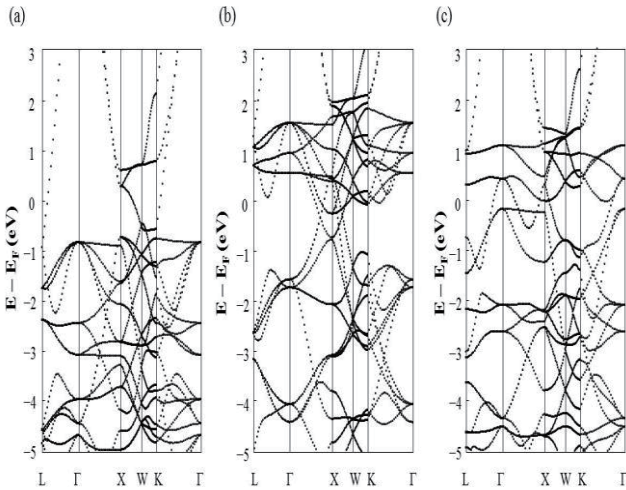
Fig. 6 Obtained band structures of (a) the FM state for the majority spin state, (b) the FM state for the minority spin state, and (c) the AFM state.

4. Conclusion

In summary, the electronic and magnetic structures of FeRh are investigated by using first principles calculations including appropriately chosen values of U for the Fe$_{3d}$ and Rh$_{4d}$ electrons, and we succeed in explaining the reported AFM-FM phase transition experiments for the first time by obtaining ΔE consistent with the experimental reports, also for the first time. Moreover, other obtained physical quantities are also consistent with the experimental reports. We will attempt to clarify the mechanism behind the AFM-FM phase transition by using the knowledge obtained in the present analysis.

References

1) K. G. Sanderman: *Scripta Mater.*, **67**, 566 (2012).
2) A. Fujita, S. Fujieda, Y. Hasegawa, and K. Fukamichi: *Phys. Rev. B*, **67**, 104416 (2003).
3) N. H. Dung, Z. Q. Ou, L. Caron, L. Zhang, D. T. C. Thanh, G. A. de Wijs, R. A. de Groot, K. H. J. Buschow, and E. Brück: *Adv. Energy Mater.*, **1**, 1215 (2011).
4) M. P. Annaorazov, K. A. Asatryan, G. Myalikgulyev, S. A. Nikitin, A. M. Tishin, and A. L. Tyurin: *Cryogenics,* **32**, 867 (1992).
5) L. Caron, X. F. Miao, J. C. P. Klaasse, S. Gama, and E. Brück: *Appl. Phys. Lett.*, **103**, 112404 (2013).
6) A. M. Tishin and Y. I. Spichkin: *Int. J. Refrig.*, **37**, 223 (2014).
7) M. Fallot: *Ann. Phys.*, **10**, 291 (1938).
8) A. I. Zakharov, A. M. Kadomtseva, R. Z. Levitin, and E. G. Ponyatovskii: *Sov. Phys. JETP*, **19**, 1348 (1964).
9) T. Miyanaga, T. Itoga, T. Okazaki, and K. Nitta: *J. Phys. Conf. Ser.*, **190**, 012097 (2009).
10) D. W. Cooke, F. Hellman, C. Baldasseroni, C. Bordel, S. Moyerman, and E. E. Fullerton: *Phys. Rev. Lett.*, **109**, 255901 (2012).
11) G. Shirane, R. Nathans, and C. W. Chen: *Phys. Rev.*, **134**, A1547 (1964).
12) J. B. McKinnon, D. Melville, and E. W. Lee: *J. Phys. C*, **3**, S46 (1970).
13) B. K. Ponomarev: *Sov. Phys. JETP*, **36**, 105 (1973).
14) T. Zhou, M. K. Cher, L. Shen, J. F. Hu, and Z. M. Yuan: *Phys. Lett. A*, **377**, 3052 (2013).
15) J.-S. Lee, E. Vescovo, L. Plucinski, C. M. Schneider, and C.-C. Kao: *Phys. Rev. B*, **82**, 224410 (2010).
16) A. X. Gray, D. W. Cooke, P. Krüger, C. Bordel, A. M. Kaiser, S. Moyerman, E. E. Fullerton, S. Ueda, Y. Yamashita, A. Gloskovskii, C. M. Schneider, W. Drube, K. Kobayashi, F. Hellman, and C. S. Fadley: *Phys. Rev. Lett.*, **108**, 257208 (2012).
17) P. Tu, A. J. Heeger, J. S. Kouvel, and J. B. Comly: *J. Appl. Phys.*, **40**, 1368 (1969).
18) J. Ivarsson, G.R. Pickett, and J. Tóth: *Phys. Lett. A*, **35**, 167 (1971).
19) J. A. Ricodeau and D. Melville: *J. Phys. F*, **2**, 337 (1972).
20) C. Kittel: *Phys. Rev.*, **120**, 335 (1960).
21) V. L. Moruzzi and P. M. Marcus: *Phys. Rev. B*, **46**, 2864 (1992).
22) V. L. Moruzzi and P. M. Marcus: *Solid State Commun.*, **83**, 735 (1992).
23) A. Szajek and J. A. Morkowski: *Physica B*, **193**, 81 (1994).
24) M. E. Gruner, E. Hoffmann, and P. Entel: *Phys. Rev. B*, **67**, 064415 (2003).
25) R. Y. Gu and V. P. Antropov: *Phys. Rev. B*, **72**, 012403 (2005).
26) L. M. Sandratskii and P. Mavropoulos: *Phys. Rev. B*, **83**, 174408 (2011).
27) Y. Kaneta, S. Ishino, Y. Chen, S. Iwata, and A. Iwase: *Jpn. J. Appl. Phys.*, **50**, 105803 (2011).
28) A. Deák, E. Simon, L. Balogh, L. Szunyogh, M. dos Santos Dias, and J. B. Staunton: *Phys. Rev. B*, **89**, 224401 (2014).
29) G. Kresse and J. Furthmüller: *Comput. Mat. Sci.*, **6**, 15 (1996).
30) G. Kresse and J. Furthmüller: *Phys. Rev. B*, **54**, 11169 (1996).
31) P. E. Blöchl: *Phys. Rev. B*, **50**, 17953 (1994).
32) G. Kresse and D. Joubert: *Phys. Rev. B*, **59**, 1758 (1999).
33) J. P. Perdew, K. Burke, and M. Ernzerhof: *Phys. Rev. Lett.*, **77**, 3865 (1996).
34) V. I. Anisimov, J. Zaanen, and O.K. Andersen: *Phys. Rev. B*, **44,** 943 (1991).
35) S. L. Dudarev, G. A. Botton, S. Y. Savrasov, C. J. Humphreys, and A. P. Sutton: *Phys. Rev. B*, **57**, 1505 (1998).
36) M. Methfessel and A. T. Paxton: *Phys. Rev. B*, **40**, 3616 (1989).
37) H. J. Monkhorst and J. D. Pack: *Phys. Rev. B*, **13**, 5188 (1976).
38) ΔE obtained with E_{cut} 830 eV and an 11×11×11 mesh is compared with that obtained with E_{cut} 680 eV and an 11×11×11 mesh. The difference in ΔE for the two conditions is less than 0.01 meV. ΔE obtained with E_{cut} 830 eV and an 11×11×11 mesh is compared with that obtained with E_{cut} 830 eV and a 15×15×15 mesh. The difference in ΔE for the two conditions is about 0.1 meV.

<Paper>

Model Calculation Considering Recording Time Window for Heat-Assisted Magnetic Recording

T. Kobayashi and Y. Fujiwara

Graduate School of Engineering, Mie Univ., *1577 Kurimamachiya-cho, Tsu 514-8507, Japan*

We improve our model calculation for heat-assisted magnetic recording (HAMR) by introducing the concept of the recording time window proposed in the micromagnetic calculation. The improved model calculation includes all the equations for the HAMR conditions used in the previous model. The difference is the introduction of the recording time window to determine the composition of the medium and the writing field. This improvement means that the results obtained using the model calculation become consistent with those obtained using a micromagnetic calculation. The minimum anisotropy constant ratio of the medium at 2, 3, and 4 Tbpsi can be determined using the improved model calculation.

Key words: heat-assisted magnetic recording, model calculation, recording time window, areal density, anisotropy constant ratio

1. Introduction

Heat-assisted magnetic recording (HAMR) is a recording method in which the medium is heated to reduce coercivity during the writing period. HAMR has been studied with the aim of solving the trilemma problem[1] of magnetic recording (MR). In most cases, a micromagnetic calculation is used for the HAMR design. A feature of the micromagnetic calculation is its precise simulation based on the actual situation. On the other hand, this calculation requires a long time, and it is sometimes difficult to grasp the physical implications of the obtained results.

We have reported a design method that uses a model calculation for the HAMR design[2] of 4 Tbpsi in order to shorten the calculation time and grasp the physical implications. In that paper, we revealed the complex relationship between certain design parameters and the anisotropy constant ratio K_u / K_{bulk} that we introduced. K_u / K_{bulk} is the intrinsic ratio of medium anisotropy constant K_u to bulk K_u. It is necessary to design a medium with a smaller K_u / K_{bulk} in terms of achieving good media productivity. We have subsequently improved our design method, and revealed the relationships between the many design parameters and K_u / K_{bulk} [3]. Then, we applied the physical implications to the many design parameters using our model calculation.

Our model calculation has a problem in that the minimum K_u / K_{bulk} value cannot be obtained at 2 Tbpsi. The reason is that the Curie temperature T_c approaches the writing temperature T_w as the areal density decreases in previous calculations[2, 3] since the grain volume increases. A certain time is necessary during cooling from T_c to T_w. The recording time window τ_{RW} proposed in the micromagnetic calculation[4] is a time during cooling from T_c to T_w. It is reported that a τ_{RW} value of around 0.1 ns is suitable for the micromagnetic calculation[4]. In this

study, we improve our model calculation by introducing τ_{RW}, and we fix τ_{RW} to 0.1 ns. This improvement means that the results obtained using the model calculation become consistent with those obtained using the micromagnetic calculation. Then, we provide the dependence of K_u / K_{bulk} on the areal density.

2. Previous Model Calculation

The medium was assumed to be granular. The arrangement of the grains was not considered.

The HAMR design procedure for obtaining the minimum K_u / K_{bulk} value using the previous model calculation is shown in Fig. 1. First, $K_u / K_{bulk} = 1$ and the design parameters are set. Then, the composition of the medium and the writing field H_w are determined using the equation:

$$K_{\beta+}(T_w, H_w) = TSF_w, \tag{1}$$

where

$$K_{\beta+}(T_w, H_w) = \frac{K_{um}(T_w)V_m}{kT_w}\left(1 + \frac{H_w}{H_{cm}(T_w)}\right)^2 \tag{2}$$

is the medium thermal stability factor[3] (K_{um}: mean anisotropy constant, V_m: grain volume for mean grain size D_m, k: Boltzmann constant, H_{cm}: mean coercivity assumed to be equal to mean anisotropy field $2K_{um}/M_s$, M_s: magnetization), and

$$TSF_w = TSF(\tau_w, n, \sigma_D, \sigma_K) \tag{3}$$

is the statistical thermal stability factor[5] ($\tau_w = d_B / v$: writing period, d_B: bit pitch, v: linear velocity n: grain number per bit, σ_D: standard deviation of grain size, σ_K: standard deviation of anisotropy). TSF_w is calculated statistically using many bits and grain-error probability

$$P = 1 - \exp\left(-f_0\tau_w \exp\left(-\text{TSF}_w \cdot \left(\frac{D}{D_m}\right)^2 \cdot \frac{K_u}{K_{um}}\right)\right) \quad (4)$$

($f_0 = 10^{11}$ s^{-1}: attempt frequency, D: grain size, K_u: anisotropy constant) with a 10^{-3} bit error rate.

The compositions of the medium and H_w are determined using Eq. (1). This means that writing completion is defined as the state in which the written bit is stable at T_w under H_w during τ_w for the medium with n, σ_D, and σ_K.

Next, four HAMR conditions I, II, III, and IV are examined. If there are margins for all four conditions, K_u/K_{bulk} can be reduced. When one of the four conditions reaches the limit, the minimum K_u/K_{bulk} value can be determined, and that condition becomes a limiting factor[3].

Condition I, which is the information (written bits) stability during 10 years of archiving, is expressed by

$$\frac{K_{um}(T_a)V_m}{kT_a} \geq \text{TSF}_{10}, \quad (5)$$

where T_a is the maximum working temperature of the hard drive, and TSF_{10} is the statistical thermal stability factor during 10 years of archiving TSF(10 years, n, σ_D, σ_K).

Condition II, which is the information stability on the trailing side located 1 bit from the writing position during writing, is expressed by

$$\frac{\Delta T}{\Delta x} = \frac{T_w - T_{rec}}{\Delta x} \leq \frac{\partial T}{\partial x}, \quad (6)$$

where $\Delta T/\Delta x$ is the medium thermal gradient for the down-track direction, which is the minimum thermal gradient required by the medium for information stability, T_{rec} is the maximum temperature at which the information on the trailing side located 1 bit from the writing position can be held during writing, and $\partial T/\partial x$ is the heat-transfer thermal gradient for the down-track direction, which is calculated by a heat-transfer simulation.

Condition III, which is the information stability in adjacent tracks during rewriting, is expressed by

$$\frac{\Delta T}{\Delta y} = \frac{T_w - T_{adj}}{\Delta y} \leq \frac{\partial T}{\partial y}, \quad (7)$$

where $\Delta T/\Delta y$ is the medium thermal gradient for the cross-track direction, T_{adj} is the maximum temperature at which the information in adjacent tracks can be held during rewriting, and $\partial T/\partial y$ is the heat-transfer thermal gradient for the cross-track direction.

Condition IV, which is the information stability under the main pole during rewriting, is expressed by

$$H_{adj} \geq H_w, \quad (8)$$

where H_{adj} is the maximum head field that can hold the information under the main pole during rewriting.

Conditions II and III can be combined as

$$\frac{\Delta T}{\Delta x} = \frac{\Delta T}{\Delta y} \leq \frac{\partial T}{\partial x} = \frac{\partial T}{\partial y}, \quad (9)$$

since $\partial T/\partial x \approx \partial T/\partial y$. Condition IV has margins for all the cases we examined. Therefore, the major limiting factors in the design are condition I given by Eq. (5) (I. $K_{um}(T_a)V_m/kT_a \geq \text{TSF}_{10}$) and conditions II and III given by Eq. (9) (hereafter, $\Delta T/\Delta x = \Delta T/\Delta y$, $\partial T/\partial x = \partial T/\partial y$, and Eq. (9) are expressed as $\Delta T/\Delta x(y)$, $\partial T/\partial x(y)$, and $\Delta T/\Delta x(y) \leq \partial T/\partial x(y)$, respectively).

When the areal density is 2 Tbpsi, V_m becomes large, and the Curie temperature T_c approaches T_w. Then, the calculation cannot be carried out, and this also arises a problem from a physical point of view. A certain time is necessary during cooling from T_c to T_w.
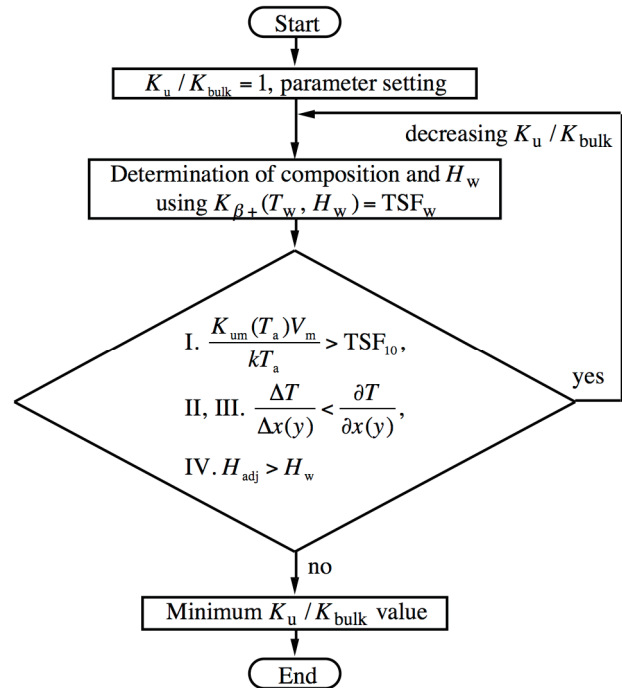
Fig. 1 HAMR design procedure for obtaining the minimum anisotropy constant ratio K_u/K_{bulk} using a previous model calculation.

3. Improved Model Calculation

3.1 Recording time window

We introduce the concept of the recording time window[4] τ_{RW} proposed in the micromagnetic calculation for the purpose of improving our model calculation.

First, we examine the physical implication of τ_{RW}. The magnetization M_s reversal number during a time τ is given by

$$f_0\tau \exp(-K_\beta), \quad (10)$$

where K_β is the medium thermal stability factor. When $\tau = 1/f_0 = 10^{-11}$ s $= 0.01$ ns, Eq. (10) becomes

$$\exp\left(-K_\beta\right). \tag{11}$$

Equation (11) is the M_s reversal probability for each attempt. For example, when $K_\beta = 0$, $\exp\left(-K_\beta\right)$ becomes one, where the M_s reversal always occurs for each attempt. $K_{\beta+}$ where M_s is parallel to H_w, and $K_{\beta-}$ where M_s is antiparallel to H_w are expressed by

$$K_{\beta+}(T, H_w) = \frac{K_{um}(T)V_m}{kT}\left(1 + \frac{H_w}{H_{cm}(T)}\right)^2, \tag{12}$$

and

$$K_{\beta-}(T, H_w) = \frac{K_{um}(T)V_m}{kT}\left(1 - \frac{H_w}{H_{cm}(T)}\right)^2 \quad \left(H_w \le H_{cm}(T)\right),$$

$$K_{\beta-}(T, H_w) = 0 \quad \left(H_{cm}(T) < H_w\right), \tag{13}$$

respectively. Therefore, the probability for each attempt where M_s and H_w change from parallel to antiparallel is expressed by

$$\exp\left(-K_{\beta+}\right). \tag{14}$$

On the other hand,

$$\exp\left(-K_{\beta-}\right) \tag{15}$$

is the probability for each attempt where M_s and H_w change from antiparallel to parallel.

In this paper, τ_{RW} is defined by

$$\tau_{RW} = \frac{T_c - T_w}{(\partial T/\partial x)\cdot v}, \tag{16}$$

where v is the linear velocity. Since $v = \partial x/\partial t$, $(\partial T/\partial x)\cdot v$ is the cooling rate $\partial T/\partial t$. Therefore, τ_{RW} is the cooling time from T_c to T_w. Then, the relationship between H_w and T_w is defined by

$$H_w = H_{cm}(T_w) = \frac{2K_{um}(T_w)}{M_s(T_w)}. \tag{17}$$

From this definition, the probability $\exp\left(-K_{\beta-}\right)$ is always equal to one during the cooling time τ_{RW}.

Figure 2 shows the dependence of the magnetization reversal probability on time. The calculation conditions and parameters are the same as those reported elsewhere[2, 3]. The closed circles are the probabilities for each attempt. T_{rec} is the temperature at the position 1 bit before the writing position. A lower $\exp\left(-K_{\beta+}\right)$ and a higher $\exp\left(-K_{\beta-}\right)$ are better during the cooling time τ_{RW} from T_c to T_w in terms of stable writing, and both lower $\exp\left(-K_{\beta+}\right)$ and

$\exp\left(-K_{\beta-}\right)$ are better around the time corresponding to T_{rec} in terms of information (written bit) stability at the position 1 bit before the writing position.
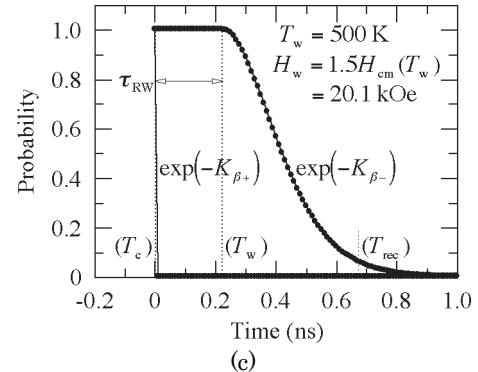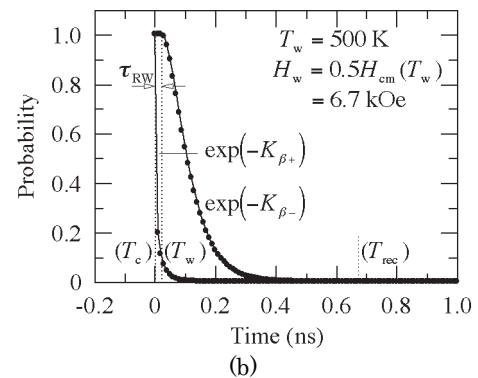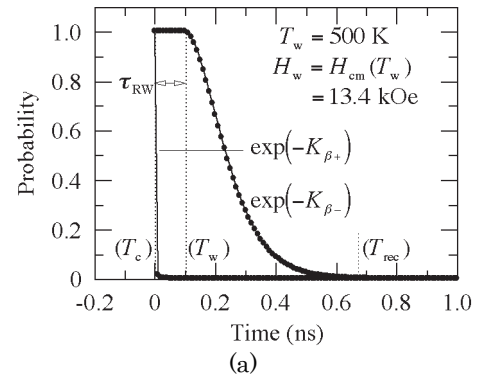

(a)

(b)

(c)

Fig. 2 Dependence of magnetization reversal probability on time for (a) $H_w = H_{cm}(T_w)$, (b) $H_w = 0.5H_{cm}(T_w)$, and (c) $H_w = 1.5H_{cm}(T_w)$.

The result is shown in Fig. 2 (a) when $T_w = 500$ K and $H_w = H_{cm}(T_w) = 13.4$ kOe according to Eq. (17). The time corresponding to T_c is 0 ns, that corresponding to T_w is 0.1 ns, and that corresponding to T_{rec} is 0.67 ns. The resultant τ_{RW} value is 0.1 ns. It is reported that a τ_{RW} value of around 0.1 ns is suitable for the micromagnetic calculation[4]. The $\exp\left(-K_{\beta+}\right)$ and $\exp\left(-K_{\beta-}\right)$ values are both one at the time corresponding to T_c since $K_{\beta\pm} = 0$. The $\exp\left(-K_{\beta+}\right)$ values are almost zero, and the attempt number is ten during the cooling time τ_{RW}, which is suitable for stable writing. The $\exp\left(-K_{\beta+}\right)$ and $\exp\left(-K_{\beta-}\right)$ values are both almost zero around the

time corresponding to T_{rec}, which is suitable for information stability at the position 1 bit before the writing position.

Figure 2 (b) shows the result when $T_w = 500$ K and $H_w = 0.5H_{cm}(T_w) = 6.7$ kOe instead of Eq. (17) where the composition and K_u/K_{bulk} are the same as those in Fig. 2 (a). The resultant τ_{RW} value is 0.02 ns. $\exp(-K_{\beta+})$ has a non-zero value, and the attempt number is only two during τ_{RW}, which is not suitable for stable writing. This corresponds to "write-error".

On the other hand, Fig. 2 (c) shows the result when $T_w = 500$ K and $H_w = 1.5H_{cm}(T_w) = 20.1$ kOe instead of Eq. (17) where the composition and K_u/K_{bulk} are the same as those in Fig. 2 (a). The resultant τ_{RW} value is 0.22 ns. In this case, $\exp(-K_{\beta-})$ has a non-zero value around the time corresponding to T_{rec}, which is unsuitable as regards the information stability at the position 1 bit before the writing position. This corresponds to "erasure-after-write".

3.2 Design procedure

The improved design procedure for obtaining the minimum K_u/K_{bulk} value is shown in Fig. 3. We fix τ_{RW} to 0.1 ns. First, $\tau_{RW} = 0.1$ ns, $K_u/K_{bulk} = 1$, and the design parameters including T_w, $\partial T/\partial x$ and v are set. T_c is determined from Eq. (16) as

$$T_c = T_w + \tau_{RW} \cdot \frac{\partial T}{\partial x} \cdot v. \tag{18}$$

Then, the Cu composition z in $(Fe_{0.5}Pt_{0.5})_{1-z}Cu_z$ of the medium is determined using the equation[6]:

$$T_c = \frac{2J(4(1-z))s(s+1)}{3k}, \tag{19}$$

where J is the exchange integral and s is the spin. The temperature dependence of the magnetic properties is determined by z and K_u/K_{bulk}. The composition is independent of K_u/K_{bulk}. The H_w value is determined using Eq. (17), which is dependent on K_u/K_{bulk}. The above means that the τ_{RW} of the cooling time from T_c to T_w is necessary during the writing process at which M_s aligns with the direction of H_w.

Next, new condition, which is the information stability at the writing position during $\tau_w = d_B/v$ (d_B: bit pitch) expressed by

$$K_{\beta+}(T_w, H_w) \geq TSF_w, \tag{20}$$

is added instead of Eq. (1). Then, the four HAMR conditions I, II, III, and IV mentioned above, that is Eqs. (5), (6), (7), and (8), respectively, are examined. If there are margins for all five conditions, K_u/K_{bulk} can be reduced. Since H_w is a function of K_u/K_{bulk}, H_w must be recalculated for reducing K_u/K_{bulk}. When one of the five conditions reaches the limit, the minimum K_u/K_{bulk} value can be determined. That condition

becomes a limiting factor.

The improved model calculation includes Eq. (20) instead of Eq. (1), and Eqs. (5), (6), (7), and (8) in the previous model calculation. Therefore, this calculation is almost the same as the previous model calculation. The difference is the introduction of the time τ_{RW}. τ_{RW} (Eqs. (16) and (17)) is the time from T_c to T_w for aligning M_s with H_w (writing bit), and τ_w (Eq. (20)) is the time from T_w to T_{rec} for the information (written bit) stability during the writing process. "Write-error" as regards τ_{RW} (writing bit) and τ_w (the written bit stability during the writing process) can be suppressed by Eqs. (16), (17) and Eq. (20), respectively. "Erasure-after-write" as regards the time after τ_w (the written bit stability after the writing process) can also be suppressed by Eq. (6).
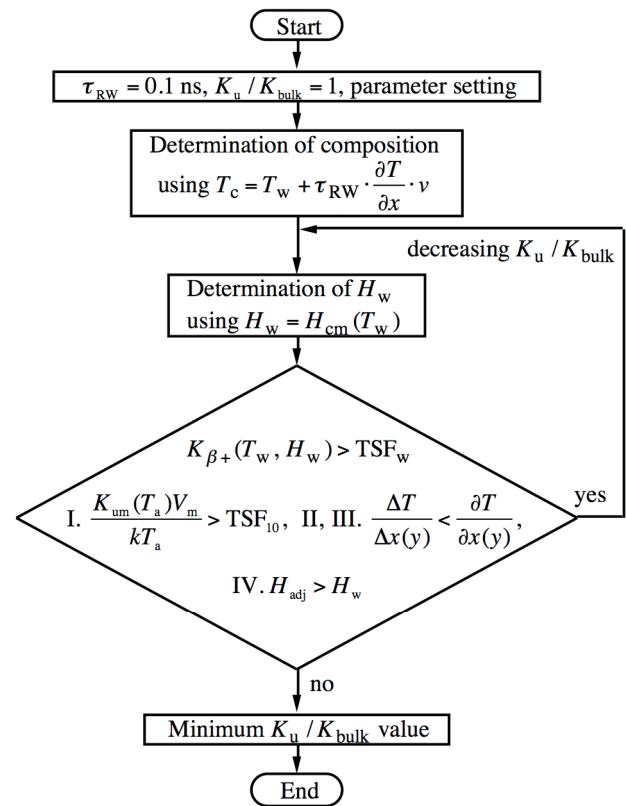

Fig. 3 HAMR design procedure for obtaining the minimum anisotropy constant ratio K_u/K_{bulk} using an improved model calculation.

3.3 Calculation results

The calculation conditions and parameters are the same as those reported elsewhere[3, 4].

The dependences of the minimum K_u/K_{bulk} value on T_w are shown in Tables 1, 2, and 3 for user areal densities of 2, 3, and 4 Tbpsi, respectively. The areal density calculated from the bit area S is larger than the user areal density. The difference is for the code of error correction, etc. The S value is inversely proportional to the areal density, and the heat-spot diameter d_w is inversely proportional to the square root of the areal density. The mean grain size D_m is

calculated using $\sqrt{S/n} - \Delta$ where $n = 4$ is the grain number per bit, and $\Delta = 1$ nm is the non-magnetic spacing between grains.

The Curie temperature T_c is $\tau_{RW} \cdot (\partial T/\partial x) \cdot v$ ($v = 10$ m/s) higher than T_w. T_w is determined by the T_c of the medium and not by the light power used for heating. If the light power alone is increased for a medium with the same T_c, the written bits will be spread in the cross-track direction, and it becomes impossible to keep the track pitch constant. Therefore, T_c must be increased to increase T_w.

The tables also show the magnetization M_s, the mean anisotropy constant K_{um}, the mean coercivity H_{cm}, and $K_{um}V_m/kT$ at 300 K.

TSF_w under the condition $K_{\beta+}(T_w, H_w) \geq TSF_w$ is constant for T_w, and is dependent on the areal density since the bit pitch decreases as the areal density increases[2, 3]. TSF_{10} under condition I is constant for T_w and the areal density, and $K_{um}(T_a)V_m/kT_a$ increases as T_w increases since $K_{um}(T_a)$ increases[7]. $\partial T/\partial x(y)$ under conditions II and III also increases as T_w increases[3]. H_{adj} under condition IV is sufficiently larger than H_w. The optimum bit pitch d_B, track pitch d_T, and d_T/d_B values are shown in the table.

Table 2 Calculation results of HAMR design for 3 Tbpsi and various writing temperatures T_w.

User areal density (Tbpsi)	3	3	3
S (nm^2)	187	187	187
d_w (nm)	11.5	11.5	11.5
T_w (K)	500	600	700
D_m (nm)	5.83	5.83	5.83
z (at.%)	34	21	7
T_c (K)	507	611	715
M_s (300 K) (emu/cm^3)	614	779	927
K_{um} (300 K) (10^6 erg/cm^3)	12	12	13
H_{cm} (300 K) (kOe)	38	31	27
$K_{um}V_m/kT$ (300 K)	76	79	83
TSF_w	7.86	7.86	7.86
$K_{\beta+}(T_w, H_w) \geq TSF_w$	8.19	8.05	7.98
TSF_{10}	62	62	62
I. $K_{um}(T_a)V_m/kT_a \geq TSF_{10}$	62	67	73
$\partial T/\partial x(y)$ (K/nm)	6.9	11.0	15.1
II, III. $\Delta T/\Delta x(y)$ (K/nm) $\leq \partial T/\partial x(y)$	6.9	11.0	15.1
H_w (kOe)	8.01	6.95	6.46
IV. H_{adj} (kOe) $\geq H_w$	11.4	10.3	9.93
K_u/K_{bulk}	0.46	0.29	0.21
d_B (nm)	7.77	7.81	7.84
d_T (nm)	24.0	23.9	23.8
d_T/d_B	3.10	3.06	3.03

Table 1 Calculation results of HAMR design for 2 Tbpsi and various writing temperatures T_w.

User areal density (Tbpsi)	2	2	2
S (nm^2)	280	280	280
d_w (nm)	14.1	14.1	14.1
T_w (K)	500	600	700
D_m (nm)	7.37	7.37	7.37
z (at.%)	34	21	7
T_c (K)	507	611	715
M_s (300 K) (emu/cm^3)	614	779	927
K_{um} (300 K) (10^6 erg/cm^3)	7	8	8
H_{cm} (300 K) (kOe)	24	19	17
$K_{um}V_m/kT$ (300 K)	76	80	85
TSF_w	8.15	8.15	8.15
$K_{\beta+}(T_w, H_w) \geq TSF_w$	8.19	8.15	8.15
TSF_{10}	62	62	62
I. $K_{um}(T_a)V_m/kT_a \geq TSF_{10}$	62	68	74
$\partial T/\partial x(y)$ (K/nm)	6.9	11.0	15.1
II, III. $\Delta T/\Delta x(y)$ (K/nm) $\leq \partial T/\partial x(y)$	5.7	9.1	12.3
H_w (kOe)	5.02	4.41	4.14
IV. H_{adj} (kOe) $\geq H_w$	7.25	6.66	6.52
K_u/K_{bulk}	0.29	0.18	0.14
d_B (nm)	9.59	9.64	9.69
d_T (nm)	29.2	29.0	28.9
d_T/d_B	3.05	3.01	2.99

Table 3 Calculation results of HAMR design for 4 Tbpsi and various writing temperatures T_w.

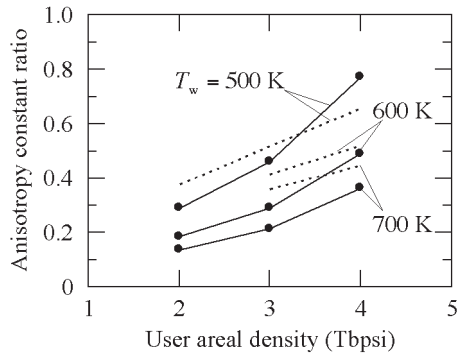| User areal density (Tbpsi)	4	4	4
S (nm^2)	140	140	140
d_w (nm)	10	10	10
T_w (K)	500	600	700
D_m (nm)	4.92	4.92	4.92
z (at.%)	34	21	7
T_c (K)	507	611	715
M_s (300 K) (emu/cm^3)	614	779	927
K_{um} (300 K) (10^6 erg/cm^3)	20	20	21
H_{cm} (300 K) (kOe)	64	52	46
$K_{um}V_m/kT$ (300 K)	91	95	100
TSF_w	7.68	7.68	7.68
$K_{\beta+}(T_w, H_w) \geq TSF_w$	9.76	9.69	9.63
TSF_{10}	62	62	62
I. $K_{um}(T_a)V_m/kT_a \geq TSF_{10}$	74	81	88
$\partial T/\partial x(y)$ (K/nm)	6.9	11.0	15.1
II, III. $\Delta T/\Delta x(y)$ (K/nm) $\leq \partial T/\partial x(y)$	6.9	11.0	15.1
H_w (kOe)	13.4	11.8	11.0
IV. H_{adj} (kOe) $\geq H_w$	22.5	20.2	19.3
K_u/K_{bulk}	0.77	0.49	0.36
d_B (nm)	6.70	6.73	6.75
d_T (nm)	20.9	20.8	20.7
d_T/d_B	3.12	3.09	3.07

Fig. 4 Dependence of anisotropy constant ratio K_u / K_{bulk} on user areal density for various writing temperatures T_w. Dotted lines are results calculated using a previous model.

The dependence of K_u / K_{bulk} on the user areal density for various T_w values is summarized in Fig. 4. The dotted lines show results calculated using the previous model. K_u / K_{bulk} at 2 Tbpsi can be obtained using the improved model calculation. K_u / K_{bulk} and/or T_w must be increased to achieve a high areal density.

4. Conclusions

We improved our model calculation for heat-assisted magnetic recording (HAMR) by introducing the concept of the recording time window proposed in the micromagnetic calculation. This improvement means that the results obtained using the model calculation become consistent with those obtained using a micromagnetic calculation.

The minimum anisotropy constant ratio K_u / K_{bulk} of the medium at 2, 3, and 4 Tbpsi can be obtained using the improved model calculation. K_u / K_{bulk} and/or the writing temperature must be increased to realize a high areal density.

References

1) S. H. Charap, P. -L. Lu, and Y. He: *IEEE Trans. Magn.*, **33**, 978 (1997).
2) T. Kobayashi, Y. Isowaki, and Y. Fujiwara: *J. Magn. Soc. Jpn.*, **39**, 8 (2015).
3) T. Kobayashi, Y. Isowaki, and Y. Fujiwara: *J. Magn. Soc. Jpn.*, **39**, 139 (2015).
4) J. -G. Zhu and H. Li: *IEEE Trans. Magn.*, **49**, 765 (2013).
5) Y. Isowaki, T. Kobayashi, and Y. Fujiwara: *J. Magn. Soc. Jpn.*, **38**, 1 (2014).
6) K. Ohta: Jikikogaku no Kiso 1 (in Japanese), p. 151 (Kyoritsu Shuppan, Tokyo, 1973).
7) T. Kobayashi, Y. Isowaki, and Y. Fujiwara: *J. Magn. Soc. Jpn.*, **40**, 1 (2016).

<Paper>

Simultaneous magnetic and chemical imaging of Nd-Fe-B thin films by means of XMCD-PEEM technique

R. Goto[1,*], S. Okamoto[1, 2], T. Ohkochi[3], N. Kikuchi[1], O. Kitakami[1], and T. Nakamura[2, 3]

[1] Institute of Multidisciplinary Research for Advanced Materials (IMRAM), Tohoku University, *2-1-1 Katahira, Aoba-ku, Sendai 980-8577, Japan*

[2] Elements Strategy Initiative Center for Magnetic Materials (ESICMM), National Institute for Materials Science, *1-2-1 Sengen, Tsukuba, Ibaraki 305-0047, Japan*

[3] Japan Synchrotron Radiation Research Institute/SPring-8, *1-1-1, Kouto, Sayo-cho, Sayo-gun, Hyogo 679-5198, Japan*

The coercivity mechanism of Nd-Fe-B thin film samples with and without Nd deposition was investigated by simultaneous chemical and magnetic imaging by means of X-ray magnetic circular dichroism-photoemission electron microscopy. The two Nd-Fe-B thin film samples exhibited almost the same surface morphology and magnetic domain patterns, but their coercive fields were quite different, being 0.98 T for the sample with Nd deposition and 0.55 T for sample without Nd deposition. The chemical distribution of Nd revealed that Nd aggregates with the average size of 130 nm exist, and the density in the Nd-deposited sample is much higher than that in the not deposited one. A comparison of the magnetic and chemical contrast images implied that the Nd aggregates act as domain wall pinning sites, indicating that the large coercivity difference in the Nd-Fe-B thin films would be attributable to the different density of wall pinning sites.

Key words: Neodymium-Iron-Boron magnets, thin films, magnetic reversal, X-ray magnetic circular dichroism, photoelectron emission microscopy

1. Introduction

Nd-Fe-B magnets are a key material for high efficiency electric generators and motors. For these applications, numerous attempts have been made to enhance the coercivity while maintaining high saturation magnetization. Although heavy rare earth (RE) elements such as Dy or Tb are usually added to increase the coercivity of Nd-Fe-B magnets, these RE elements degrade their saturation magnetization due to antiferromagnetic coupling between 3d and 4f magnetic moments. Moreover, the availability and price of the heavy RE elements are currently serious resource problems. Recently, the coercivity $\mu_0 H_c$ of Nd-Fe-B sintered magnets has been successfully enhanced to about 2 T even without addition of heavy RE elements by various methods such as refinement of the constituent crystal grains of the $Nd_2Fe_{14}B$ phase [1] and/or grain boundary diffusion of RE elements to restore magnetic anisotropy near the grain boundaries or to suppress intergranular exchange coupling [2, 3]. However, the $\mu_0 H_c$ obtained by these techniques remains much smaller than the anisotropy field of $\mu_0 H_k = 7.5$ T [4].

The large discrepancy between the $\mu_0 H_c$ and $\mu_0 H_k$ observed in a wide variety of permanent magnets, which is known as Brown's paradox [5], is the subject of a long-standing debate in magnetics. To solve this problem, a detailed analysis of the magnetization reversal process is indispensable. So far it is widely accepted that nucleation of reversed domains dominates the magnetization reversal in Nd-Fe-B

magnets, judging from the initial and minor magnetization curve behaviors [6]. On the other hand, the angular dependence and c-axis dispersion dependence of $\mu_0 H_c$ [7, 8] strongly suggest that domain wall depinning is the dominant process in Nd-Fe-B magnets.

Recently, we proposed a new approach to examine the magnetization reversal process [9]. At a finite temperature, magnetization reversal proceeds under the influence of thermal activation, which enables the magnetization to overcome a finite energy barrier separating local energy minima. The energy barrier is a function of a magnetic field H, and its function form depends on the magnetization reversal process. For example, the energy barrier is a quadratic function of H for coherent rotation and/or nucleation [10] and a linear function of H for weak pinning of a domain wall [11]. The energy barrier function can be determined experimentally by analysis of magnetic viscosity measurements. We applied this type of analysis to two kinds of (001) oriented Nd-Fe-B thin film samples with and without a Nd overlayer which is preferentially diffused along the Nd-Fe-B grain boundaries during the deposition [9]. In spite of the large difference in their coercivities, both of their barriers were found to be linear functions of H, suggesting that weak domain wall pinning is dominant in both samples. It should be stressed here that the above two Nd-Fe-B thin film samples have almost the same structures, such as c-axis orientation, grain size, and so on. In order to understand the reason for the large coercivity

difference mentioned above, simultaneous magnetic and chemical distribution imaging were performed on the two Nd-Fe-B film samples by means of X-ray magnetic circular dichroism-photoemission electron microscopy (XMCD-PEEM).

2. Experiments

Nd-Fe-B thin films examined in the present study are grown on MgO (001) substrates with the layer structure of MgO/Mo(30 nm)/Nd(0.25 nm)/Nd-Fe-B(50 nm)/Nd(t_{Nd} = 0, 1 nm)/Mo(10 nm). For brevity, the Nd-Fe-B film samples with and without a Nd deposition are denoted as Nd-Fe-B/Nd and Nd-Fe-B, respectively. The composition of the Nd-Fe-B layer is adjusted to $Nd_{12.8}Fe_{78.7}B_{8.5}$ in at% by controlling the sputtering rates of Nd, Fe, and B. The substrate is kept at T_s = 500°C during deposition of both Nd-Fe-B and Nd. The detailed sample fabrication conditions and magnetic and structural characterization methods are described elsewhere [9]. Since both Nd-Fe-B/Nd and Nd-Fe-B are prepared under the same condition, they have the same crystal structure with good c-axis orientation. The surface morphologies and magnetic domain structures were observed by atomic force microscopy (AFM) and magnetic force microscopy (MFM), respectively. X-ray magnetic circular dichroism-photoemission electron microscopy (XMCD-PEEM) was performed with Nd $M_{4,5}$ and Fe $L_{2,3}$ edges at the BL25SU beamline of SPring-8. Soft X-rays were incident on the sample at 30 degree with respect to the sample plane, enabling us to detect perpendicular component of the magnetizations. Prior to the XMCD-PEEM experiment, the Mo capping layers were etched *ex situ* down to about 5 nm considering the very short probing depth of PEEM. The samples were observed at room temperature without application of a magnetic field.

3. Results and Discussions

Figures 1(a) and 1(b) show the perpendicular magnetization curves of Nd-Fe-B and Nd-Fe-B/Nd, respectively. While they both exhibit high remanence ratios, their coercive fields are quite different, being $\mu_0 H_c$ = 0.55 T for Nd-Fe-B and 0.98 T for Nd-Fe-B/Nd. According to the AFM images in Figs. 1(c) and 1(d), both samples have a partially-connected island structure with the mean size of 100±50 nm. Figures 1(e) and 1(f) show the MFM images of thermally demagnetized Nd-Fe-B and Nd-Fe-B/Nd, respectively. Their domain structures are very similar with the average size of 200 nm. This is roughly two times larger than the grain size in Figs.1 (c) and 1(d), indicating that each Nd-Fe-B grain is more or less exchange-coupled to neighboring grains. In spite of the very similar micro- and domain-structures, the Nd-Fe-B with and without Nd deposition exhibit quite
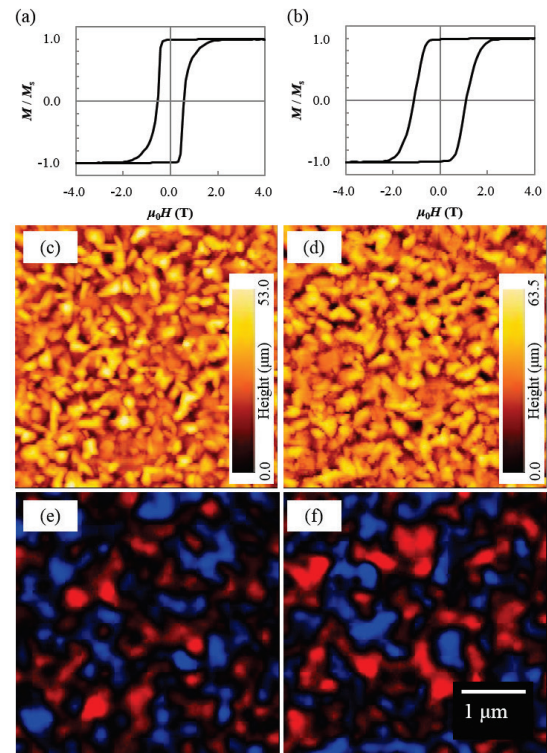

Fig. 1 (a) and (b) perpendicular magnetization curves, (c) and (d) AFM images, and (e) and (f) MFM images of thermal demagnetization states. (a), (c), and (e) show Nd-Fe-B, and (b), (d), and (f) show Nd-Fe-B/Nd.

different coercivities.

In order to explore the reason for the difference, we performed simultaneous chemical and magnetic imaging by means of XMCD-PEEM. Figure 2 shows the X-ray absorption spectra (XAS) of the Nd-Fe-B obtained at the Fe $L_{2,3}$ and Nd $M_{4,5}$ edges. In addition to the clear Fe and Nd absorption edges, a small shoulder is observed at the slightly higher energy side near the Fe L_3 edge owing to oxidation of Fe. This oxidation may be caused by partial over-etching of the Mo capping layer. We believe this small amount of oxidation does not affect the following discussion.

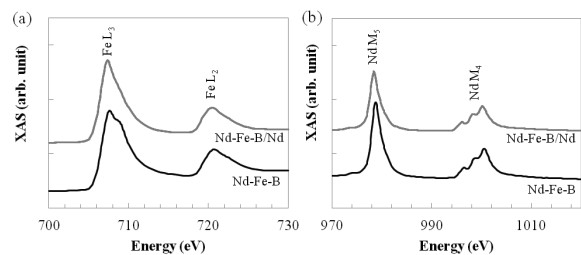Figures 3(a) and 3(b) show the chemical contrast maps of Nd for Nd-Fe-B and Nd-Fe-B/Nd, respectively,

Fig. 2 XAS spectra for (a) Fe $L_{2,3}$ and (b) Nd $M_{4,5}$ edges of Nd-Fe-B and Nd-FeB/Nd.
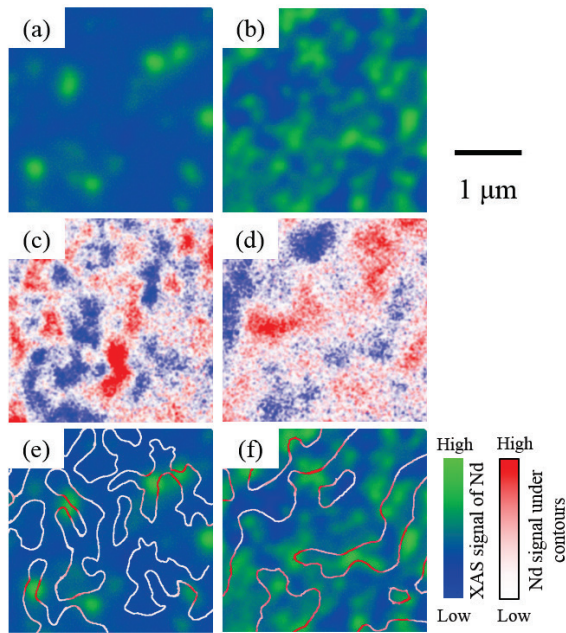
Fig. 3 (a) and (b) chemical contrast images of Nd, (c) and (d) magnetic contrast images, and (e) and (f) contours of magnetic contrast shown in (c) and (d) overlapped with Nd chemical images. The red-colored contrast of contours corresponds to the Nd content under themselves. (a), (c), and (e) show Nd-Fe-B, and (b), (e), and (f) show Nd-Fe-B/Nd.

which were displayed as the spatial distributions of the photoemission intensities at the Nd M_5-edge (978.5 eV) normalized to those at a pre-absorption-edge (972.0 eV). Since Nd is one of the main constituents of the samples, Nd is distributed over the whole area of the samples, as indicated by the blue-colored areas in Figs. 3(a) and 3(b). In addition to this uniform Nd distribution, many tiny Nd-rich aggregates with the size of 130 nm can be clearly observed as indicated by green areas in the same figures. Obviously, the density of the Nd aggregates in Nd-Fe-B/Nd is much higher than that in Nd-Fe-B. According to cross-sectional transmission electron microscopy (TEM) observation of the Nd-Fe-B film prepared under the same conditions, Nd aggregates exist laterally beside the Nd-Fe-B particles on the Mo buffer layer [12]. Figures 3(c) and 3(d) show XMCD-PEEM images of Nd-Fe-B and Nd-Fe-B/Nd, respectively, which were taken to be the XMCD amplitude defined as the difference of XMCD intensity between the Fe L_3 edge (707.6 eV) and Fe L_2 edge (720.8 eV) to highlight the very weak XMCD contrast. In spite of this data processing, the XMCD contrast is still very weak, probably due to the presence of the Mo capping layer. However, XMCD contrasts reflecting the magnetic domain states can be clearly noted, and the patterns are similar to the MFM images in Figs. 1(e) and 1(f). The average domain width of Nd-Fe-B in fig.

3(c) is about 200 nm, being comparable with the value from MFM images in Fig. 1(e). For Nd-Fe-B/Nd, however, the domain width roughly reaches 400 nm, which is about 2 times larger than that from MFM in Fig. 1(f). This discrepancy is probably brought about by weak magnetic contrast in the XMCD measurements. The contours of these XMCD contrasts are overlaid on the chemical mapping of Nd in Figs. 3(e) and 3(f). Note that the magnetic contours which correspond to domain walls partially run across Nd aggregates as indicated by the red-colored portions on the contours. It suggests that Nd-rich aggregates act as pinning sites of magnetic domain walls. This tendency is more obvious in the Nd-Fe-B/Nd sample shown in Fig. 3(f). Each magnetic contour overlaps multiple Nd aggregates, and in some cases lies along the aggregates. The above observation implies that Nd aggregates act as pinning sites of magnetic domain walls. When a magnetic domain wall is pinned at multiple defects, Nd aggregates in this study, the effective pinning force in the two-dimensional system as in the present study may be proportional to the density of defects [13] if the so-called weak pinning process is dominant [14]. Thus based on the present experimental results, we at present consider that the larger coercivity for Nd-Fe-B/Nd is due to higher density of pinning sites, in this case Nd aggregates. This conclusion is qualitatively consistent with our previous report, in which we found that domain wall pinning was dominant for both Nd-Fe-B and the Nd-Fe-B/Nd samples [9].

4. Conclusion

To discuss the origin of the different coercive fields of Nd-Fe-B thin film samples with and without Nd deposition, simultaneous observations of magnetic and chemical contrast images were carried out by the XMCD-PEEM technique. These two Nd-Fe-B films exhibit almost the same surface morphologies and magnetic domain patterns, but their coercive fields are quite different. From the Nd chemical contrast imaging, it was found that a large number of Nd aggregates with the average size of 130 nm exist, and the density of the Nd aggregates for the Nd deposited sample is much higher than that for not deposited one. Although the XMCD contrasts of these thin film samples were very weak, patterns similar to the MFM images were obtained. A comparison of the chemical and magnetic contrast images implied that the Nd aggregates act as wall pinning sites. This result indicates that the large difference in coercive fields of the Nd-Fe-B thin films with and without Nd deposition is attributable to the different density of wall pinning sites.

References

1) Y. Une and M. Sagawa: *J. Japan Inst. Met.* **76**, 12 (2012).
2) H. Nakamura, K. Hirota, T. Ohashi and T. Minowa: *J. Phys. D. Appl. Phys.* **44** ,064003 (2011).
3) H. Sepehri-Amin, T. Ohkubo and K. Hono: *Acta Mater.* **61** ,1982 (2013).
4) R. Grössinger, X.K. Sun, R. Eibler, K.H.J. Buschow and H.R. Kirchmayr: *J. Magn. Magn. Mater.* **58**, 55 (1986).
5) W.F. Brown, *Rev. Mod. Phys.* **17**, 15 (1945).
6) R. Skomski and J. M. D. Coey: Permanent Magnetism, p.175 (Institute of Physics Publishing, Bristol and Phyiladelphia, 1981).
7) F. Cebollada, M. Rossignol, D. Givord, V. Villas-Boas and J. González: *Phys. Rev. B* **52**, 13511 (1995).
8) Y. Matsuura, J. Hoshijima, R. Ishii, *J. Magn. Magn. Mater.* **336**, 88 (2013).
9) R. Goto, S. Okamoto, N. Kikuchi and O. Kitakami: *J. Appl. Phys.* **117**, 17B514 (2015).
10) E.C. Stoner and E.P. Wohlfarth: *Philos. Trans. R. Soc. A Math. Phys. Eng. Sci.* **240**, 599 (1948).
11) P. Gaunt: *J. Appl. Phys.* **59**, 4129 (1986).
12) R. Goto, S. Okamoto, N. Kikuchi and O. Kitakami: in preparation for submission
13) See, for example, the very simple and classical Neel model on domain wall pinning. (e.g. A. H. Morrish: The Physical Principles of Magnetism (Wiley-IEEE Press, 2001)).
14) According to our previous analysis on magnetic viscosity measurements, the functional form of the energy barrier suggests the weak pinning/depinning process in conventional NdFeB magnets.

Present address
*Santoku Corporation, 4-14-34 Fukaekitamachi, Higashinada-ku, Kobe, Hyogo 658-0013, Japan

<Paper>

Structure and magnetic properties for FePt thin films prepared on MgAl₂O₄ and MgO substrates

H. Iwama, M. Doi and T. Shima

Graduate School of Engineering, Tohoku Gakuin University, Tagajo, 985-8537, Japan

In order to investigate the effect of lattice mismatch between FePt thin films and single crystal substrates on the tetragonality and the magnetization process, FePt thin films have been fabricated on MgAl₂O₄ (MAO) (100) and MgO (100) single crystalline substrates at a substrate temperature of 700 °C. The Fe concentration in the FePt films was varied from 45.0 to 50.8 at. %. In addition to the fundamental (002) peak, (001) and (003) superlattice peaks have clearly been observed in the X-ray diffraction patterns for all the samples, indicating the formation of $L1_0$ ordered structure. The magnetization measurements show that all the samples are perpendicularly magnetized. Large coercivity (H_c) of 57.8 kOe and 54.4 kOe was observed for the films with $Fe_{49.3}Pt_{50.7}$ and $Fe_{48.3}Pt_{51.7}$ (at. %) deposited on MgO and MAO substrates, respectively. It was confirmed that good hard magnetic properties can be obtained for the $Fe_{49}Pt_{51}$ (at. %) thin film.

Key words: $L1_0$ ordered FePt, hard magnetic material, thin film, MgO substrate, MgAl₂O₄ substrate

1. Introduction

The magnetization process of assemblies of ferromagnetic nanoparticles with a large uniaxial magnetocrystalline anisotropy is of great scientific and technological interest, since they are expected to be applied in forthcoming magnetic devices such as high density magnetic recording media and high performance biasing nano-magnets. It is well known that the magnetization process and the coercivity depend strongly on the characteristic size and the morphology of the assemblies of ferromagnetic particles. Since FePt alloy shows high uniaxial magnetocrystalline anisotropy (K_u = 7.0×10⁷ erg/cm³) [1], moderate saturation magnetization and high corrosion resistance, several studies have recently been done on $L1_0$ ordered [CuAu (I) type] FePt thin films [2–14] and nanoparticles [15, 16] using conventional thin film preparation methods and chemical syntheses. It is also thought to overcome the instability of magnetization vectors caused by thermal fluctuation even in the nano-meter scaled particles. However, magnetization process of FePt thin films has not been fully elucidated. The lattice mismatch plays a crucial role in the growth of epitaxial thin films. Generally, MgO single crystalline substrate has been commonly used to induce the $L1_0$ ordered (001) texture of FePt films. Recently, low temperature fabrication of epitaxial FePt thin films below 400 ºC have been reported for MgAl₂O₄ [17] single crystalline substrates. However, systematic investigations of the effects of lattice mismatch on the structure and magnetic properties of FePt films have rarely been reported. Therefore, it would be worthwhile to study the structure and magnetic properties of FePt films prepared on different substrates. For this purpose, two single crystal substrates MgO (NaCl-type) and MgAl₂O₄ (Spinel-type) were chosen. The values of unstrained lattice mismatch between a-axis of $L1_0$ FePt ordered alloy and these substrates are 8.4 % for MgO [18] and 3.8 % for MgAl₂O₄ [19].

In this study, in order to investigate the effect of lattice mismatch between FePt thin films and single crystal substrates on the tetragonality and the magnetization process, FePt thin films have been fabricated on MgAl₂O₄ (MAO) (100) and MgO (100) single crystalline substrates, their structure and magnetic properties have been investigated.

2. Experimental procedure

All the samples were prepared using an ultrahigh vacuum magnetron sputtering system (ULVAC, QAM4) with co-deposition of Fe and Pt directly onto polished single crystalline MgO (100) or MAO (100) substrates. The lattice parameters of $L1_0$ ordered FePt alloy, MAO (100) substrate and MgO (100) substrate are a_{FePt} = 0.385 nm, c_{FePt} = 0.371 nm ($L1_0$-$Fe_{50}Pt_{50}$ (at. %)) [20], a_{MAO} = 0.404 nm [19] and a_{MgO} = 0.420 nm [18]. The targets were commercial products with purities higher than 99.99 at% for Fe and 99.9 at% for Pt. The base pressure was under 8.5×10⁻⁷ Pa. High-purity argon of 0.2 Pa was introduced during sputtering. The substrates were heated to T_s = 700 ºC during deposition. The nominal thickness of FePt layer was fixed at 10 nm. The compositions of the films were determined by an electron probe X-ray microanalysis (EPMA) and X = 45.0, 47.2, 48.3, 48.8, 49.3, 49.8 50.3 and 50.8 for Fe_XPt_{100-X} (at. %) are confirmed. The structural analysis was performed by X-ray diffraction (XRD) with Cu $K\alpha$ radiation. The lattice constant of c-axis was obtained by the out-of-plane XRD measurement, while the value of a-axis was obtained by the in-plane XRD measurement. The film morphology was observed by atomic force microscopy (AFM, in tapping mode). The magnetic properties were measured by a superconducting quantum interference device (SQUID) magnetometer in the field up to 70 kOe at room temperature (R. T.).
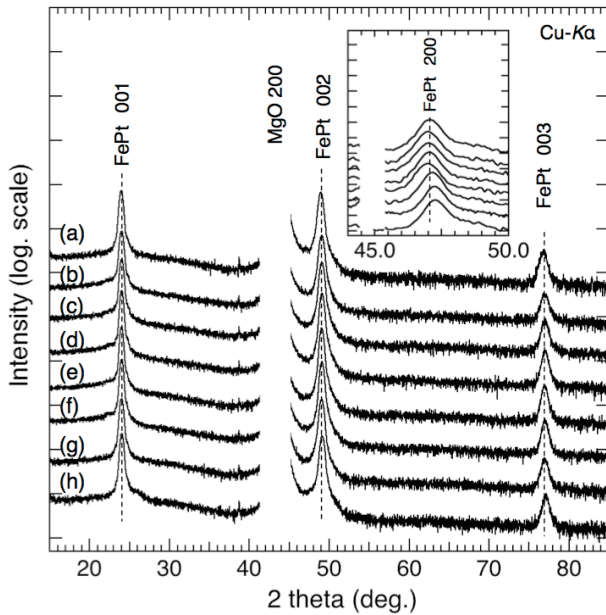
Fig. 1. XRD patterns for FePt thin films prepared on MgO (100) substrate. Inset show the in-plane XRD patterns for FePt thin films. The Fe content X for Fe_XPt_{100-X} films are 45.0 (a), 47.2 (b), 48.3 (c), 48.8 (d), 49.3 (e), 49.8 (f), 50.3 (g) and 50.8 (at. %) (h).
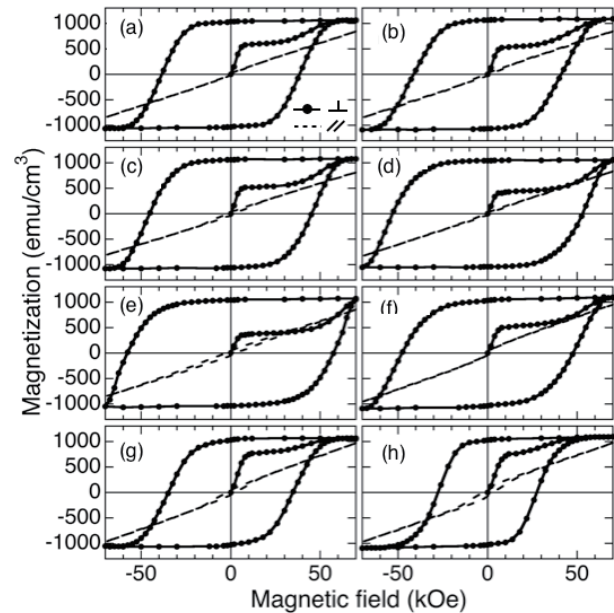

Fig. 2. Magnetization curves for FePt thin films prepared on MgO (100) substrate. The Fe content X for Fe_XPt_{100-X} films are 45.0 (a), 47.2 (b), 48.3 (c), 48.8 (d), 49.3 (e), 49.8 (f), 50.3 (g) and 50.8 (at. %) (h).

3. Results and discussion

XRD patterns for Fe_XPt_{100-X} films with various Fe content prepared on MgO (100) substrate are shown in Fig. 1. The Fe content was varied as follows: $X = 45.0$ (a), 47.2 (b), 48.3 (c), 48.8 (d), 49.3 (e), 49.8 (f), 50.3 (g) and 50.8 (at. %) (h). In addition to a fundamental (002) peak, (001) and (003) superlattice peaks of the $L1_0$-FePt phase were clearly observed for all the samples. The peak from the other plane of the $L1_0$ structure was not observed. Therefore, it is confirmed that the c-axis of FePt layers was aligned perpendicular to the film plane for the FePt films. With increasing X, the peak position of the (001) plane shifts to a higher angle, suggesting that the lattice parameter of c-axis decreases due to the change of the tetragonality of $L1_0$ ordered FePt phase. From the integrated intensities of fundamental and superlattice peaks extracted from numerical fitting, the degree of long-range chemical order parameter S was evaluated. The detailed procedure for the evaluation of S was described in a previous letter [21]. The S shows the maximum of 0.80 ± 0.05 for $Fe_{49.3}Pt_{50.7}$ (at. %) (e).

Magnetization curves for the Fe_XPt_{100-X} films prepared on MgO (100) substrate are shown in Fig. 2. All the measurements were preformed at R.T.. The solid and broken lines denote the magnetic fields applied in the perpendicular direction to the film plane and in-plane directions, respectively. The magnetic easy axes are perpendicular to the film plane for all the samples, since the [001] axis of the tetragonal $L1_0$ ordered structure was perpendicular to the film plane as

demonstrated in Fig. 1. Coercivity (H_c) of 38.4 kOe was obtained for the film with $X = 45.0$ (at. %) (a). The maximum H_c of 57.8 kOe was obtained for the film with $X = 49.3$ (at. %) (e). With further increasing of Fe content, H_c decreases slowly, but still keeps a quite large value of 48 kOe for the film with $X = 49.8$ (at. %) (f). However, H_c decreased to 27.7 kOe for the film with $X = 50.8$ (at. %) (h). The in-plane magnetization does not saturate even at a magnetic field of 70 kOe, which is the maximum magnetic field of the SQUID magnetometer, indicating that they possess high uniaxial magnetic anisotropy. A remarkable step in the initial magnetization curve was observed for all samples. A steep increase of the magnetization at low magnetic field was observed. The fractional magnetization at low magnetic field corresponds to the magnetic domain wall displacement; in other words, particles larger than 200 nm (single domain size [22]) with multiple domain structure are magnetized at low magnetic field. However, it is to be magnetized at applied magnetic field more then 10 kOe, because they contain single domain particles. Hence, the magnetization process governed by the magnetic domain wall displacement in the multiple domain particles and the rotation of the magnetization in the single domain particles.

XRD patterns for Fe_XPt_{100-X} films prepared on MAO (100) substrate are shown in Fig. 3. The Fe content was varied as follows: $X = 45.0$ (a), 47.2 (b), 48.3 (c), 48.8 (d), 49.3 (e), 49.8 (f), 50.3 (g) and 50.8 (at. %) (h). Both fundamental and superlattice peaks of the $L1_0$-FePt phase were clearly observed for all the samples. The unlabeled peaks were due to the MAO (100) substrate.
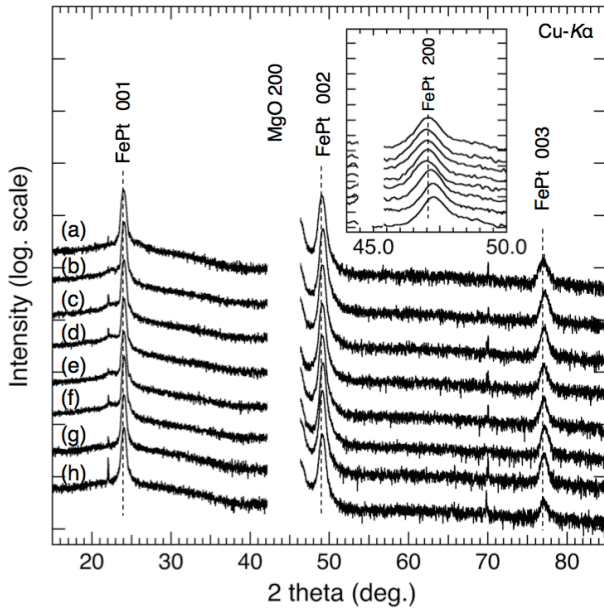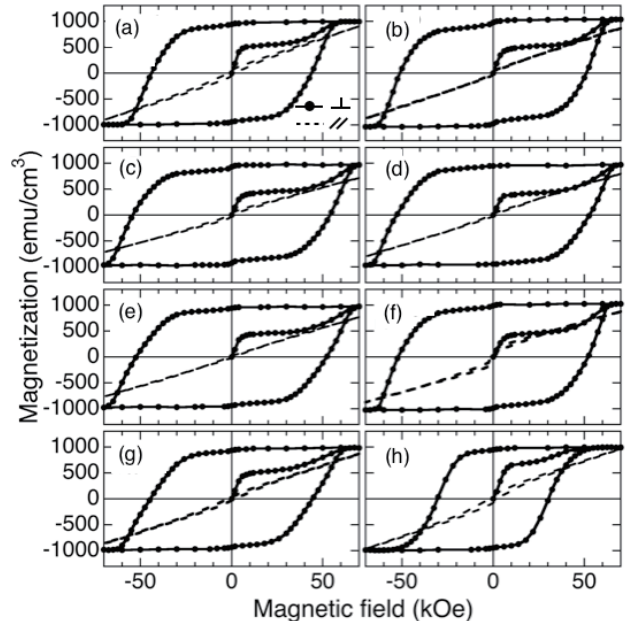
Fig. 3. XRD patterns for FePt thin films prepared on MgAl$_2$O$_4$ (100) substrate. Inset show the in-plane XRD patterns for FePt thin films. The Fe content X for Fe$_X$Pt$_{100-X}$ films are 45.0 (a), 47.2 (b), 48.3 (c), 48.8 (d), 49.3 (e), 49.8 (f), 50.3 (g) and 50.8 (at. %) (h).

Fig. 4. Magnetization curves for FePt thin films prepared on MgAl$_2$O$_4$ (100) substrate. The Fe content X for Fe$_X$Pt$_{100-X}$ films are 45.0 (a), 47.2 (b), 48.3 (c), 48.8 (d), 49.3 (e), 49.8 (f), 50.3 (g) and 50.8 (at. %) (h).

The peak from the other plane of the $L1_0$ structure was not observed. It is also confirmed that c-axis of FePt layers was successfully aligned perpendicular to the film plane for the films deposited on the MAO (100) substrate. This indicates that the highly (001) oriented $L1_0$ structure was achieved for the FePt films, even with different Fe content of the FePt layer. From the integrated intensities of fundamental and superlattice peaks extracted from numerical fitting, the degree of long-range chemical order parameter S was evaluated. The S shows the maximum of 0.74±0.05 for Fe$_{48.3}$Pt$_{51.7}$ (at. %) (c). The clear four fold symmetry was also confirmed in both of FePt thin films on MgO (100) and MAO (100) substrates by $2\theta_\chi/\varphi$ scan of XRD. As a result, the epitaxial growth of FePt thin films on MgO (100) and MAO (100) substrates were confirmed. From the AFM observation, island growth with the island size of about 150 nm was observed in both the FePt thin films on the MgO (100) and the MAO (100) substrates.

Magnetization curves for FePt films with various Fe content prepared on MAO (100) substrate are shown in Fig. 4. The magnetic field was applied in the perpendicular (solid line) and in-plane (broken line) directions to the film. The easy magnetization axis is aligned perpendicular to the film plane for all the samples. The [001] axis of the tetragonal $L1_0$ ordered structure was perpendicular to the film plane as demonstrated in Fig. 3. H_c of 44.1 kOe was obtained for the film with X = 45.0 (at. %) (a). The maximum H_c of 54.4 kOe was obtained for the film with X = 48.3 (at. %) (c). With further increasing Fe content, H_c decreases slowly, but still keeps a quite large value of 52.1 kOe for

the film with X = 49.8 (at. %) (f). However, H_c was decreased to 44.8 kOe and 30.8 kOe for the films with X = 50.3 (g) and 50.8 (at. %) (h), respectively. Similar to the result observed in the initial magnetization curves of the films deposited on MgO (100) substrate, the magnetization process for the FePt films deposited on MAO (100) substrate is thought to a mixture of a magnetic domain displacement and a rotation of the magnetism.

The a-axis, c-axis, c/a and H_c for FePt thin films deposited on MgO (100) and MAO (100) substrates with different Fe content are summarized in Fig. 5. Solid circles and solid triangles denote the data for the FePt film deposited on MgO (100) substrate, while open marks are denote the data for the films deposited on MAO (100) substrate. Maximum value of a-axis was obtained for both substrates at X = 47.1 (at. %). However, a-axis was decreased with further increased of Fe content. While monotonical increase was obtained for c/a more than X = 48 (at. %) and maximum. H_c was obtained at X = 49 (at. %) for both films. From these results, it is confirmed that lattice spacing of a-axis is strongly dependent on the composition rather than the one of c-axis. The reason why the FePt films deposited on MAO (100) substrates show large H_c at wide composition region is thought to arise from a small lattice mismatch between the substrate and the FePt film. The more detail investigation of morphological analysis will be necessary for the exact discussion of H_c.

4. Summary

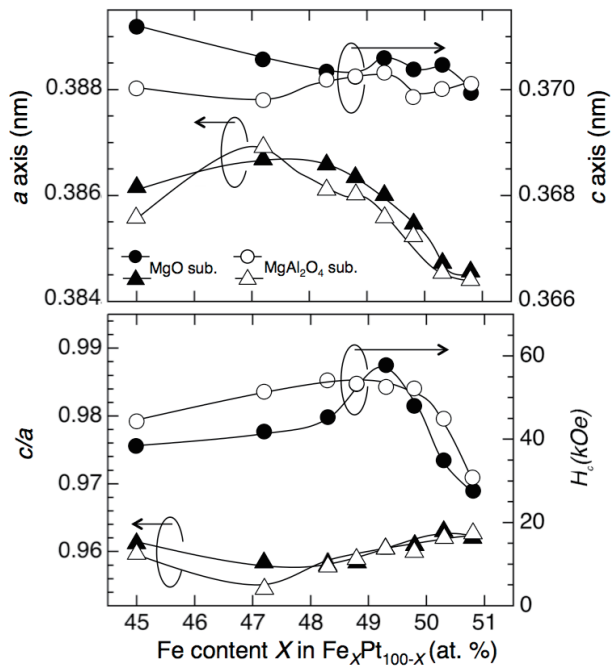The structure and magnetic properties of FePt films

Fig. 5. Effect of Fe content X on the lattice constant of *a* and *c*-axis, the tetragonality represented by *c/a* and coercivity H_c for Fe$_X$Pt$_{100-X}$ thin films prepared on MgO (100) and MgAl$_2$O$_4$ (100) single crystalline substrates.

prepared on MgO (100) and MAO (100) substrates have been investigated. The FePt layer was epitaxially grown on MgO (100) and MAO (100) substrates. Large H_c of 57.8 kOe and 54.4 kOe was obtained for the films with Fe$_{49.3}$Pt$_{50.7}$ and Fe$_{48.3}$Pt$_{51.7}$ (at. %) deposited on MgO (100) and MAO (100) substrates, respectively. It was confirmed that good hard magnetic properties can be obtained for the Fe$_{49}$Pt$_{51}$ (at. %) thin film. Although, similar behavior of H_c dependence on the composition was observed in FePt thin films on MgO (100) and MAO (100) substrates, large H_c can be obtained at wide composition range of Fe$_X$Pt$_{100-X}$ thin films, even at low Fe content between 45.0 and 48.3 (at. %).

References

1) O. A. Ovanov, L. V. Solina, and V. A. Demshina: *Phys. Met. Metallogr.*, **35**, 81 (1973).
2) T. Suzuki, K. Harada, N. Honda, and K. Ouchi: *Phys. Met. Metallogr.*, **193**, 85 (1999).
3) C. L. Platt, K. W. Wierman, E. B. Svedberg, R. van de Veerdonk, J. K. Howard, A. G. Roy, and D. E. Laughlin: *J. Appl. Phys.,* **92**, 6104 (2002).
4) T. Shima, K. Takanashi, Y. K. Takahashi, and K. Hono: *Appl. Phys. Lett.,* **81**, 1050 (2002).
5) T. Shima, K. Takanashi, Y. K. Takahashi, K. Hono, G. Q. Li, and S. Ishio: *Appl. Phys. Lett.,* **99**, 033516 (2006).
6) C. Moutafis, S. Komineas, C. A. F. Vaz, J. A. C. Bland, T. Shima, T. Seki, and K. Takanashi: *Phys. Rev. B,* **76**, 104426 (2007).
7) Z. Xu, X. D. Liu, R. X. Gao, Z. F. Chen, T. S. Lai, H. N. Hu, S. M. Zhou, X. J. Bai, and J. Du: *Appl. Phys. Lett.,* **93**, 162509 (2008).
8) T. Narisawa, T. Hasegawa, S. Ishio, and H. Yamane: *J. Appl. Phys.,* **109,** 033918 (2011).
9) T. Seki, H. Iwama, T. Shima, and K. Takanashi: *J. Phys. D: Appl. Phys.,* **44,** 335001 (2011).
10) S. Matsumoto, and T. Shima: *J. Phys. Conf. Ser.*, **266**, 012038 (2011).
11) S. Matsumoto, H. Iwama, and T. Shima: *J. Magn. Soc. Jpn.,* **36**, 86 (2012).
12) K. F. Dong, H. H. Li, and J. S. Chen: *J. Magn. Magn. Mater.*, **347**, 165 (2013).
13) K. F. Dong, H. H. Li, and J. S. Chen: *J. Appl. Phys.,* **113,** 233904 (2013).
14) J. Wang, S. Hata, Y. K. Takahashi, H. Sepehri-Amin, B. S. D. Ch. S. Varaprasad, T. Shiroyama, T. Schrefl, and K. Hono: *Acta. Mater.,* **91**, 41 (2015).
15) S. Yamamoto, Y. Morimoto, T. Ono, and M. Takano: *Appl. Phys. Lett.,* **87**, 032503 (2005).
16) T. Shima, K. Takanashi, Y. K. Takahashi, and K. Hono: *Appl. Phys. Lett.,* **88**, 063117 (2006).
17) A. Hotta, T. Ono, M. Hatayama, K. Tsumura, N. Kikuchi, S. Okamoto, and T. Shimatsu: *J. Appl. Phys.,* **115,** 17B712 (2014).
18) K. Wasa, M. Kitabatake, and H. Adachi: THIN FILM MATERIALS TECHNOLOGY Sputtering of Compound Materials, (2004) Springer Verlag, Heidelbrg-New York.
19) W. F. Gale, and T. C. Totemeler: Smithells Metals Reference Book (2004) ELSEVIER, Oxford.
20) K. H. J. Buschow: Handbook of Magnetic materials **19,** (2011) ELSEVIER, Amsterdam.
21) T. Shima, T. Moriguchi, S. Mitani, and K. Takanashi: *Appl. Phys. Lett.,* **80**, 288 (2002).
22) T. Shima, K. Takanashi, G. Q. Li, and S. Ishio: *Mater. Trans.,* **44**, 8, 1508 (2003).

<Paper>

Effect of Si/Fe Composition, Substrate Temperature, and Substrate Orientation on the Structure and Magnetic Properties of Fe-Si Alloy Film

Takuya Aida[1], Tetsuroh Kawai[1], Mitsuru Ohtake[1,2], Masaaki Futamoto[1],
Fumiyoshi Kirino[3], and Nobuyuki Inaba[4]

[1]Faculty of Science and Engineering, Chuo University, *1-13-27 Kasuga, Bunkyo-ku, Tokyo 112-8551, Japan*
[2]Faculty of Engineering, Kogakuin University, *2665-1 Nakano, Hachioji, Tokyo 192-0015, Japan*
[3]Graduate School of Fine Arts, Tokyo University of the Arts, *12-8 Ueno-Koen, Taito-ku, Tokyo 110-8714, Japan*
[4]Faculty of Engineering, Yamagata University, *4-3-16 Jyonan, Yonezawa, Yamagata 992-8510, Japan*

$Fe_{100-x}Si_x$ (x = 0, 2, 6, 10 at. %) alloy films are prepared on MgO single-crystal substrates of (001), (110), and (111) orientations at temperatures ranging between room temperature and 600 °C by using a radio-frequency magnetron sputtering system. The film growth behavior, the crystallographic properties, and the magnetic properties are systematically investigated. Fe-Si(001) single-crystal films with bcc structure are formed on MgO(001) substrates. The Fe-Si films deposited on MgO(110) substrates consist of epitaxial bcc(211) bi-crystals whose orientations are rotated around the film normal by 180° each other. Fe-Si films grow epitaxially on MgO(111) substrates with two types of bcc(110) variant whose crystallographic orientations are similar to the Nishiyama-Wasserman and the Kurdjumov-Sachs relationships. The orientation dispersion of Fe-Si film decreases with decreasing the Si composition, with increasing the substrate temperature, and with decreasing the index of the substrate crystallographic plane. The Fe-Si films deposited on MgO(001) and (110) show in-plane magnetic anisotropies reflecting the magnetocrystalline anisotropies of bulk Fe-Si alloy crystals. The Fe-Si films deposited on MgO(111) show nearly isotropic in-plane magnetic anisotropies that possibly come from the multiple variant structure. The coercivity decreases with increasing the Si composition and with decreasing the substrate temperature.

Keywords: $Fe_{100-x}Si_x$ (x = 0 – 10 at. %) alloy, epitaxial thin film, MgO single-crystal substrate, soft magnetic property

1. Introduction

Fe-Si alloy is a typical soft magnetic material and has been used in transformers, motors, etc. It is known that the crystallographic structure and the magnetic properties change depending on the Si composition and the processing temperature[1,2]. In particular, Fe – 3 wt. % Si (≈ Fe – 6 at. % Si) alloys are widely used in the related industries because of excellent soft magnetic properties with high permeability, high saturation magnetization (M_s), and low coercivity (H_c). In such applications, grain-oriented or non-grain-oriented silicon steel sheets are generally employed, where the overall magnetic properties are influenced by the structure consisting of crystal grains. Therefore, understanding the magnetic properties of Fe-Si crystals with different orientations is very important to further improve the overall soft magnetic properties.

There are some reports on the investigations concerning the relationships of Si/Fe composition and crystallographic orientation with respect to the magnetic properties by using bulk Fe-Si single-crystal materials[3,4]. However, it is not easy to prepare bulk crystal samples systematically varying the Si composition or the crystallographic orientation. In contrast, it seems possible to prepare thin film crystal samples, where the composition and the crystallographic orientation can be respectively controlled by the target composition and the orientation of single-crystal substrate. In the present study,

$Fe_{100-x}Si_x$ (at. %, x = 0 – 10) alloy thin films are prepared on MgO single-crystal substrates of (001), (110). and (111) orientations at temperatures ranging from room temperature (RT) to 600 °C. The influences of film composition, substrate temperature, and substrate orientation on the detailed structure and the magnetic properties are systematically investigated.

2. Experimental Procedure

$Fe_{100-x}Si_x$ (x = 0, 2, 6, 10 at. %) alloy films of 40 nm thickness were deposited on polished MgO substrates of (001), (110), and (111) orientations by using a radio-frequency (RF) magnetron sputtering system equipped with a reflection high-energy electron diffraction (RHEED) facility. The base pressures were lower than 4×10^{-7} Pa. Before film formation, substrates were heated at 600 °C for 1 hour to obtain clean surfaces. The distance between a target and substrates was fixed at 150 mm. The Ar gas pressure was kept constant at 0.67 Pa. The RF powers for Fe, $Fe_{98}Si_2$, $Fe_{94}Si_6$, and $Fe_{90}Si_{10}$ targets were respectively fixed at 52, 59, 54, and 54 W, where the deposition rates were 0.02 nm/s. The substrate temperature was varied in a range from RT to 600 °C.

The surface structure was studied by RHEED. The resulting film structure was investigated by $2\theta/\omega$ scan out-of-plane and $2\theta\chi/\varphi$ scan in-plane X-ray diffractions (XRDs) with Cu-Kα radiation (λ = 0.15418 nm). The surface morphology was observed by atomic force
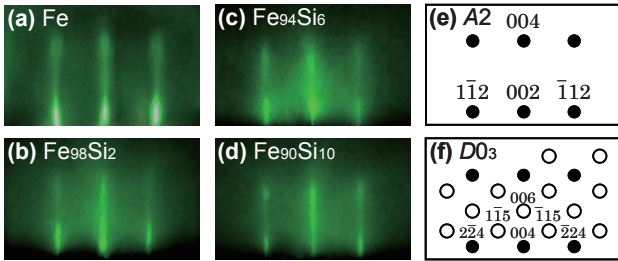
Fig. 1 RHEED patterns observed for (a) Fe, (b) Fe98Si2, (c) Fe94Si6, and (d) Fe90Si10 films prepared on MgO(001) substrates at 200 °C. [(e), (f)] Schematic diagrams of RHEED patterns of (e) $A2$(001) and (f) $D0_3$(001) single-crystal surfaces simulated by using the lattice constants of bulk (e) Fe (a = 0.2866 nm[6]) and (f) Fe3Si (a = 0.5653 nm[7]), respectively. The incident electron beam is parallel to (a)–(d) MgO[100], (e) $A2$[110], or (f) $D0_3$[110]. The filled and open circles in (f) respectively correspond to the fundamental and the superlattice reflections.

microscopy (AFM). The magnetization curves were measured by vibrating sample magnetometry.

3. Results and Discussion

3.1 Effect of Si/Fe composition

Figures 1(a)–(d) show the RHEED patterns observed for $Fe_{100-x}Si_x$ alloy films with x = 0 – 10 at. % deposited on MgO(001) substrates at 200 °C. Clear diffraction patterns are observed for all the investigated compositions. The Fe-Si films grow epitaxially on the substrates. bcc-based disordered $A2$ phase and ordered $D0_3$ phase exist in Fe-rich region of the bulk Fe-Si binary alloy phase diagram[5]. Diffraction patterns for $A2$(001) and $D0_3$(001) surfaces were thus calculated by using the lattice constants of bulk Fe (a = 0.2866 nm[6]) and Fe3Si (a = 0.5653 nm[7]), respectively. Figures 1(e) and (f) are the schematic diagrams of the simulated patterns of $A2$(001) and $D0_3$(001) surfaces, respectively. The observed RHEED patterns are corresponding to the pattern simulated for $A2$(001) surface. The epitaxial orientation relationship is determined as

$A2$(001)[110] ∥ MgO(001)[100].

Fe-Si(001) single-crystal films with $A2$ structure are obtained on the substrates, where the Fe-Si(001) lattice is rotated around the film normal by 45° with respect to the MgO(001) lattice. In this configuration, the lattice mismatch slightly increases from −4.0% to −4.4% with increasing the x value from 0 to 10 at. %, where the lattice constants of bulk MgO (a = 0.4217 nm[8]), Fe (a = 0.2866 nm[6]), and Fe89.5Si10.5 (a = 0.2853 nm[9]) crystals are used.

Figures 2(a-1)–(d-1) and 3(a-1)–(d-1) show the out-of-plane and in-plane XRD patterns measured for Fe-Si films. Here, the scattering vector of in-plane XRD is parallel to MgO[1$\bar{1}$0]. Out-of-plane $A2$(002) and in-plane $A2$(200) fundamental reflections are recognized, whereas out-of-plane $D0_3$(002) and in-plane $D0_3$(200)
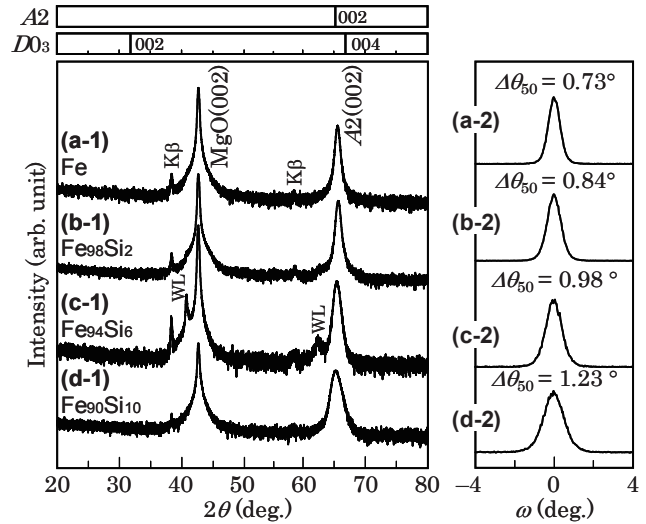
Fig. 2 (a-1)–(d-1) Out-of-plane XRD patterns measured for (a) Fe, (b) Fe98Si2, (c) Fe94Si6, and (d) Fe90Si10 films prepared on MgO(001) substrates at 200 °C. (a-2)–(d-2) Rocking curves measured by fixing the diffraction angle of 2θ at the peak angles of $A2$(002) reflections in the patterns of (a-1)–(d-1), respectively. The intensity is shown in (a-1)–(d-1) logarithmic or (a-2)–(d-2) linear scale.
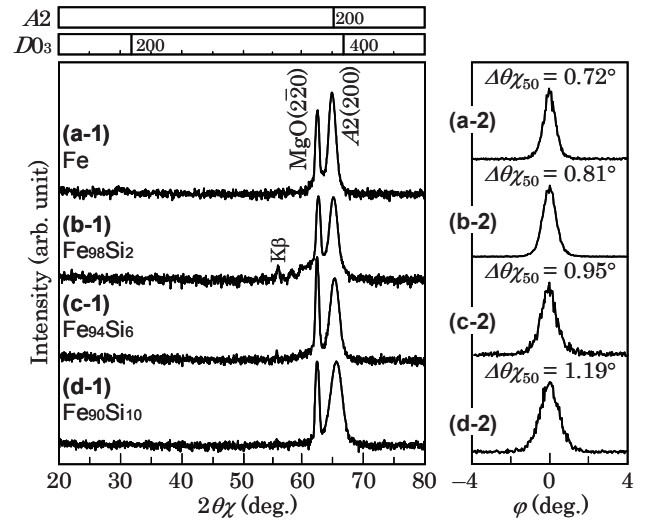
Fig. 3 (a-1)–(d-1) In-plane XRD patterns measured for (a) Fe, (b) Fe98Si2, (c) Fe94Si6, and (d) Fe90Si10 films prepared on MgO(001) substrates at 200 °C. The scattering vector is parallel to MgO[110]. (a-2)–(d-2) Rocking curves measured by fixing the diffraction angle of $2\theta\chi$ at the peak angles of $A2$(200) reflections in the patterns of (a-1)–(d-1), respectively. The intensity is shown in (a-1)–(d-1) logarithmic or (a-2)–(d-2) linear scale.

superlattice reflections are absent. The XRD confirms the crystal structure and the epitaxial orientation relationship determined by RHEED.

Figure 4(a) shows the Si composition dependences of lattice constants, a and c, of Fe-Si film. The lattice constants are calculated by using the relation of $(a, c) = (2d_{A2(200)}, 2d_{A2(002)})$. The Fe-Si lattices are slightly
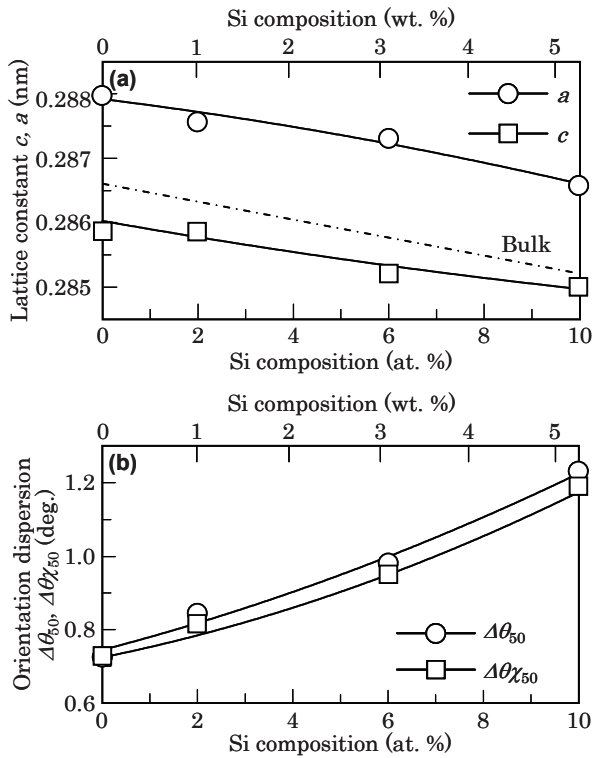
Fig. 4 Compositional dependences of (a) lattice constants of *a* and *c* and (b) orientation dispersion values of $\Delta\theta_{50}$ and $\Delta\theta\chi_{50}$ of Fe-Si film prepared on MgO(001) substrate at 200 °C. The lattice constants of bulk Fe-Si crystals are cited from Ref. 9.

Fig. 5 Magnetization curves measured for (a) Fe, (b) Fe$_{98}$Si$_2$, (c) Fe$_{94}$Si$_6$, and (d) Fe$_{90}$Si$_{10}$ films prepared on MgO(001) substrates at 200 °C.

Fig. 6 Compositional dependences of (a) H_c and (b) M_s values of Fe-Si films prepared on MgO(001) substrate at 200 °C.

deformed along the *c*-axis due to accommodation of lattice misfits of about –4%. With increasing the Si composition, *a* and *c* values are decreasing. The out-of-plane and in-plane orientation dispersions ($\Delta\theta_{50}$, $\Delta\theta\chi_{50}$) are respectively estimated as the full widths at half maximum of rocking curves measured by fixing the diffraction angles of 2θ and $2\theta\chi$ at the peak angles of out-of-plane $A2(002)$ and in-plane $A2(200)$ reflections, as shown in Figs. 2(a-2)–(d-2) and 3(a-2)–(d-2). Figure 4(b) shows the Si composition dependences of $\Delta\theta_{50}$ and $\Delta\theta\chi_{50}$. With increasing the Si composition, $\Delta\theta_{50}$ and $\Delta\theta\chi_{50}$ values are increasing. These results indicate that Si composition in Fe-Si film affects delicately the crystal unit cell size and the crystallographic quality.

Figure 5 shows the magnetization curves, where the rotation angle of θ_H shows the applied field direction with respect to $A2[100]$ in $A2(001)$. These films are easily magnetized when the magnetic field is applied along $A2[100]$, while the magnetization curves measured along $A2[110]$ saturate at higher fields. Therefore, the magnetic properties of these films are reflecting the magnetocrystalline anisotropy of bulk Fe-Si crystal with $A2$ structure.

It is recognized that the magnetization curve measured along $A2[110]$ saturates at a lower magnetic field and the coercivity decreases with increasing the Si composition from 0 to 10 at. %. The magnetic property will be explained by considering magnetocrystalline

anisotropy energy. When the magnetization rotates in $A2(001)$, the magnetic free energy is expressed as
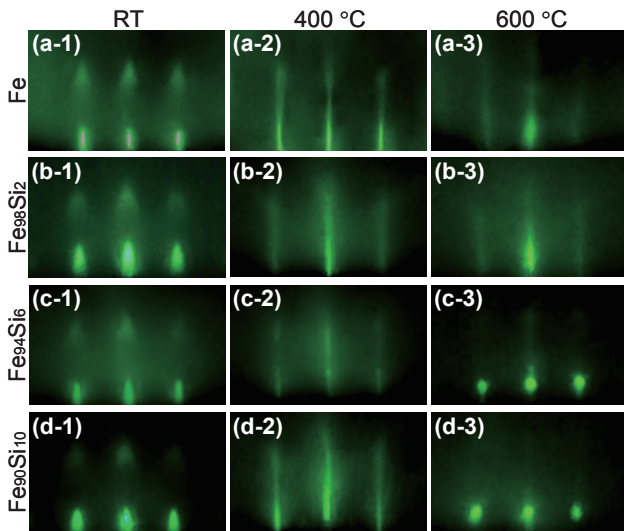
Fig. 7 RHEED patterns observed for (a) Fe, (b) $Fe_{98}Si_2$, (c) $Fe_{94}Si_6$, and (d) $Fe_{90}Si_{10}$ films prepared on MgO(001) substrates at (a-1)–(d-1) RT, (a-2)–(d-2) 400 °C, and (a-3)–(d-3) 600 °C. The incident electron beam is parallel to MgO[100].

Fig. 8 Substrate temperature dependences of (a) c and (b) a values of Fe, $Fe_{98}Si_2$, $Fe_{94}Si_6$, and $Fe_{90}Si_{10}$ films prepared on MgO(001) substrates.

$$E_a = \frac{1}{8} \cdot K_1 \cdot (1 - \cos 4\theta_M), \tag{1}$$

where K_1 is the magnetic anisotropy energy and θ_M is the direction of magnetization. For Fe and Fe-Si alloy, K_1 is positive. Then, E_a becomes minimum at $\theta_M = 0°$, 90° and becomes maximum at $\theta_M = 45°$. Therefore, $A2$[100] is the easy magnetization axis and $A2$[110] is the hard magnetization axis. This calculation is well explaining the measured magnetization curves. Figure 6 shows the Si composition dependences of coercivity (H_c) and saturation magnetization (M_s). Here, M_s value is regarded as the magnetization of Fe-Si film measured at 5 kOe. With increasing the Si composition from 0 to 10 at. %, the M_s value decreases linearly by about 11 %, and the H_c value decreases from 24 to 16 Oe reflecting the soft magnetic property of Fe-Si alloy.

3.2 Effect of substrate temperature

Figure 7 shows the RHEED patterns observed for Fe-Si films with different Si compositions grown on MgO(001) substrates at RT, 400, and 600 °C. Clear diffraction patterns corresponding to $A2$(001) surface are recognized for all the compositions, whereas any patterns corresponding to $D0_3$(001) surface are not recognized.

Figure 8 shows the substrate temperature dependences on lattice constants, a, and c, of Fe-Si films with different Si compositions. With increasing the substrate temperature, c value increases, while a value decreases for all the Si compositions.

Figure 9 shows the substrate temperature dependences on out-of-plane and in-plane orientation dispersions, $\Delta\theta_{50}$ and $\Delta\theta\chi_{50}$. With increasing the substrate temperature, the $\Delta\theta_{50}$ and $\Delta\theta\chi_{50}$ values decreases for all the Si compositions. The

Fig. 9 Substrate temperature dependences of (a) $\Delta\theta_{50}$ and (b) $\Delta\theta\chi_{50}$ of Fe, $Fe_{98}Si_2$, $Fe_{94}Si_6$, and $Fe_{90}Si_{10}$ films prepared on MgO(001) substrates.

crystallographic quality of Fe-Si film is improving possibly through relaxation of film stress caused by lattice mismatch with the substrate.

Figure 10 shows the AFM images observed for Fe-Si films with different Si compositions deposited at different temperatures. The films deposited at RT, 200, and 400 °C have flat surfaces with the arithmetical mean roughness (R_a) values less than 2 nm. On the
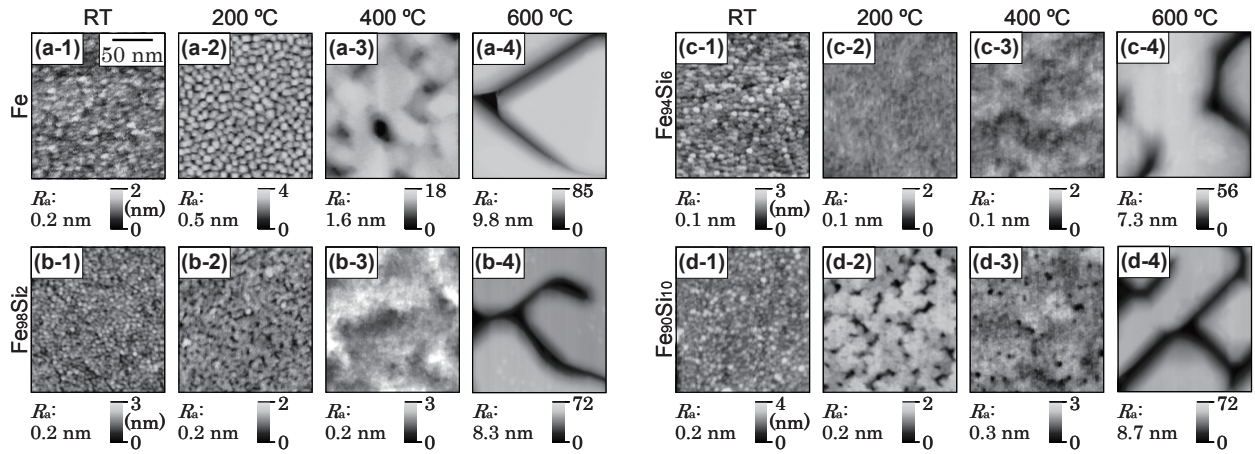
Fig. 10 AFM images observed for (a) Fe, (b) Fe$_{98}$Si$_2$, (c) Fe$_{94}$Si$_6$, and (d) Fe$_{90}$Si$_{10}$ films prepared on MgO(001) substrates at (a-1)–(d-1) RT, (a-2)–(d-2) 200 °C, (a-3)–(d-3) 400 °C, and (a-4)–(d-4) 600 °C.
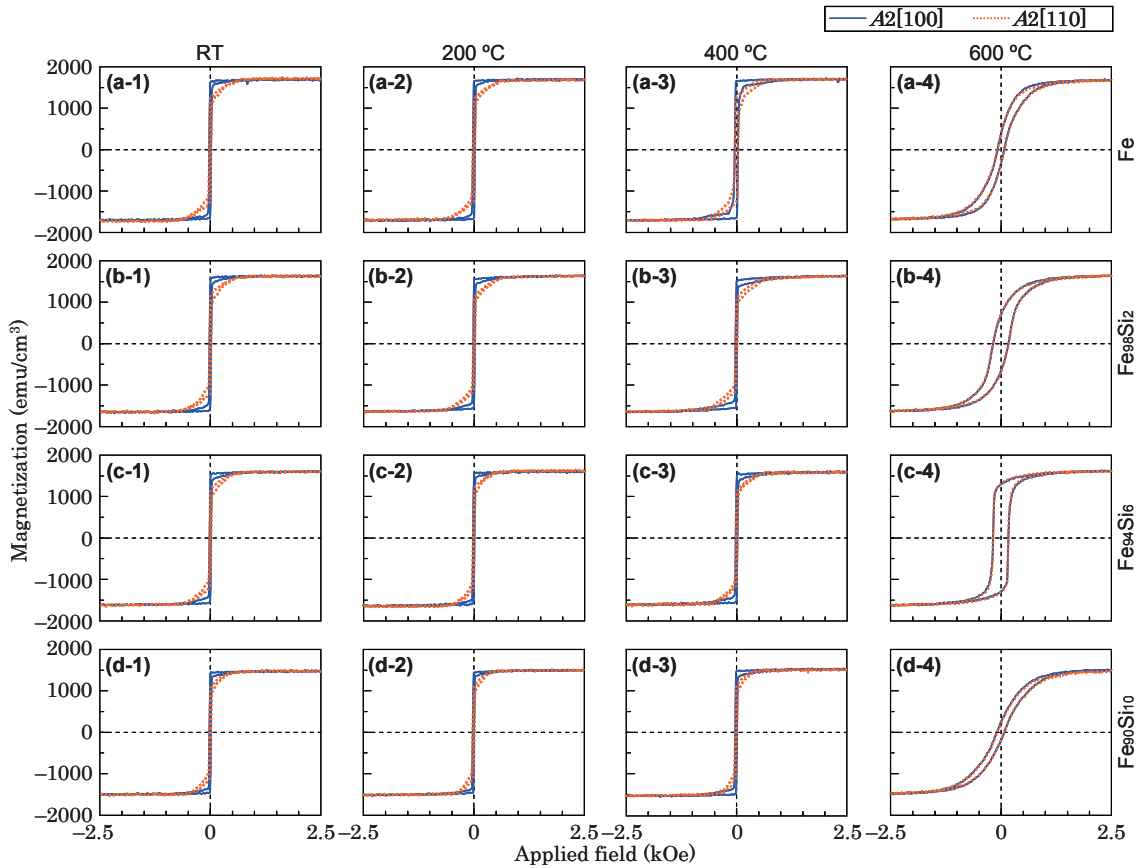
Fig. 11 Magnetization curves measured for (a) Fe, (b) Fe$_{98}$Si$_2$, (c) Fe$_{94}$Si$_6$, and (d) Fe$_{90}$Si$_{10}$ films prepared on MgO(001) substrates at (a-1)–(d-1) RT, (a-2)–(d-2) 200 °C, (a-3)–(d-3) 400 °C, and (a-4)–(d-4) 600 °C.

contrary, the R_a values of films deposited at 600 °C are greater than 7 nm, where large islands with faceted faces are formed as shown in Figs. 10(a-4)–(d-4). It is considered that migrations of deposited atoms are enhanced at a higher substrate temperature. The variation of surface roughness as a function of substrate temperature is similar in these Fe-Si films.

Figure 11 shows the magnetization curves of Fe-Si films at different substrate temperatures. The films deposited at RT, 200, and 400 °C show the magnetic properties reflecting the magnetocrystalline anisotropy of bulk Fe-Si crystal with $A2$ structure. With increasing the substrate temperature up to 600 °C, the difference in the curves measured along $A2$[110] and $A2$[100] becomes small. The films are almost magnetically isotropic in in-plane measurements. The reason is possibly due to the shape anisotropy caused by the surface undulation as shown in Figs. 10(a-4)–(d-4).
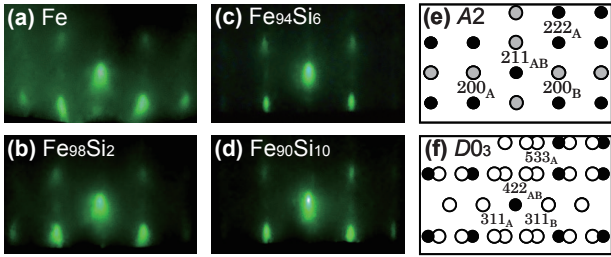
Fig. 12 RHEED patterns observed for (a) Fe, (b) Fe98Si2, (c) Fe94Si6, and (d) Fe90Si10 films prepared on MgO(110) substrates at 200 °C. [(e), (f)] Schematic diagrams of RHEED patterns of (e) $A2(211)$ and (f) $D0_3(211)$ single-crystal surfaces simulated by using the lattice constants of bulk (e) Fe and (f) Fe₃Si, respectively. The incident electron beam is parallel to (a)–(d) MgO[001]. The filled and open circles in (f) respectively correspond to the fundamental and the superlattice reflections. The reflections indicated by the gray circles in (e) show that the $A2(211)$ plane has a reconstructed surface of $p(3\times1)$.
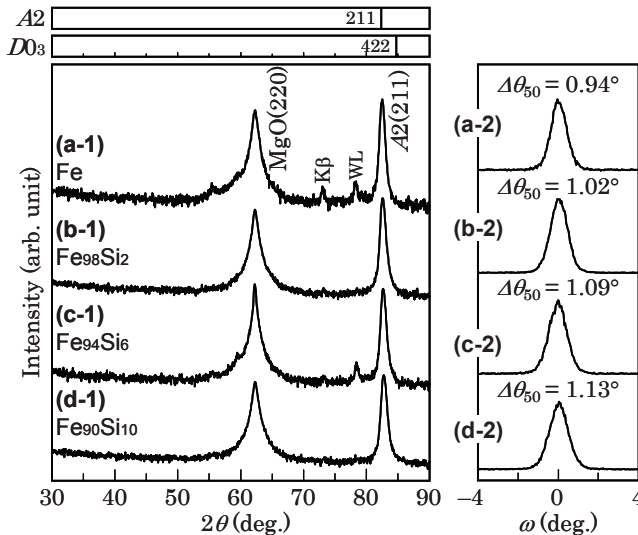
Fig. 13 (a-1)–(d-1) Out-of-plane XRD patterns measured for (a) Fe, (b) Fe98Si2, (c) Fe94Si6, and (d) Fe90Si10 films prepared on MgO(110) substrates at 200 °C. (a-2)–(d-2) Rocking curves measured by fixing the diffraction angle of 2θ at the peak angles of $A2(211)$ reflections in the patterns of (a-1)–(d-1), respectively. The intensity is shown in (a-1)–(d-1) logarithmic or (a-2)–(d-2) linear scale.

3.3 Effect of substrate orientation

Figures 12(a)–(d) show the RHEED patterns observed for Fe-Si films with different Si compositions deposited on MgO(110) substrates at 200 °C. Clear diffraction patterns corresponding to $A2(211)$ surface are recognized, whereas diffractions corresponding to $D0_3(211)$ surface are not observed, where the schematic diagrams of RHEED patterns from $A2(211)$ and $D0_3$ (211) are respectively shown in Figs. 12(e) and (f). The $A2(211)$ RHEED pattern consists of two reflections, as shown by the spots A and B in the diagram of Fig. 12(e).
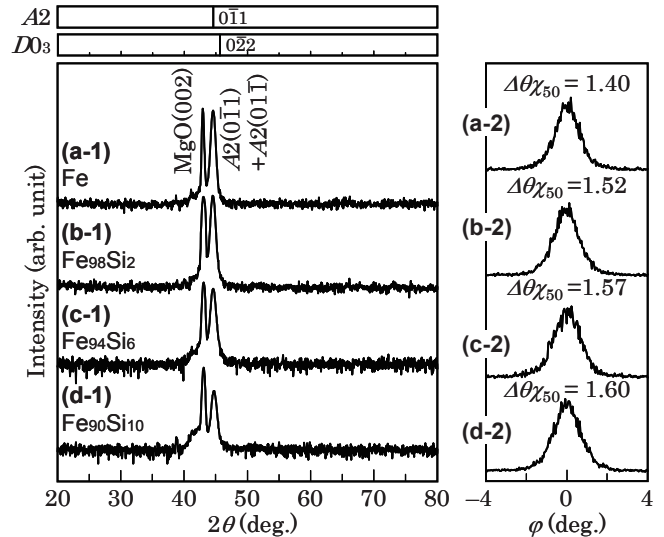
Fig. 14 (a-1)–(d-1) In-plane XRD patterns measured for (a) Fe, (b) Fe98Si2, (c) Fe94Si6, and (d) Fe90Si10 films prepared on MgO(110) substrates at 200 °C. The scattering vector is parallel to MgO[001]. (a-2)–(d-2) Rocking curves measured by fixing the diffraction angle of $2\theta\chi$ at the peak angles of $A2(0\bar{1}1) + A2(01\bar{1})$ reflections in the patterns of (a-1)–(d-1), respectively. The intensity is shown in (a-1)–(d-1) logarithmic or (a-2)–(d-2) linear scale.
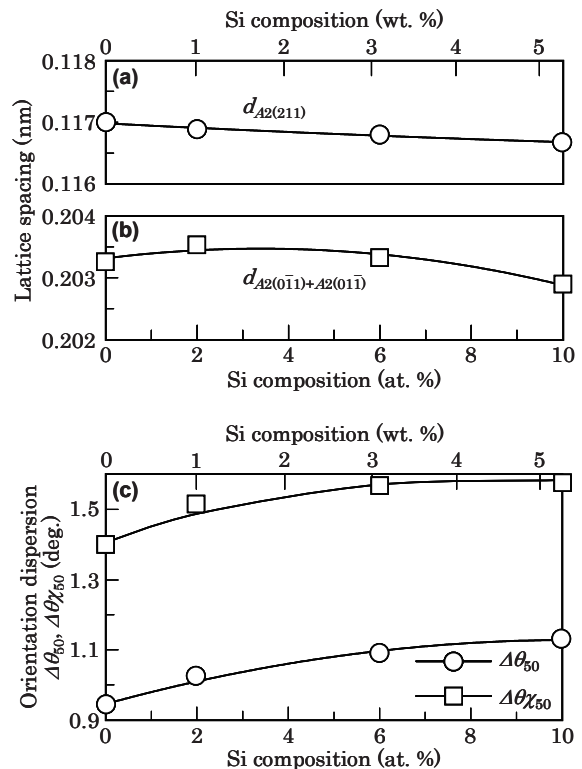
Fig. 15 Compositional dependences of (a) $d_{A2(211)}$, (b) $d_{A2(0\bar{1}1)+A2(01\bar{1})}$, and (c) $\Delta\theta_{50}$ and $\Delta\theta\chi_{50}$ of Fe-Si film prepared on MgO(110) substrate at 200 °C.

The epitaxial orientation relationship is determined from the RHEED observation as follows,

$A2(211)[0\bar{1}1] \parallel MgO(110)[001]$,　　　　(type A)

$A2(211)[01\bar{1}] \parallel MgO(110)[001]$.　　　　(type B)

The Fe-Si(211) films consist of two types of variant whose orientations are rotated around the film normal by 180° each other. In this configuration, the lattice misfit value differs depending on the in-plane direction at the Fe-Si/MgO interface. The lattice misfit value

along MgO[001] is about −4%. Although there exists a fairly large mismatch of around −17% along MgO[110], epitaxial growth of Fe-Si crystal is taking place. This type of epitaxial growth where misfit dislocations are introduced at the interface is reported for the Cr/MgO system[10,11]. The mismatch is considered to be reduced through introduction of misfit dislocations in the film around the Fe-Si/MgO interface.
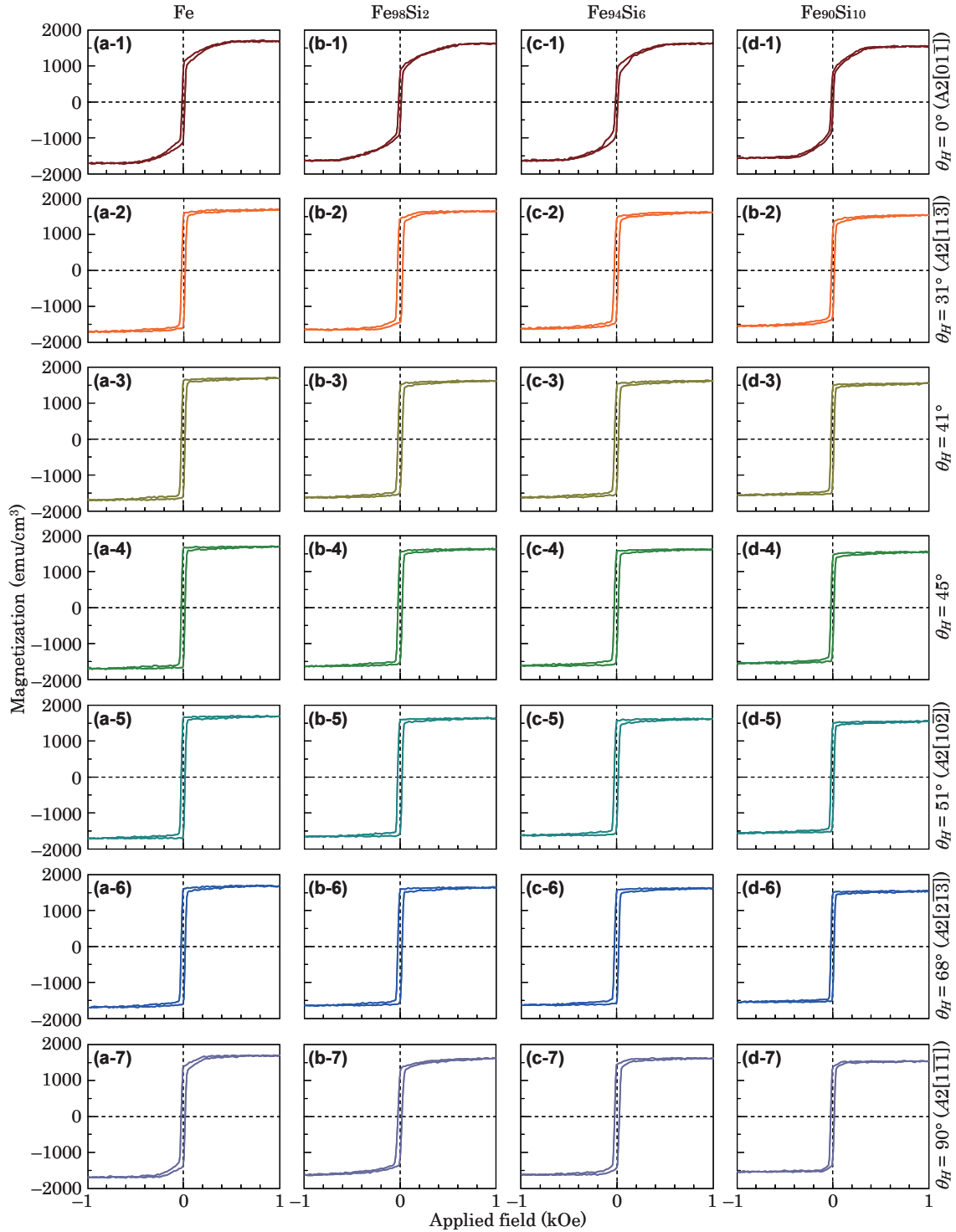
Fig. 16 Magnetization curves measured for (a) Fe, (b) Fe98Si2, (c) Fe94Si6, and (d) Fe90Si10 films prepared on MgO(110) substrates at 200 °C.

Figures 13(a-1)–(d-1) show the out-of-plane XRD patterns of Fe-Si films deposited on MgO(110) substrates. $A2(211)$ reflections are recognized, whereas $D0_3(211)$ reflections are not recognized. Figures 14(a-1)–(d-1) show the in-plane XRD patterns. Only the reflections from $A2$ crystals and the MgO substrates are recognized for these films. Figure 15 shows the Si composition dependences of lattice spacing, $d_{A2(211)}$ and $d_{A2(0\bar{1}1)+A2(01\bar{1})}$, and orientation dispersion of $\Delta\theta_{50}$ and $\Delta\theta\chi_{50}$ of these films. With increasing the Si composition, the $d_{A2(211)}$ and $d_{A2(0\bar{1}1)+A2(01\bar{1})}$ values are slightly decreasing, whereas the $\Delta\theta_{50}$ and $\Delta\theta\chi_{50}$ values are increasing similar to the case of Fe-Si/MgO(001) system.

Figures 16(a)–(d) show the magnetization curves of Fe-Si films deposited on MgO(110) substrates. Here, θ_H is the direction of magnetic field applied to the sample expressed in angle measured from $A2[01\bar{1}]$ direction in the $A2(211)$ film plane. These films are easily magnetized when the magnetic field is applied along around $\theta_H = 45°$, while the magnetization curves measured along $\theta_H = 0°$ and $90°$ saturate at higher fields. Figure 17 shows the pole-figure maps indicating the distribution of low-index planes including $A2\{100\}$ planes. The angle of $A2[01\bar{1}]$ and in-plane component of $A2(010)$ is 41°. The magnetic free energy is written in the following equation when the magnetization rotates in (211) plane,

$$E_a = \frac{1}{12} \cdot K_1 \cdot (4 - 8\cos^2\theta_M + 7\cos^4\theta_M). \quad (2)$$

Figure 18 shows the anisotropy energy, E_a, as a function of θ_M calculated by using the equation (2). It is shown that the easy magnetization axis lies along $\theta_M = 41°$ or 139° and the first hard magnetization axis lies along $A2[1\bar{1}\bar{1}]$ and the second hard magnetization axis lies along $A2[01\bar{1}]$. When the measured magnetization curves shown in Figs. 16 are compared with the calculation, it is noted that the angle-direction of easy magnetization axis is in agreement with the calculation for all the compositions. However, the experimental data shown in Fig. 16 show that the first hard magnetization axis lies parallel to $A2[01\bar{1}]$ and the second one lies parallel to $A2[1\bar{1}\bar{1}]$. There is a difference in the order of magnetization hardness, suggesting that there exists an additional influence from the film detailed structure. The XRD data shown in Fig. 15(c) indicate that the dispersion in Fe-Si film sample varies depending on the crystallographic orientation which suggests the presence of anisotropic film distortion. Such kind of distortion may have affected the magnetocrystalline anisotropy.

Figure 19 shows the Si composition dependences of H_c and M_s values of Fe-Si film deposited on MgO(110) substrate. With increasing the Si composition from 0 to 10 at. %, the M_s value decreases linearly by about 13 %, and the H_c value decreases from 28 to 19 Oe reflecting the soft magnetic property of Fe-Si alloy.

Figures 20(a)–(d) show the RHEED patterns
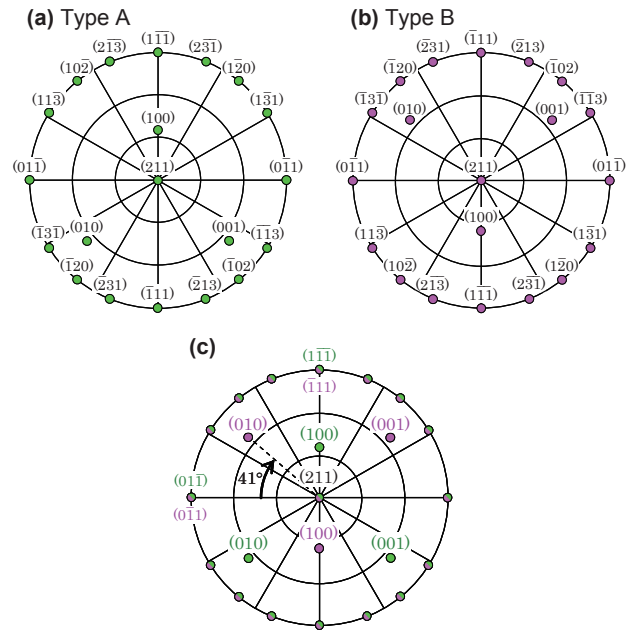
Fig. 17 Pole-figure maps showing the configurations of $A2\{100\}$ planes of (a) type A, (b) type B, and (c) type A + B, where $A2(211)$ is centered.
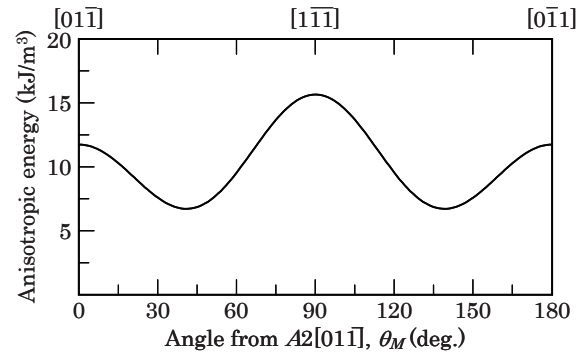

Fig. 18 Anisotropy energy in $A2(211)$ as a function of magnetization direction. K_1 is set to 47 kJ/m³.
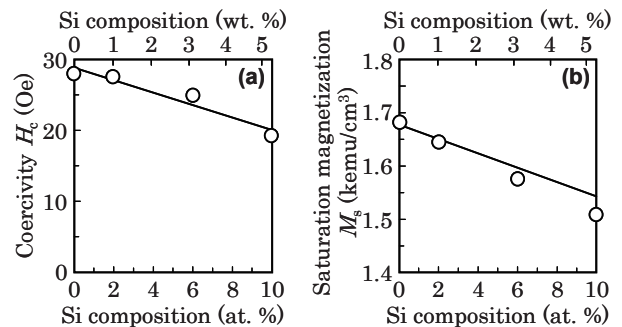

Fig. 19 Compositional dependences on (a) H_c and (b) M_s values of Fe-Si films prepared on MgO(110) substrates at 200 °C.

observed for Fe-Si films deposited on MgO(111) substrates at 200 °C. Clear RHEED patterns corresponding to $A2(110)$ texture [Fig. 20(e)] are observed. These RHEED patterns consist of two
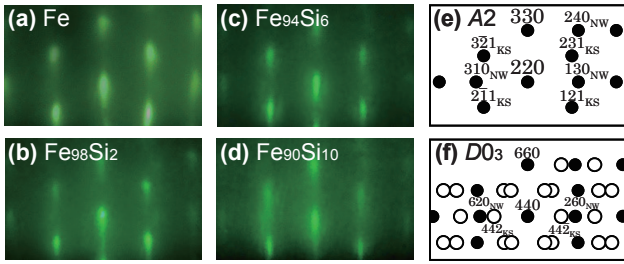
Fig. 20 RHEED patterns observed for (a) Fe, (b) Fe98Si2, (c) Fe94Si6, and (d) Fe90Si10 films prepared on MgO(111) substrates at 200 °C. [(e), (f)] Schematic diagrams of RHEED patterns of (e) $A2$(110) and (f) $D0_3$(110) single-crystal surfaces simulated by using the lattice constants of bulk (e) Fe and (f) Fe3Si, respectively. The incident electron beam is parallel to (a)–(d) MgO[1$\bar{1}$0], (e) $A2$[001] and $A2$[$\bar{1}$10], or (f) $D0_3$[001] and $D0_3$[$\bar{1}$10]. The filled and open circles in (f) respectively correspond to the fundamental and the superlattice reflections.
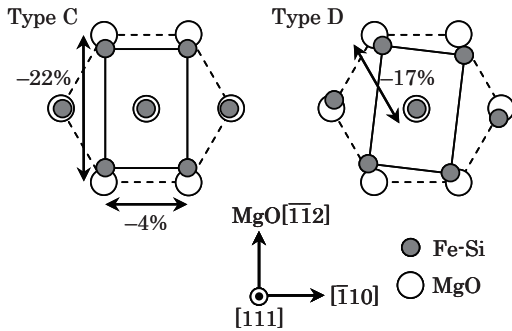
Fig. 21 Epitaxial orientation relationships of Fe-Si(110) ∥ MgO(111).

reflections, as shown by the spots C and D in the spot map of Fig 20(e). The epitaxial orientation relationship is determined by RHEED as follows,

$A2$(110)[001] ∥ MgO(111)[1$\bar{1}$0],   (type C)

$A2$(110)[11$\bar{1}$] ∥ MgO(111)[1$\bar{1}$0].   (type D)

When the atomic arrangement of MgO(111) surface which shows six-fold symmetry with respect to the perpendicular direction is considered, the $A2$(110) crystals of types C and D are interpreted to be consisting of three and six variants whose orientations are rotated around the film normal by 120° and 60° each other, respectively. The crystallographic orientation relationships of types C and D are similar to the Nishiyama-Wasserman (NW)[12,13] and the Kurdjumov-Sachs (KS)[14] relationships, respectively. In these configurations, as shown in Fig. 21, large lattice mismatches along MgO[11$\bar{2}$], –22%, and MgO[1$\bar{1}$0], –17%, are involved at the $A2$(110)type C/MgO(111) and the $A2$(110)type D/MgO(111) interfaces. The crystallographic orientation relationships observed in the present study is similar to those reported for the Fe-based alloy films with bcc(110) orientation formed on MgO(111) substrates[15,16].
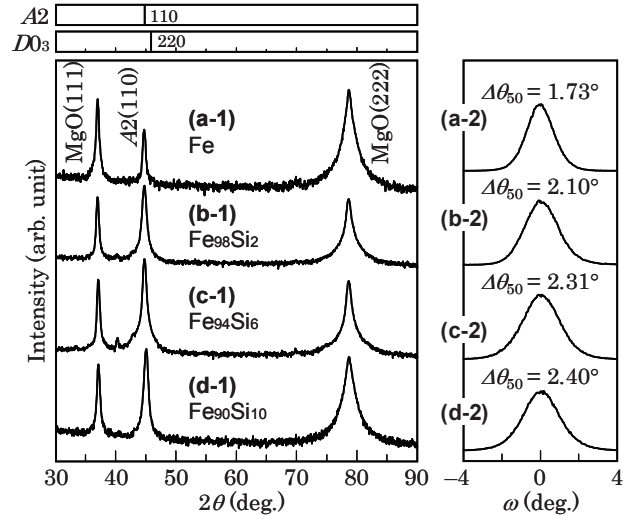
Fig. 22 (a-1)–(d-1) Out-of-plane XRD patterns measured for (a) Fe, (b) Fe98Si2, (c) Fe94Si6, and (d) Fe90Si10 films prepared on MgO(111) substrates at 200 °C. (a-2)–(d-2) Rocking curves measured by fixing the diffraction angle of 2θ at the peak angles of $A2$(110) reflections in the patterns of (a-1)–(d-1), respectively. The intensity is shown in (a-1)–(d-1) logarithmic or (a-2)–(d-2) linear scale.
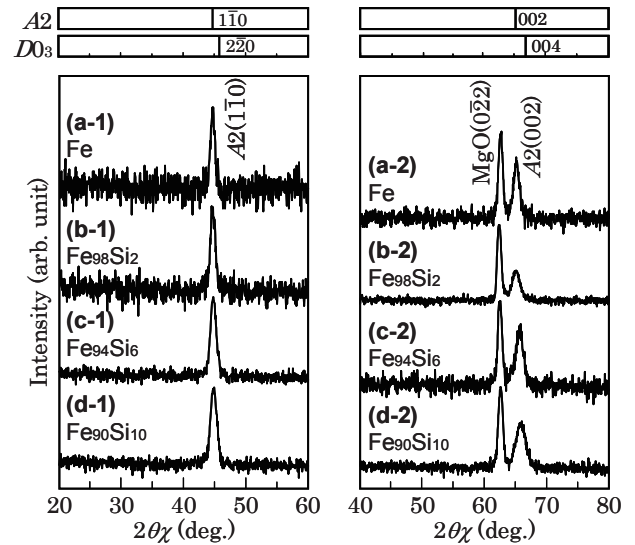
Fig. 23 (a)–(d) In-plane XRD patterns measured for (a) Fe, (b) Fe98Si2, (c) Fe94Si6, and (d) Fe90Si10 films prepared on MgO(111) substrates at 200 °C. The scattering vector is parallel to (a-1)–(d-1) MgO[11$\bar{2}$] or (a-2)–(d-2) MgO[1$\bar{1}$0]. The intensity is shown in logarithmic scale.

Figures 22(a-1)–(d-1) and 23(a-1)–(d-2) show the out-of-plane and in-plane XRD patterns of Fe-Si films deposited on MgO(111) substrates, respectively. Reflections from $A2$ crystals are recognized, whereas Reflections from $D0_3$ are not recognized.

Figure 24 shows the Si composition dependences of lattice constants, $\Delta\theta_{50}$, and $\Delta\theta\chi_{50}$. The lattice constants are calculated by using the relation of
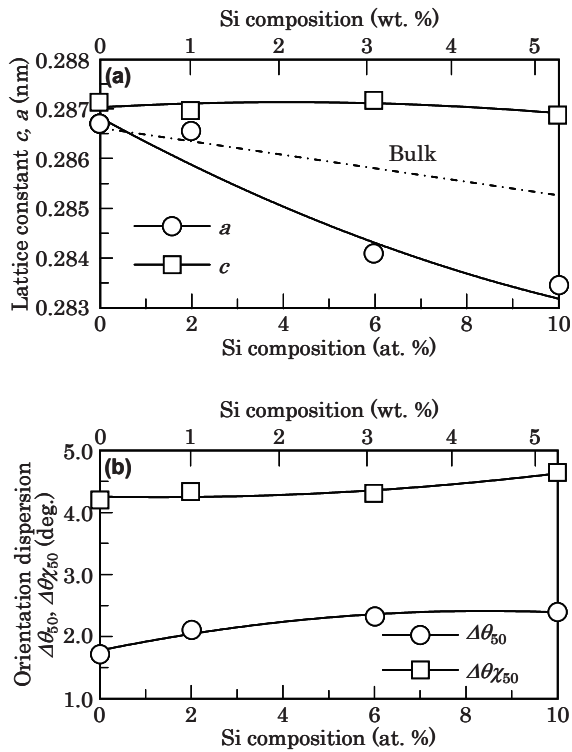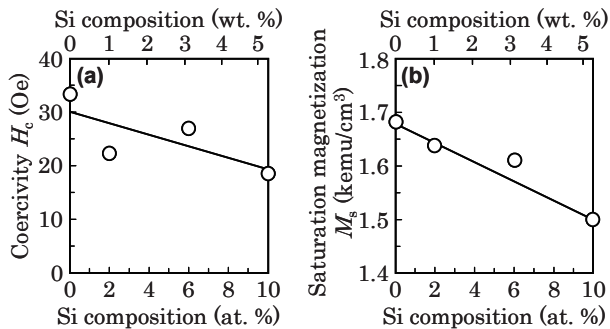
Fig. 24 Compositional dependences of (a) a and c and (b) $\Delta\theta_{50}$ and $\Delta\theta\chi_{50}$ of Fe-Si films prepared on MgO(111) substrate at 200 °C.

$$a = (d_{A2(110)}^2 + d_{A2(1\bar{1}0)}^2)^{1/2}, \tag{3}$$

$$c = 2d_{A2(002)}. \tag{4}$$

The Fe-Si lattices are slightly deformed along the c-axis in accommodation of lattice misfits of about −4%. With increasing the Si composition, the a value is decreasing, while the c value does not change much. The $\Delta\theta_{50}$ and $\Delta\theta\chi_{50}$ values are increasing with increasing the Si composition.

Figure 25 shows the magnetization curves. Here, θ_H is the direction of magnetic field applied to the sample expressed in angle measured from $A2[001]$ direction in the $A2(110)$ film plane. The magnetic free energy is written in the following equation when the magnetization rotates in (110) plane,

$$E_a = \frac{1}{32} \cdot K_1 \cdot (7 - 4\cos2\theta_M - 3\cos4\theta_M). \tag{4}$$

Figure 26 shows the anisotropy energy, E_a, as a function of θ_M calculated by using the equation (4). It is shown that the easy magnetization axis lies along $A2[001]$. Indeed, it was reported that Fe(110) single-crystal films were easily magnetized when the magnetic field was applied along the Fe[001] direction[17]. However, the films prepared in the present study show nearly isotropic in-plane magnetic anisotropies. This is possibly because that the films prepared in the present study are not single-crystals but epitaxial thin films consisting of three and six variants whose orientations are rotated around the film normal by 120° and 60° each other (Fig. 21). In this
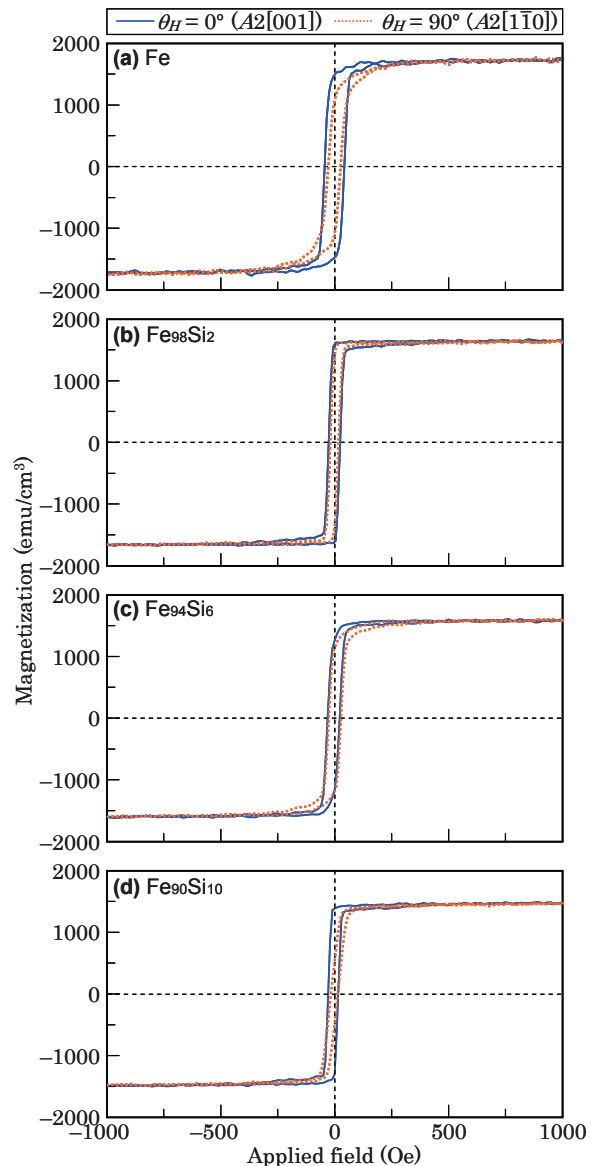
Fig. 25 Magnetization curves measured for (a) Fe, (b) Fe98Si2, (c) Fe94Si6, and (d) Fe90Si10 films grown on MgO(111) substrates at 200 °C.
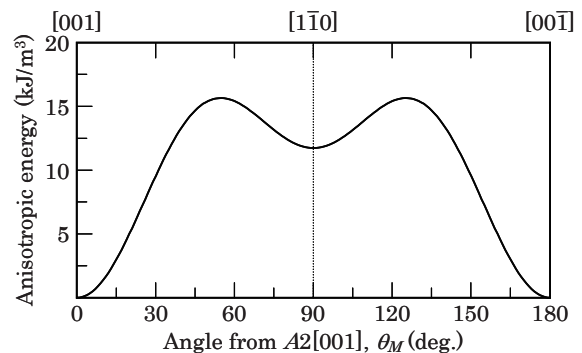
Fig. 26 Anisotropy energy in $A2(110)$ as a function of magnetization direction. K_1 is set to 47 kJ/m³.

case, the in-plane magnetic property of epitaxial thin film will be influenced by the distribution of variant

Fig. 27 Compositional dependences on (a) H_c and (b) M_s values of Fe-Si films prepared on MgO(111) substrates at 200 °C.

crystals. The almost isotropic in-plane magnetic anisotropies observed for the epitaxial thin films are due to the complex variant structure.

Figure 27 shows the compositional dependences of H_c and M_s values. With increasing the Si composition from 0 to 10 at. %, the M_s value decreases linearly by about 12 %, and the H_c value decreases from 34 to 19 Oe reflecting the soft magnetic property of Fe-Si alloy.

In the present study, $Fe_{100-x}Si_x$ ($x = 0 - 10$ at. %) epitaxial films are prepared on MgO single-crystal substrates under similar experimental conditions. It is shown that single-crystal films of (001) orientation grow on MgO(001), bi-crystalline epitaxial films with (211) orientation grow on MgO(110), and epitaxial films consisting of two types of (110) variant grow on MgO(111) substrates. Although they are epitaxial thin film crystals, differences in quality and magnetic properties are noted between these samples. For example when the $\Delta\theta_{50}$ value, out-of-plane dispersion which is a measure of crystallographic quality, is compared between the samples prepared at 200 °C, lower values are observed in the order of samples prepared on MgO(001) < MgO(110) < MgO(111) for the investigated compositional range. The $\Delta\theta_{50}$ value is increasing with increasing the Si composition for all cases. Similar tendency is also noted in the variation of $\Delta\theta\chi_{50}$, in-plane dispersion, between these samples (Figs. 4(b), 15(c), 24(b)). The results indicate that the crystallographic quality slightly degrades when deposited on an MgO single crystal with higher index plane.

Differences in coercivity are also noted between the epitaxial thin films. In-plane coercivity decreases with increasing the Si content for the epitaxial Fe-Si films grown on three kinds of crystallographic planes of MgO single-crystal substrates (Figs. 6(a), 19(a), 27(a)). When the coercivity is compared, lower values are observed in the order of samples prepared on MgO(001) < MgO(110) < MgO(111) for the compositional range of $x = 0 - 10$ at. %. The low coercivities of Fe-Si(001) epitaxial films are considered to be due to the high crystallographic quality of single-crystal with low dispersion.

In the present study, Fe-Si single crystal films of

$A2(100)$ orientation are obtained on MgO(100) substrate. The Fe-Si films prepared on MgO(110) substrate are epitaxial films of $A2(211)$ orientation with bi-crystalline structure, whereas the films formed on MgO(111) are epitaxial films of $A2(110)$ consisting of variants. By using these epitaxial thin films, it is possible to investigate the magnetic properties such as magnetostriction[18], damping constant, etc. in relation to the crystallographic orientation of Fe-Si magnetic material. The thin film growth technique can be applicable to the preparation of Fe-Si single-crystal films, for example, with $A2(110)$ by changing the substrate to GaAs(110) crystal[19].

4. Conclusion

Fe-Si alloy thin films are deposited on MgO single-crystal substrates of (001), (110), and (111) orientations at temperatures ranging between RT and 600 °C by varying the Si composition, x, from 0 to 10 at. %. The effects of composition and substrate orientation on the structure and the magnetic properties are investigated. Fe-Si(001) single-crystal films are formed on MgO(001) substrates. Fe-Si films epitaxially grown on MgO(110) substrates consist of two (211) variants whose orientations are rotated around the film normal by 180° each other. Fe-Si(110) films grow epitaxially on MgO(111) substrates with two-type variants, Nishiyama-Wasserman and Kurdjumov-Sachs relationships. The orientation dispersion of Fe-Si film decreases with decreasing the Si composition, with increasing the substrate temperature, and with decreasing the index of substrate crystallographic plane. The magnetic properties of films prepared on MgO(001) and (110) are reflecting the magnetocrystalline anisotropy of bulk Fe-Si crystal with $A2$ structure. The Fe-Si epitaxial films prepared on MgO(111) show almost isotropic in-plane magnetic anisotropies which are related with the multiple variant structure.

References

1) M. Takahashi, S. Suwabe, T. Narita, and T. Wakiyama: *J. Magn. Soc. Jpn.*, **10**, 307 (1986).
2) R. R. Rodriguez, G. A. Perez Alcazar, H. Sanchez, M. Sacilotti, and J. M. Greneche: *Phys. Status Solidi C*, **4**, 4220 (2007).
3) S. Yaegashi, T. Kurihara, and K. Satoh: *J. Magn. Soc. Jpn.*, **20**, 437 (1996).
4) L. T. Vinh, J. Chevrier, and J. Derrien: *Phys. Rev. B*, **46**, 946 (1992).
5) E. Schürmann, U. Hensgen: *Arch. Eisenhuettenwes*, **51**, 1 (1980).
6) M. Takahashi, Y. Takahashi, and H. Shoji: *IEEE Trans.*

Magn., **37**, 1937 (2001).

7) J. Waliszewski, L. Dobrzyńskia, A. Malinowskia, D. Satułaa, K. Szymańskia, W. Prandlb, Th Brückela, and O. Schärpf: *J. Magn. Magn. Mater.*, **132**, 349 (1994).

8) J. Yamashita and S. Asano: *J. Phys. Soc. Jpn.*, **52**, 3506 (1983).

9) F. C. Farquhar, H. Lipson, and A. R. Weill: *J. Iron Steel Inst.*, **152**, 457 (1945).

10) A. Nakamura, M. Koguchi, and M. Futamoto: *Jpn. J. Appl. Phys.*, **34**, 2307 (1995).

11) M. Ohtake, T. Nishiyama, K. Shikada, F. Kirino, and M. Futamoto: *J. Magn. Magn. Mater.*, **322**, 1947 (2010).

12) G. Wasserman: *Arch. Eisenhuettenwes*, **16**, 647 (1993).

13) Z. Nishiyama: *Sci. Rep. Tohoku Univ.*, **23**, 638 (1934).

14) G. Kurdjimov and G. Sachs: *Z. Phys.*, **64**, 325 (1930).

15) I. L. Grigorov, M. R. Fitzsimmons, I-Liang Siu, and J. C. Walker: *Phys. Rev. Lett.*, **82**, 5309 (1999).

16) Y. Asai, M. Ohtake, T. Kawai, and M. Futamoto: *J. Korean Phys. Soc.*, **63**, 733 (2013).

17) K. Matsubara, M. Ohtake, K. Tobari, and M. Futamoto: *Thin Solid Films*, **519**, 8299 (2011).

18) T. Kawai, T. Aida, M. Ohtake, and M. Futamoto: *J. Appl. Phys.*, **117**, 17A303 (2015).

19) M. W. Ruckman, J. J. Joyce, and J. H. Weaver: *Phys. Rev. B*, **33**, 7029 (1986).

<Paper>

Preparation and Characterization of Bi substituted gadolinium iron garnet $Bi_xGd_{3-x}Fe_5O_{12}$ films with x = 1 to 2.5 by Enhanced Metal Organic Decomposition method

D. A. Wahid, J. Sato, M. Hosoda, and H. Shimizu

Department of Electronic and Information Engineering, Tokyo University of Agriculture and Technology, 2-24-16 Naka-cho, Koganei-shi, Tokyo 184-8588, Japan

Bismuth substituted gadolinium iron garnet thin films ($Bi_xGd_{3-x}Fe_5O_{12}$) were prepared with x = 1, 2, and 2.5 on glass substrates by enhanced metal organic decomposition (EMOD) method. We mixed the solution containing Fe_2O_3, Bi_2O_3 and Gd_2O_3 carboxylates so that we could obtain desired Bi content x. X-ray diffraction (XRD), optical transmittance / reflectivity, and Faraday rotation (FR) were measured for characterizations in order to examine their dependence on annealing temperatures and different amount of Bismuth substitution (x). When $Bi_xGd_{3-x}Fe_5O_{12}$ thin films were directly prepared on glass substrates, Bi_2O_3 phase were observed by XRD measurements and with increasing Bi content x from 1 to 2, the FR increased from 1.2 to 5.8 deg./μm at the wavelength of 530 nm. FR of $Bi_{2.5}Gd_{0.5}Fe_5O_{12}$ thin films prepared directly on glass substrates were smaller (0.35 deg./μm) than those with x = 2. When $Bi_{2.5}Gd_{0.5}Fe_5O_{12}$ thin films were prepared with annealing temperature of 620ºC with $Gd_3Fe_5O_{12}$ buffer layer on glass substrates, the films showed garnet crystal structure and FR, which is comparable with that of $Bi_{2.5}Gd_{0.5}Fe_5O_{12}$ thin films prepared on (111) $(GdCa)_3(GaMgZr)_5O_{12}$ (SGGG) single crystal substrates. These results demonstrate that $Bi_xGd_{3-x}Fe_5O_{12}$ thin films can be prepared on glass substrates with controlled Bi content and that FR as high as that prepared on the SGGG substrate can be obtained by the EMOD method.

Key words: magnetic garnet, enhanced metal organic decomposition method, Faraday effect.

1. Introduction

Bismuth substituted rare-earth iron garnets have a considerable interest owing to their large magneto optic effect. Large FR with high transparency in the visible to near infrared range[1] are key properties which made the magnetic garnet materials suitable for various applications for magneto-optical device elements such as in magnetoplasmonic structure[2], optical isolators[3], circulators[4,5], and magnet photonic crystals (MPCs) used in magneto-optic spatial light modulators (MOSLM)[6-9].

Bismuth substituted gadolinium iron garnet (Bi:GdIG) is a ferrimagnetic material and shows perpendicular magnetic anisotropy, which is one of the most desirable materials for magneto optical devices owing to its high optical transmittance and extremely high magneto optical activity in the visible and near infrared regions [10,11], which enable this material to have high frequency application. FR can be controlled by Bi substitution of Gd. Therefore, it is very important to control the amount of Bi substitution in order to control and increase the FR. There are several methods to prepare the bismuth substituted rare-earth iron garnet thin films such as a laser ablation[12], a liquid phase epitaxy[13], RF magnetron sputtering[14], etc. Among them,

metal organic decomposition (MOD) method is a promising one to prepare magnetic garnet film, because it is a simple fabrication method which is composed of spin coating of the MOD solution and annealing, and guarantees high uniformity in chemical composition and purity combined with chemical stability. It was reported that $Bi_xGd_{3-x}Fe_5O_{12}$, $Bi_xY_{3-x}Fe_5O_{12}$, and $Bi_xY_{3-x}(FeGa)_5O_{12}$ thin films were prepared on gadolinium gallium garnet (GGG) [12-17] and glass substrates [18]. We have prepared Bi:GdIG thin films on GGG substrates by annealing with and without O_2 gas and investigated the crystal growth process and magnetic anisotropy[19]. The fabrication of magnetic garnet such as $Bi_{2.5}Y_{0.5}Fe_5O_{12}$ films was reported by using $Nd_2Bi_1Fe_4Ga_1O_{12}$ buffer layers on glass substrate which was fabricated by the MOD method, and FR of 13.8 deg./μm at λ = 520 nm was reported for the $Bi_{2.5}Y_{0.5}Fe_5O_{12}$ films[18]. It is important to obtain $Bi_xGd_{3-x}Fe_5O_{12}$ thin films having higher Bi content x and FR. However, it is reported that preparation of $Bi_xGd_{3-x}Fe_5O_{12}$ with high Bi content on glass substrates is difficult[12-17]. Therefore, fabrication of $Bi_xGd_{3-x}Fe_5O_{12}$ thin films with various Bi content x and characterization of FR are important. In order to investigate the effect of changing the Bi content x on FR of $Bi_xGd_{3-x}Fe_5O_{12}$ thin films by increasing the Bi content x systematically, we fabricated the $Bi_xGd_{3-x}Fe_5O_{12}$ thin

films on glass substrates by the EMOD method. Furthermore, we used the $Gd_3Fe_5O_{12}$ buffer layer in order to fabricate the $Bi_xGd_{3-x}Fe_5O_{12}$ thin films with higher x of 2.5 showing larger FR by the EMOD method.

2. Experiments

We fabricated $Bi_xGd_{3-x}Fe_5O_{12}$ thin films with $x = 1$, 2 and 2.5 at different annealing temperatures of 620°C, 650°C and 700°C on 15 mm x 15 mm glass substrate, and $Bi_xGd_{3-x}Fe_5O_{12}$ thin film with $x = 2.5$ on 12 mm x 12 mm SGGG (111) single crystal substrate and $Gd_3Fe_5O_{12}$ buffer layer / glass substrate by the EMOD method. The EMOD liquids used in this experiment are SYM-FE05 containing Fe_2O_3 carboxylates, SYM-BI05 containing Bi_2O_3 carboxylates, and SYM-GD01 containing Gd_2O_3 carboxylates by Kojundo Chemical Laboratory so that we could obtain $Bi_xGd_{3-x}Fe_5O_{12}$ thin films with desired Bi content x. Kojundo Chemical Laboratory Ltd provides their own MOD solutions, as well as EMOD solutions developed by Symetrix corporation of the United States and Kojundo Chemical Laboratory Ltd[20]. The MOD solution contains 2 – 3 kinds of metal oxides carboxylates such as Bi_2O_3, Gd_2O_3, and Fe_2O_3 carboxylates in acetic ester to prepare $Bi_xGd_{3-x}Fe_5O_{12}$ thin films. In case of preparation of $Bi_xGd_{3-x}Fe_5O_{12}$ thin films by the MOD method, Bi content x is fixed. On the other hand, the EMOD solution contains one metal oxide carboxylate in xylene and can be mixed with other EMOD solutions containing other metal oxide. Therefore it is possible to prepare the $Bi_xGd_{3-x}Fe_5O_{12}$ thin films in any proportion of Bi content x, which enables greater degree of freedom and more precise control of composition in order to prepare $Bi_xGd_{3-x}Fe_5O_{12}$ thin films. When we prepare the $Bi_xGd_{3-x}Fe_5O_{12}$ thin films with different Bi content x by the EMOD method, the EMOD solutions of Fe_2O_3 carboxylate (product name SYM-FE05), Bi_2O_3 carboxylate (product name SYM-BI05), and Gd_2O_3 carboxylate (product name SYM-GD05), are mixed and combined for different Bi content x, which is advantage compared with the MOD method. The selected components were mixed in the desired stoichiometric ratio of $Bi_xGd_{3-x}Fe_5O_{12}$ with different value of $x = 1$, 2 and 2.5 and stirred well. The solution was then filtered by advantec filter paper. The solution was spin-coated in 2 steps process of 500 rpm for 10 s and 2000 rpm for 20 s, followed by drying on a hot plate at 120°C for 10 min and the solvent are evaporated. In order to decompose the organic materials and obtain the amorphous metal oxide films, the samples were pre-annealed at 550°C for 10 min. The thickness by single spin coating step is typically 20 - 30 nm. The conditions for spin coating, drying, and pre-annealing were fixed. We changed the mixing ratio of the SYM-BI05 and SYM-GD01 solutions in order to change the Bi substitution x in $Bi_xGd_{3-x}Fe_5O_{12}$ thin films, and changed the final-annealing temperature. The thickness of the samples slightly changes with the spin coating speed, time and viscosity of the solutions. Spin coating, drying and pre-annealing were repeated for 11 times to obtain an appropriate thickness. Spin coating, drying and pre-annealing, were repeated 6 times for the $Bi_xGd_{3-x}Fe_5O_{12}$ films on the $Gd_3Fe_5O_{12}$ buffer layer / glass substrate. Also, we prepared a $Bi_xGd_{3-x}Fe_5O_{12}$ film on SGGG (111) single crystal substrate for a reference sample to compare the FR. The amorphous $Bi_xGd_{3-x}Fe_5O_{12}$ films prepared by pre-annealing process were then annealed at 620, 650 and 700 °C for 2 hours for crystallization (final annealing). The pressure during the annealing was atmospheric pressure. Bi:GdIG thin films prepared in this study were characterized by x-ray diffraction (XRD), optical transmittance, optical reflectivity, and FR spectra. All the measurement was done at room temperature. We measured the XRD from the central part of the samples. The diameter d of the x-ray beam is about 0.4 mm. Therefore, the measurement results of the XRD show average crystallinity of the samples over $d = 0.4$ mm. We estimated the thickness of the samples from the optical reflectivity spectra, and discussed the relationship between XRD and FR spectra.

3. Results and Discussion

Figure 1 shows the optical reflectivity spectra (wavelength $\lambda = 250$ - 2600 nm) of the $Bi_xGd_{3-x}Fe_5O_{12}$ samples annealed at 620, 650 and 700 °C, with the Bi content $x = 0$, 1, 2 and 2.5 on glass substrates. The incident direction of the light was normal to the sample. In order to estimate the thickness of the $Bi_xGd_{3-x}Fe_5O_{12}$ films, we fitted the measured optical reflectivity spectra to reproduce the experimental results by the calculated reflectivity spectra. We calculated the reflectivity spectra by considering the multiple reflection inside the $Bi_xGd_{3-x}Fe_5O_{12}$ films by interfaces between air / film (af) and film / glass substrate (fs). We assumed that the film thickness is uniform and the glass substrate is non-absorbing and incoherent material. The reflectivity R is calculated by the following formula (1) [21,22].

$$R = R_{afs} + \frac{R_{sa}(T_{afs})^2}{1 - R_{sa}R_{sfa}} \tag{1}$$

where R_{afs}, is the reflectivity within the interface between air (a), film (f), and the interface between film (f) and substrate (s), R_{sfa} is the reflectivity within the interface between substrate (s), film (f), and the interface between film (f) and air (a), and T_{afs} is the transmission within the interface between air (a), film (f), and the interface between film (f) and substrate (s). R_{afs}, R_{sfa} and T_{afs} include the effect of multiple reflections inside the film and can be expressed by the following formulas (2), (3) and (4). They are related to the film thickness d, wavelength λ, and refractive index $n \cdot \mathrm{i}k$ of the film. Since the refractive index has wavelength dependence, we divided the optical reflectivity spectra to two regions ($\lambda < 1000$ nm and $\lambda > 1000$ nm), and changed the refractive index and thickness to reproduce the experimentally obtained optical transmission spectra[23]. In the final stage of the fitting, the films thickness d is obtained.

$$R_{afs} = \frac{R_{af} - (2R_{af}R_{fs} - R_{fs})e^{-\frac{4\pi}{\lambda}(n-ik)d}}{1 - R_{af}R_{fs}e^{-\frac{4\pi}{\lambda}(n-ik)d}} \tag{2}$$

$$T_{afs} = \frac{(1 - R_{af})(1 - R_{fs})e^{-\frac{2\pi}{\lambda}(n-ik)d}}{1 - R_{af}R_{fs}e^{-\frac{4\pi}{\lambda}(n-ik)d}} \tag{3}$$

$$R_{sfa} = \frac{R_{fs} - (2R_{af}R_{fs} - R_{af})e^{-\frac{4\pi}{\lambda}(n-ik)d}}{1 - R_{af}R_{fs}e^{-\frac{4\pi}{\lambda}(n-ik)d}} \tag{4}$$

The simulated reflectivity spectra showed by the dotted lines in figure 1. The thicknesses were estimated to 170 - 210 nm for the samples with $x = 1$, 200 - 260 nm for the samples with $x = 2$, and 330 - 360 nm for the samples with $x = 2.5$. The viscosity of the solution was increased with increasing the Bi content x. Therefore the film thickness increased with increasing the Bi content x.

Figure 2 shows the XRD spectra of the fabricated samples on glass substrates. The XRD spectra of samples shows some peaks associated with (420) plane of $Bi_xGd_{3-x}Fe_5O_{12}$, (104) plane of Fe_2O_3, (112) plane of Gd_2O_3, (008) plane of ε-Bi_2O_3, (200) plane of BiO_3, (222) plane of β-Fe_2O_3, and (130) plane of ε-Fe_2O_3 phases.
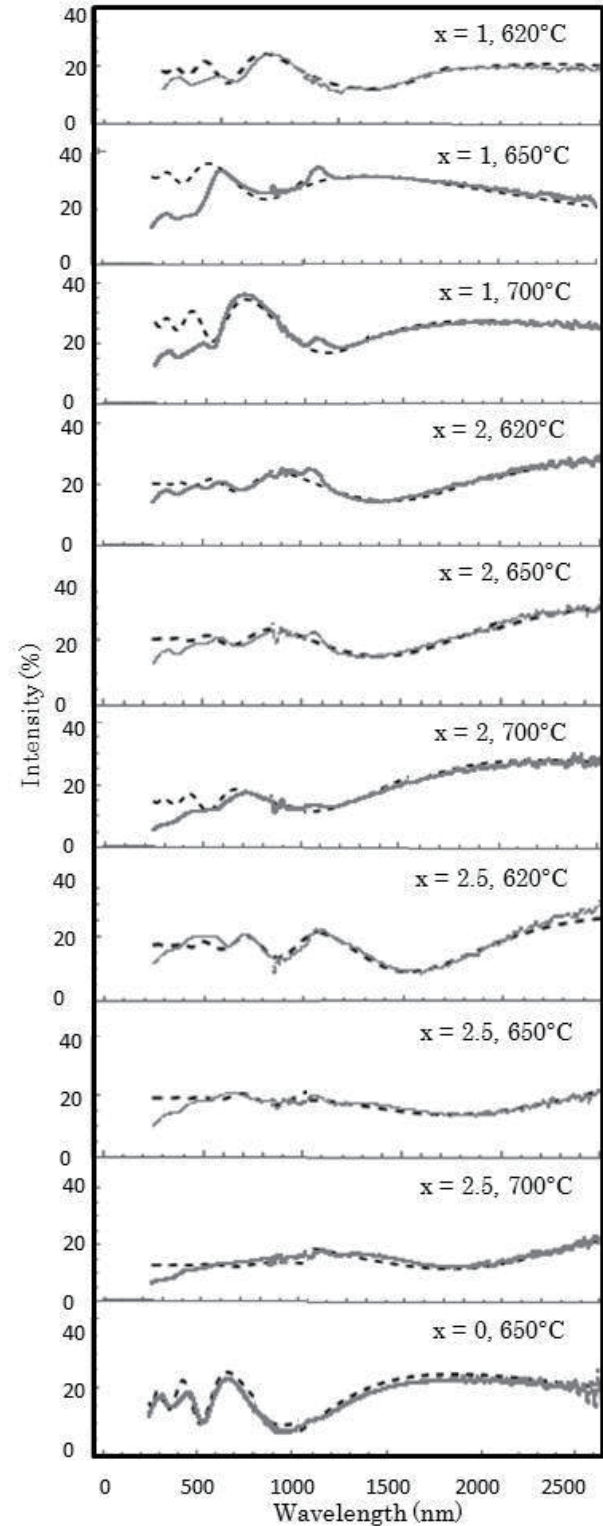
Fig. 1 Optical reflectivity spectra (solid lines) of the $Bi_xGd_{3-x}Fe_5O_{12}$ samples annealed at 620, 650 and 700 °C, with bismuth content $x = 0$, 1, 2 and 2.5 on glass substrates. The fitted spectra are shown by dashed lines.
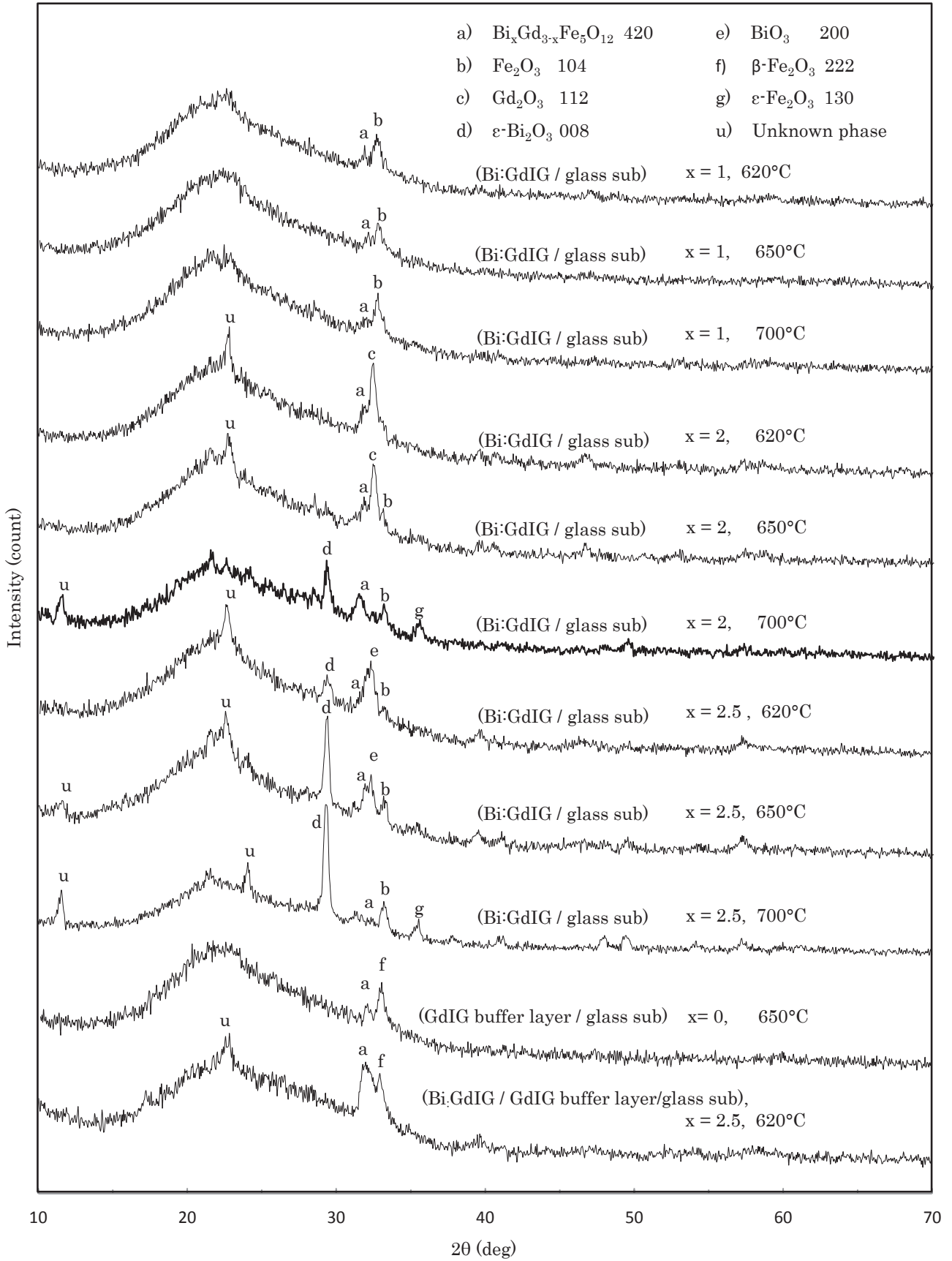
Fig. 2 X-ray diffraction spectra of the $Bi_xGd_{3-x}Fe_5O_{12}$ thin films on glass substrates at annealing temperature of 620, 650 and 700 °C with Bismuth doped $x = 0$, 1, 2 and 2.5 on glass substrates and $Bi_{2.5}$:GdIG on GdIG buffer layer/glass substrate.
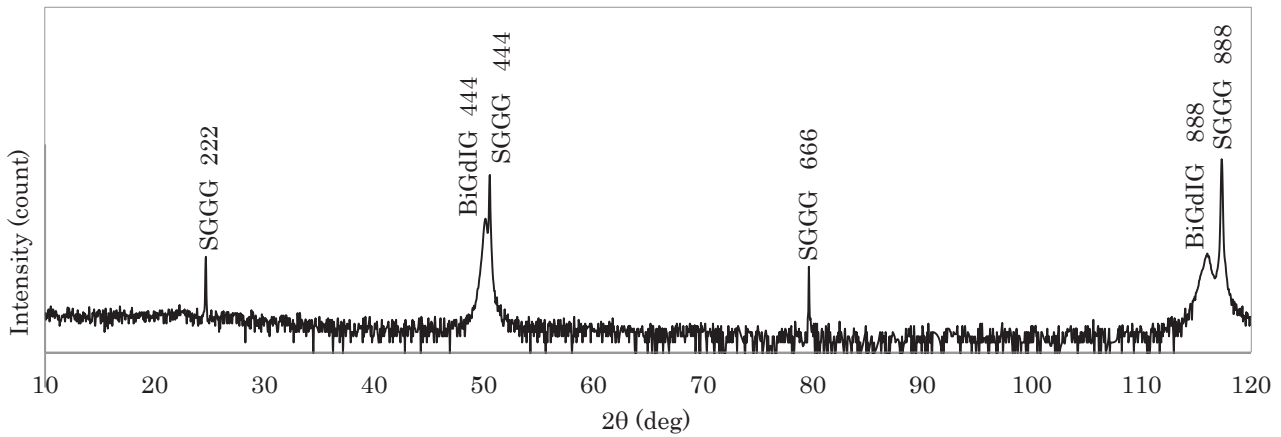
Fig. 3 X-ray diffraction spectra of the $Bi_{2.5}Gd_{0.5}Fe_5O_{12}$ thin film on SGGG (111) single crystal substrate at the annealing temperature of 620°C.　Please note that the vertical axis is in logarithmic scale.
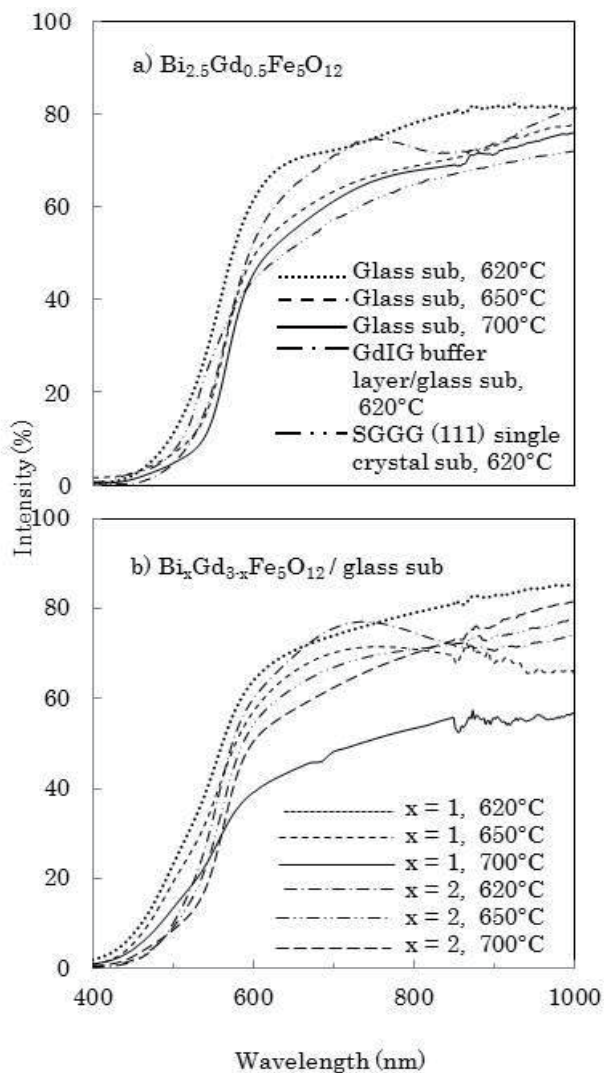
Fig. 4 Optical transmittance spectra of the Bi:GdIG samples annealed at 620, 650 and 700 °C, with the bismuth content of a) $x = 2.5$ on glass, GdIG buffer layer / glass and SGGG (111) single crystal substrates, b) $x = 1$ and 2 on glass substrates.

When the Bi_2O_3, Gd_2O_3 and Fe_2O_3 carboxylates are mixed with a ratio of $1 : 2 : 5$, and the annealing temperature of $620 - 700$ °C directly prepared on the glass substrates, the diffraction signal from Fe_2O_3 is larger than that from $Bi_xGd_{3-x}Fe_5O_{12}$. When the Bi_2O_3, Gd_2O_3 and Fe_2O_3 carboxylates are mixed with a ratio of $2 : 1 : 5$ and the annealing temperature of $620 - 650$ °C directly prepared on the glass substrates, the diffraction signal from Gd_2O_3 is larger than that from $Bi_xGd_{3-x}Fe_5O_{12}$. When the annealing temperature is 700 °C, the diffraction signal from Bi_2O_3 is increased. When the Bi_2O_3, Gd_2O_3 and Fe_2O_3 carboxylates are mixed with a ratio of $2.5 : 0.5 : 5$ and the annealing temperature of $620 - 700$ °C directly prepared on glass substrates, the diffraction signals from Bi_2O_3 and ε-Bi_2O_3 are much more dominant than that from $Bi_xGd_{3-x}Fe_5O_{12}$. The diffraction peak associated with $Bi_xGd_{3-x}Fe_5O_{12}$ were the weakest with $x = 2.5$ among all the samples without the $Gd_3Fe_5O_{12}$ buffer layer. With increasing the final annealing temperature, the diffraction peak associated with ε-Bi_2O_3 increased.　From the XRD spectra of the samples, it is difficult to fabricate Bi:GdIG thin films with high Bi content $x = 2.5$ directly on glass substrate. In order to solve this problem, we fabricated a gadolinium iron garnet (GdIG) thin film with composition of $(Gd_2O_3:Fe_2O_3 = 3:5)$ as a buffer layer for preparation of $Bi_xGd_{3-x}Fe_5O_{12}$ thin films with higher Bi content x of 2.5, with the thickness of 150 nm on the glass substrate at final annealing temperature of 650°C by the EMOD method.　When the Gd_2O_3 and Fe_2O_3 carboxylates are mixed with a ratio of $3 : 5$, the diffraction signals from $Gd_3Fe_5O_{12}$, and β-Fe_2O_3 are dominant.
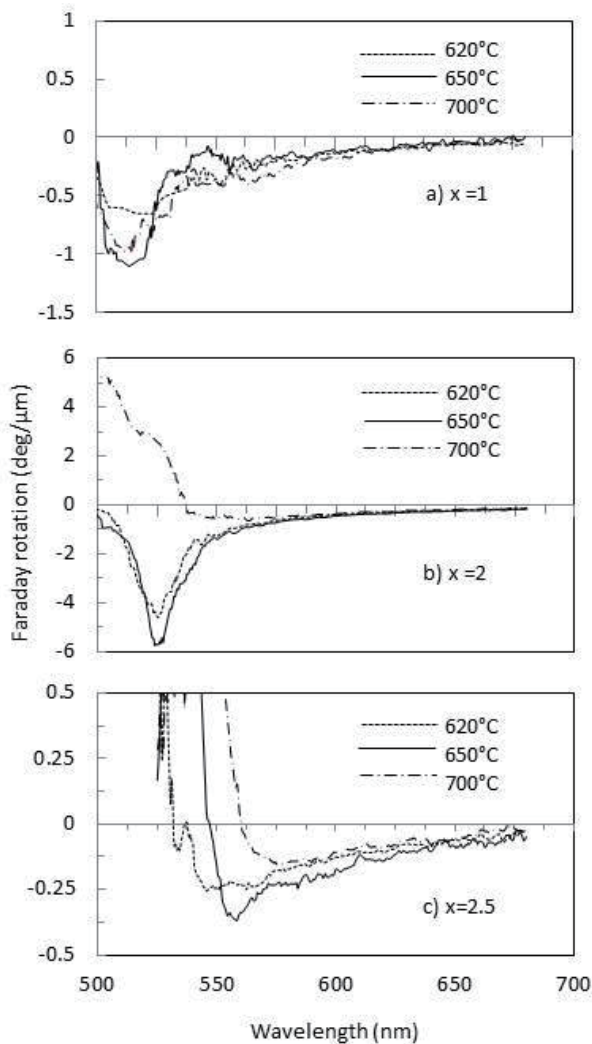
Fig. 5 Faraday rotation spectra of the $Bi_xGd_{3-x}Fe_5O_{12}$ samples with different annealing temperatures and bismuth content(a) $x = 1$, (b) $x = 2$ and (c) $x = 2.5$.

Then we tried to fabricate a $Bi_{2.5}Gd_{0.5}Fe_5O_{12}$ thin film on the GdIG buffer layer / glass substrate. The final annealing temperature for $Bi_{2.5}Gd_{0.5}Fe_5O_{12}$ thin film was set at 620°C instead of the annealing temperature of 650°C shown in figure 2. This is because when the final annealing temperature of the $Bi_{2.5}Gd_{0.5}Fe_5O_{12}$ film is the same or higher than the final annealing temperature for the GdIG buffer layer/glass sub., the part of crystal structure of the GdIG buffer layer can be destroyed[25]. Therefore, we set the final annealing temperature at 620°C for the $Bi_{2.5}Gd_{0.5}Fe_5O_{12}$ film on the GdIG buffer layer/glass sub.

When the Bi_2O_3, Gd_2O_3 and Fe_2O_3 carboxylates are mixed with a ratio of 2.5 : 0.5 : 5 and the annealing temperature of 620 °C with the $Gd_3Fe_5O_{12}$ buffer layer on glass substrate, the diffraction signal from $Bi_xGd_{3-x}Fe_5O_{12}$ is the most dominant and the formation of other
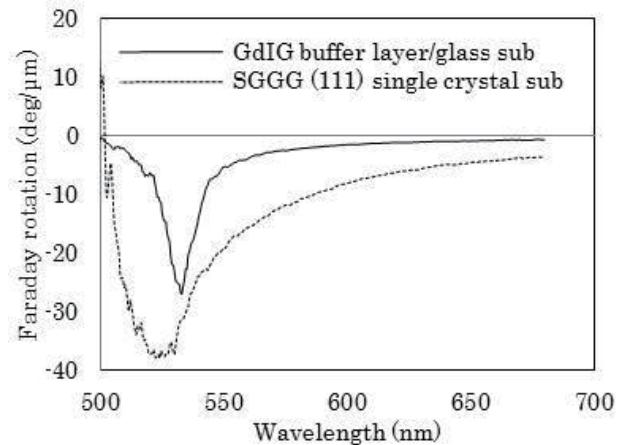
Fig. 6 Faraday rotation spectra of the $Bi_{2.5}Gd_{0.5}Fe_5O_{12}$ samples annealed at 620°C with the bismuth content $x = 2.5$ on gadolinium iron garnet buffer layer / glass sub and SGGG (111) single crystal substrates.

phases such as ε-Bi_2O_3, BiO_3 and Gd_2O_3 are suppressed. The diffraction peak associated with β-Fe_2O_3 at the right side of the Bi:GdIG diffraction peak is associated with the $Gd_3Fe_5O_{12}$ buffer layer. From figure 2, it was confirmed that the $Bi_{2.5}Gd_{0.5}$-Fe_5O_{12} thin film having garnet crystal structure was prepared with the buffer layer on glass substrate by the EMOD method.

Figure 3 shows the XRD spectra of $Bi_{2.5}Gd_{0.5}Fe_5O_{12}$ prepared by the EMOD method on (111) SGGG single crystal substrate. 444 and 888 diffraction peaks are clearly observed and other peaks associated with polycrystalline or impurity phases were not observed. The lattice constant a was calculated to 1.2587 nm. It was reported that the lattice constant of $Bi_{2.5}Gd_{0.5}Fe_5O_{12}$ samples prepared by liquid phase epitaxy (LPE) was 1.259 nm[24], and comparable to that of our $Bi_{2.5}Gd_{0.5}Fe_5O_{12}$ thins films on (111) SGGG substrate. By comparing the lattice constant of two materials and the results of figure 3, we estimated the composition of our single crystal film to $Bi_{2.5}Gd_{0.5}Fe_5O_{12}$ by the EMOD method. Also the diffraction peaks associated with Bi_2O_3, Gd_2O_3, Fe_2O_3, GdIG and BiGdIG of the polycrystalline samples on the glass substrates were confirmed by comparing the lattice spacing d measured by the XRD to the powder diffraction files of international center for diffraction data (ICDD). Therefore, we estimated the fabricated crystal structure by the EMOD method to the garnet structure.

Figure 4 shows the optical transmittance spectra of the $Bi_xGd_{3-x}Fe_5O_{12}$ thin films on the glass substrates with / without $Gd_3Fe_5O_{12}$ buffer layer and on (111)

SGGG single crystal substrate. The $Bi_{2.5}Gd_{0.5}Fe_5O_{12}$ on the $Gd_3Fe_5O_{12}$ buffer / glass sub has high transparency in visible and near infrared region, higher than the $Bi_{2.5}Gd_{0.5}Fe_5O_{12}$ film on (111) SGGG substrate.

Figure 5 shows the FR spectra of the fabricated $Bi_xGd_{3-x}Fe_5O_{12}$ thin films crystallized at 620, 650, and 700 °C with x = 1, 2 and 2.5 on glass substrates. The magnetic field of 1 T was applied perpendicular to the samples in order to fully magnetize the samples.

The samples with the annealing temperature of 650°C show larger FR (negative) than the other samples with x = 1, 2, and 2.5 annealed at 620 and 700 °C. Therefore the annealing temperature of 650°C is the optimum condition for crystallization of the BiGdIG thin films on the glass substrate by the EMOD method. The FR of Bi:GdIG increased with increasing x to 2, and decreased in the sample with high Bi content of x = 2.5.

Figure 6 shows the FR spectra of the $Bi_{2.5}Gd_{0.5}Fe_5O_{12}$ thin films on the GdIG buffer layer / glass substrate and SGGG (111) single crystal substrate. $Bi_{2.5}Gd_{0.5}Fe_5O_{12}$ thin film on the GdIG buffer layer / glass substrate showed 27.5 deg./μm at the wavelength of 533 nm, which is 8 times larger than that without the GdIG buffer layer. This is because the sample with the GdIG buffer layer showed the largest diffraction signal from the $Bi_xGd_{3-x}Fe_5O_{12}$ and garnet structure, and the samples without garnet structure including other phases such as Bi_2O_3 and Gd_2O_3 showing little FR, as shown in figure 2.

Maximum FR (negative) angle of the $Bi_{2.5}Gd_{0.5}Fe_5O_{12}$ thin films on SGGG substrate is 32.5 deg./μm at the wavelength of 533 nm. The maximum FR of the $Bi_{2.5}Gd_{0.5}Fe_5O_{12}$ thin films on the GdIG buffer layer / glass substrate is comparable with that on (111) SGGG single crystal substrate. The FR of $Bi_{2.5}Gd_{0.5}Fe_5O_{12}$ thin films on the $Gd_3Fe_5O_{12}$ buffer layer / on glass substrate (27.5 deg./μm at λ = 533 nm) is 3 time larger than that of the reported $Bi_{1.4}Gd_{1.6}Fe_5O_{12}$ sample (9.3 deg./μm at λ = 520 nm.), which was fabricated by sintering, hot press and annealing method[26]. Also it was reported that $Bi_{2.5}Gd_{0.5}Fe_5O_{12}$ films on $Nd_2Bi_1Fe_4Ga_1O_{12}$ buffer layers on a glass substrate which was fabricated by the MOD method had FR of 13.8 deg./μm at λ = 520 nm, which is half of the FR of our $Bi_{2.5}Gd_{0.5}Fe_5O_{12}$ thin films on the $Gd_3Fe_5O_{12}$ buffer layer / on glass substrate [18]. Therefore, our samples fabricated by the EMOD method showed 2 - 3 times larger FR compared with that of previously reported $Bi_xGd_{3-x}Fe_5O_{12}$ samples.

4. Conclusion

We have prepared $Bi_xGd_{3-x}Fe_5O_{12}$ thin films on glass substrates, with and without $Gd_3Fe_5O_{12}$ buffer layer prepared on glass substrates and (111) SGGG single crystal substrate by the EMOD method. We characterized the XRD, FR and optical transmittance spectra of the samples. The FR shows that the annealing temperature of 650 °C is the optimum condition for crystallization of $Bi_xGd_{3-x}Fe_5O_{12}$ on the glass substrate. From the XRD spectra, the $Bi_{2.5}Gd_{0.5}Fe_5O_{12}$ samples on the $Gd_3Fe_5O_{12}$ buffer layer shows that the Bi:GdIG thin films were successfully fabricated on the glass substrates without forming Bi_2O_3 and Gd_2O_3 phases, which are observed in samples without $Gd_3Fe_5O_{12}$ buffer layer. Furthermore, larger Faraday rotation (27.9 deg./μm at λ = 533 nm) was obtained on the sample with the $Gd_3Fe_5O_{12}$ buffer layer than that without $Gd_3Fe_5O_{12}$ buffer layer, and the Faraday rotation is comparable with that prepared on SGGG (111) single crystal substrate. It is important to suppress the formation of the Bi_2O_3 and Gd_2O_3 phases by the $Gd_3Fe_5O_{12}$ buffer layer in order to prepare $Bi_xGd_{3-x}Fe_5O_{12}$ thin films having higher Bi content x and FR, from the XRD spectra and measurement of the Faraday rotation. These findings are important to realize $Bi_xGd_{3-x}Fe_5O_{12}$ thin films having large Faraday rotation for future applications to MOSLMs and optical isolators on the glass substrates.

References

1) P. Hansen, H. Heitmann, and K. Witter: *Phys. Rev. B.,* **23**, 6085 (1981).
2) L. Halagačka, K. Postava, M. Vanwolleghem, F. Vaurette, J. Ben Youssef, B. Dagens, and J. Pištora: *J. Opt. Soc. Am. A.,* **4**, 1903 (2014).
3) H. Ishikawa, K. Nakajima, K. Machida and A. Tanii: *Opt Quantum Electron.,* **22**, 517 (1990).
4) W. Smigaj, L. Magdenko, L. Magdenko, J. Romero, S. Guenneau, B. Dagens, B. Gralak and M. Vanwolleghem: *Phot. Nano. Fund. Appl.,* **10**, 83 (2012).
5) W. Smigaj, J. Romero, B. Gralak, L. Magdenk, B. Dagens and M. Vanwolleghem: *Opt. Lett.,* **35**, 568 (2010).
6) H. Kato, T. Matsushita, A. Takayama, M. Egawa, H. Uchida, K. Nishimaura, and M. Inoue: *Trans. Magn. Soc. Jpn.,* **4**, 289 (2004).
7) H. Takagi, J. Kim, K. H. Chung, S. Mito, H. Umezawa, and

M. Inoue: *J. Magn. Soc. Jpn.,* **33**, 525 (2009).

8) S. Mito, K. Takahashi, F. Kawanishi, K. H. Chung, H. Takagi, J. Kim, P. B. Lim, and M. Inoue: *J. Magn. Soc. Jpn.,* **32**, 63 (2008).

9) K. H. Chung, J. Heo, K. Takahashi, S. Mito, H. Takagi, J. Kim, P.B.Lim and M.Inoue: *J. Magn. Soc. Jpn.*, **32**, 114 (2008).

10) M. Suzuki, T. Kotani, N. Yamaguchi, T. Miura, M. Yamaoka, M. kobayashi, and A. Misu: *J. Electron. Spectrosc. Relat. Phenom.*, **78**, 291 (1996).

11) W. Eppler, and M. H. Kryder: *IEEE Trans. Magn.,* **25**, 3743 (1989).

12) M. Laulajainen, P. Paturi, J. Raittila, H. Huhtinen, A.B. Abrahamsen, N.H. Andersen and R. Laiho: *J. Magn. Magn. Mater.,* **279**, 218 (2004).

13) J. M. Robertson, S. Wittekoek, Th. J. A. Popma, and P. F. Bongers: *Appl. Phys.,* **2**, 219 (1973).

14) Y. H. Kim, J. S. Kim and S. I. Kim: *J. Korean Phys. Soc.,* **43**, 400 (2003).

15) T. Ishibashi, A. Mizusawa, N. Togashi, T. Mogi, M. Houchido and K. Sato: *J. Cryst. Growth.,* **275**, 2427 (2005).

16) T. Kosaka, M. Naganuma, M. Aoyagi, T. Kobayasi, S. Niratisairak, T. Nomura, and T. Ishibashi: *J. Magn. Soc. Jpn.,* **35**, 194 (2011).

17) T. Ishibashi, A. Mizusawa, N. Togashi, T. Mogi, M. Houchico, and K. Sato: *J. Cryst. Growth.,* **275**, 2427 (2005).

18) T. Ishibashi, T. Yoshida, S. Ikehara and T. Nishi: *J. Appl. Phys.*, **113**, 17A926 (2013).

19) D. A. Wahid, T. Hattori, J. Sato, and H. Shimizu: *J. Magn. Soc. Jpn.,* **39**, 100-106, (2015).

20) http://www.kojundo.co.jp/English/Guide/material/csd.html

21) D. Pekker, and L. Pekker: *Thin Solid Films.*, **425**, 203 (2003).

22) M. M. Gader: *Euro. Intl. J. Sci. Technol.,* **2,** 214 (2013).

23) R. Kitamura, L. Pilon, and M. Jonasz: *Appl. Opt.*, **46**, 8118 (2007).

24) P. Hansen, K. Witter, and W. Tolksdorf: *Phys. Rev.,* **27**, 4375 (1983).

25) M. Hosoda, J. Sato, D. A. Wahid, H. Shimizu: Proc. the 63rd. spring meeting of Japan Society of Applied Physics., 20a-S621-2, Tokyo, (2016).

26) H. Takeuchi: *Jpn. J. Appl. Phys.*, **14**, 1903 (1975).

<Paper>

Demagnetization Analysis of Ferrite Magnet Using Two-line Approximation Based on Reluctance Network Analysis

D. Momma, Y. Yoshida*, and K. Tajima

Department of Cooperative Major in Life Cycle Design Engineering, Akita Univ., *1-1, Tegata Gakuen-machi, Akita 010–5802, Japan*
*Department of Electrical and Electronic Engineering, Akita Univ., *1-1, Tegata Gakuen-machi, Akita 010–5802, Japan*

This study presents a method for determining the demagnetization characteristics of ferrite magnets based on reluctance network analysis (RNA). First, an RNA model for determining the operating points of a magnet considering demagnetization using a two-straight-line approximation of the demagnetization curve is discussed. Then, using the proposed model, demagnetization characteristics are determined. Experimental results demonstrate the validity of the proposed method.

Key words: reluctance network analysis, ferrite magnet, demagnetization analysis, two line approximation

1. Introduction

Permanent magnet (PM) motors based on powerful rare-earth magnets are widely used in various applications because of their high-performance characteristics. However, rare-earth magnets may be subject to price rises as the production of such metals is concentrated in a single country. Therefore, the development of highly PM motors without rare-earth magnets is required.

Although the maximum magnetic energy product of ferrite magnets is one tenth that of rare-earth magnets [1], high-efficiency ferrite magnet motors have been reported [2]. Ferrite magnets in motors are exposed to a large reverse magnetic field to obtain performance equivalent to that of rare-earth magnet motors. Therefore, ferrite magnets are at a risk of demagnetization because of their low coercive force. Thus, it is necessary to consider the demagnetization of ferrite magnets for ferrite magnet motor design.

Reluctance network analysis (RNA) is a useful method to save calculation time in the estimation of the characteristics of PM motors, as reported in previous studies [3]-[6]. However, a demagnetization analysis method using RNA has not yet been proposed.

Because demagnetization analysis using finite element analysis (FEA) has been previously discussed [7]-[8], this method is now applied to RNA. This study presents an RNA model for determining the operating points of ferrite magnets; this model uses a two-line approximation of the demagnetization curve. To verify the accuracy of the proposed model, the calculated results are compared to values obtained from two-dimensional (2D) FEA and experimental results.

2. Derivation of the RNA Model

Fig. 1 shows the shape and specifications of analytical and experimental objects under consideration. Exciting coils are wound around U-shaped cores. Ferrite magnets with a thickness of 2 or 3 mm are sandwiched between the cores. The number of winding turns of exciting coils per leg is 80, and the stack length of the cores and ferrite magnets is 20 mm.

Fig. 2 illustrates the division of a 2D RNA model. The RNA model is derived in a quarter region of the analysis model shown in the figure, taking advantage of the analytical model's symmetry. In the model, the elements around the air gap are divided with a size of 1.0 mm × 1.0 mm. When the 3-mm-thick magnet is used, the element size of the magnet in the y-axis direction is 1.5 mm.

Each divided element is expressed in a 2D-unit magnetic circuit. Fig. 3(a) shows the unit magnetic circuit of the core and air region. In the figure, *l* is the length of the element. The reluctance, R_m, in the unit magnetic circuit is obtained from

$$R_m = \frac{l}{2\mu_s\mu_0(l \times l_s)}, \qquad (1)$$

where μ_s is the relative permeability, μ_0 is the permeability of vacuum, and l_s is the stack length of the model. The elements of a ferrite magnet can be expressed as the reluctance and magnetomotive force (MMF), F_m, shown in Fig. 3(b). The reluctance of a ferrite magnet,
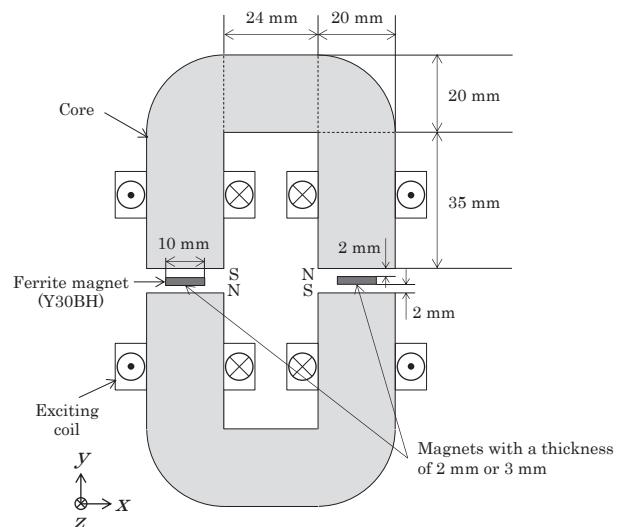

Fig. 1 Specifications of analytical and experimental objects.

R_{mag}, is expressed by

$$R_{mag} = \frac{l}{2\mu_r\mu_0(l \times l_s)},\qquad(2)$$

where μ_r is the magnet's recoil. By connecting all unit magnetic circuits together, the RNA model is obtained.

Fig. 4 illustrates the demagnetization curve of a ferrite magnet, which is approximated by two lines. In the figure, B_r, B_r', H_c, and H_c' are the residual magnetic flux density before demagnetization, residual magnetic flux density after demagnetization, coercive force before demagnetization, and coercive force after demagnetization, respectively. If there is no demagnetization in a ferrite magnet element, F_m is given by

$$F_m = \frac{B_r l}{2\mu_r\mu_0}.\qquad(3)$$

When an operating point of a ferrite magnet is changed by an external magnetic field and becomes less than the knee point, the MMF after demagnetization, F_m', can be expressed as

$$F_m' = \frac{B_r'l}{2\mu_r\mu_0}.\qquad(4)$$

To obtain the residual magnetic flux density after demagnetization (B_r'), B–H and J–H characteristics, where $J = B - \mu_0 H$ as shown in Fig. 5, are used [9]. First, the operating point without considering an external magnetic field, plotted as point a in the figure, is determined by the derived RNA model. The magnetic field at this time is diamagnetic, H_d. At the same time, point b, where a perpendicular line from point a intersects with J–H characteristics, is determined Then, line l_0 is given as a straight line passing through point b and the origin. Next, the operating point considering an external magnetic field, plotted as point c in the figure, is determined. The external magnetic field, H_{ex}, is calculated as the difference between the magnetic field at point c and H_d. The line, l_0, is shifted toward the negative direction by H_{ex} without changing the slope to obtain line l_1. The intersection of J–H characteristics and line l_1 is plotted as point d. When point d is less than the knee point of J–H characteristics, irreversible demagnetization occurs. B_r' is determined as the point where the vertical axis intersects the straight line, which passes through point d and is parallel to J–H characteristics before demagnetization.

3. Demagnetization Analysis of the Ferrite Magnets

Using the proposed RNA model, the demagnetization of the ferrite magnets is determined with an exciting current that produces an external magnetic field opposed to the magnetization direction. Three cycles of a sawtooth wave, shown in Fig. 6, are applied to exciting coils. The maximum value of the current is 4.0 A when the magnet thickness is 2 mm, and 5.5 A when the thickness is 3 mm.

Fig. 7 illustrates the direction of the magnetic flux flowing through the core. This direction is caused by the
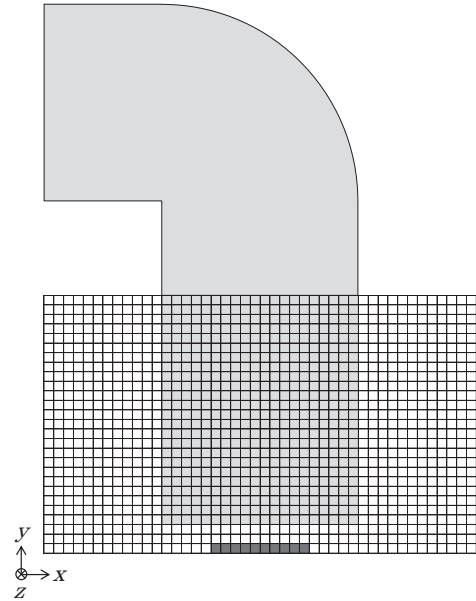
Fig. 2 Division of the RNA model.
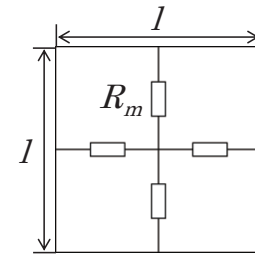
(a) Core and air
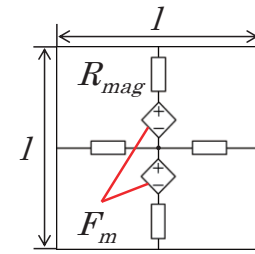
(b) Magnet
Fig. 3 Unit magnetic circuit.

$B = \mu_r\mu_0 H + B_r$
$= 1.40 \times 10^{-6} H + 0.385$

Knee point

Parallel lines

H_c H_c' H_{cb}

$B = 0.6 \times 10^{-4} H + 13.7$

B_r
B_r'
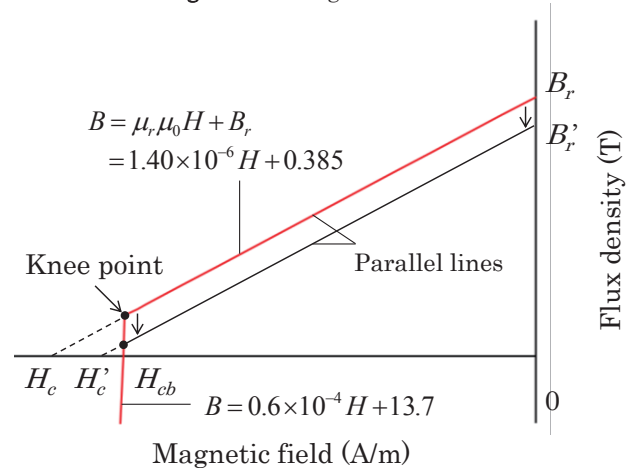
Flux density (T)

Magnetic field (A/m)

Fig. 4 Demagnetization curve approximated by two lines.
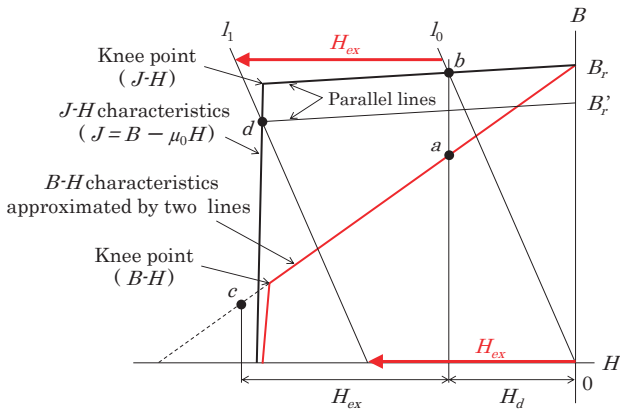
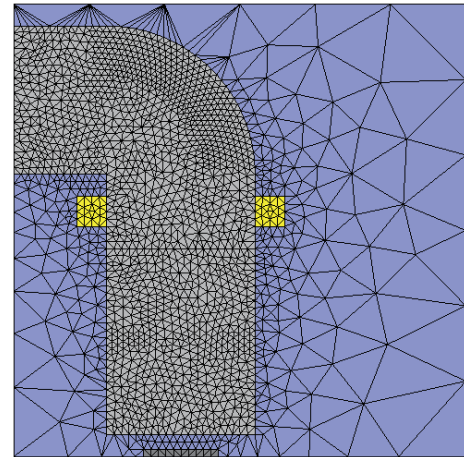**Fig. 5** Calculation method for the residual magnetic flux density after demagnetization.
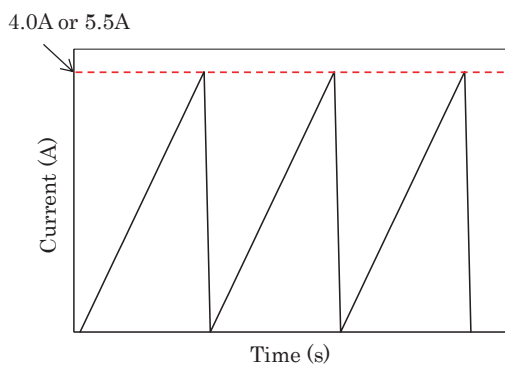

Fig. 6 Waveform of exciting current.
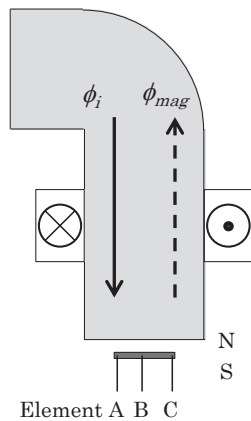
Fig. 7 Direction of magnetic flux and detection points.

Fig. 8 Mesh distribution of the 2D-FEA model.

(a) Graph for the 2-mm-thick magnet.

(b) Graph for the 3-mm-thick magnet.
Fig. 9 Calculated operating points of element B.

winding current and is the inverse of the flux of the ferrite magnet. In the figure, elements A, B, and C are the detection points of demagnetization.

To compare the results from the RNA model with those obtained using FEA, the same calculation as that of RNA was performed using the JMAG-Designer Ver.14.1 software. Fig. 8 shows the mesh distribution of the 2D FEA model. The number of elements of the FEA model is 3,429.

Fig. 9 shows the operating points of element B determined by the RNA and 2D FEA models. It is observed that the data obtained by the proposed RNA model almost agree with the corresponding 2D FEA

calculation results. The residual flux density of the magnet before demagnetization, B_r, is 0.385 T. The calculated residual magnetic flux density after demagnetization by RNA, B_r', is 0.283 T when the magnet thickness is 2 mm, and 0.284 T when it is 3 mm.

Table 1 shows a comparison between the demagnetization factors calculated by RNA and 2D FEA for the 2-mm-thick magnet, and Table 2 shows a comparison of the calculated demagnetization factors by RNA and 2D FEA for the 3-mm-thick magnet In the tables, the demagnetization factor, D_{fac}, is defined as

Table 1 Demagnetization factors for the 2-mm-thick magnet.

	Element		
	A [%]	B [%]	C [%]
RNA	14.9	26.6	14.9
2D-FEA	14.2	30.4	14.6

Table 2 Demagnetization factors for the 3-mm-thick magnet.

	Element		
	A [%]	B [%]	C [%]
RNA	12.7	26.3	12.7
2D-FEA	7.9	31.0	8.0

Table 3 Interlinkage magnetic flux of ferrite magnets.

	2 mm		3 mm	
	before [Wb]	after [Wb]	before [Wb]	after [Wb]
RNA	0.0236	0.0182	0.0308	0.0239
2D-FEA	0.0236	0.0173	0.0308	0.0229

follows:

$$D_{fac} = \left(1 - \frac{B_r{}'}{B_r}\right) \times 100. \quad (5)$$

Demagnetization factor at the center of the magnet is greater than that at either end. The calculated values obtained from the proposed model almost agree with those obtained from 2D FEA.

Table 3 shows a comparison of the interlinkage magnetic flux of the ferrite magnets calculated via RNA and 2D FEA. After demagnetization, the interlinkage magnetic flux decreased by approximately 25 % for both magnet thickness.

The number of time steps of the proposed model and 2D FEA model is 64 for three cycles of the sawtooth wave. The calculation times of the proposed and 2D FEA models are 17 s and 58 s, respectively.

4. Comparison with Experimental Results

To verify the calculation accuracy of the RNA model, the calculated values were compared to the measured ones. Fig. 10 shows a photograph of the experimental apparatus; Fig. 10(a) is an exposed view. The supporters are sandwiched between the cores to fix the positions of the cores and magnets. Fig. 10(b) shows an assembled experimental setup. Fig. 11(a) shows the conditions of the experiment, and Fig. 11(b) shows the detection point of the magnetic flux density of the ferrite magnet. The magnetic flux density was determined using a gauss meter (GM-301, Denshijiki Kogyo); the average values of the surface magnetic flux density were obtained from 10 measurements with magnets of the same size.

Fig. 12 shows the comparison of the magnetic flux density of the magnet surface before and after demagnetization. The DC input current is 4.0 A when the magnet thickness is 2 mm and 5.5 A when it is 3

(a) Exposed view
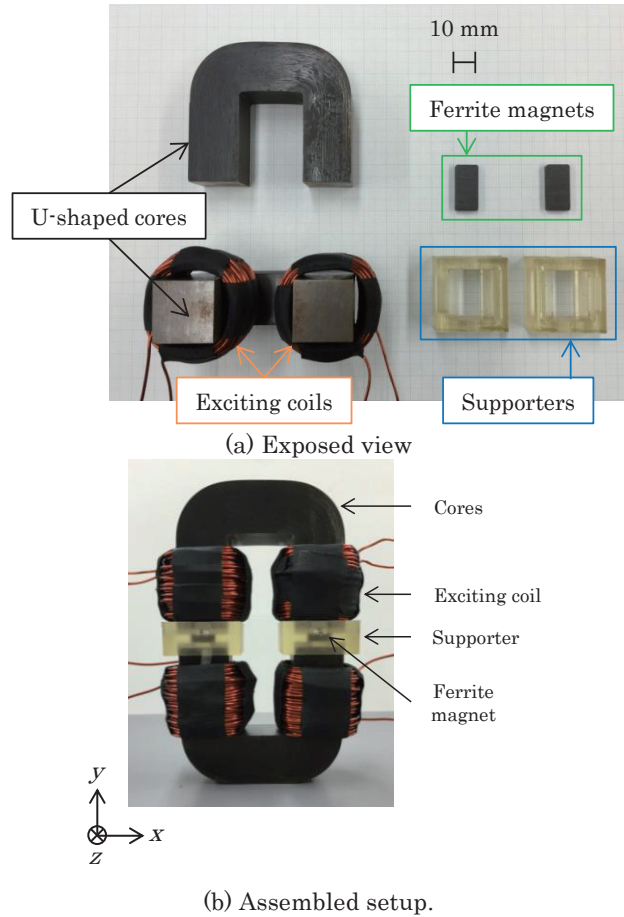
(b) Assembled setup.
Fig. 10 Photographs of the experimental apparatus.
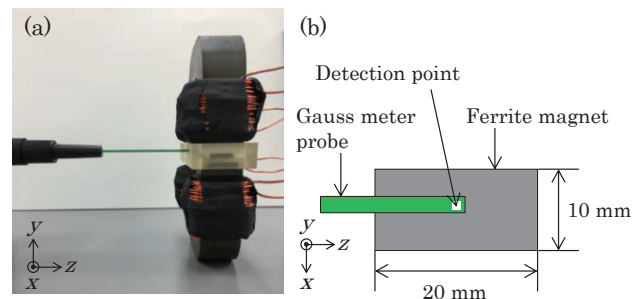
**Fig. 11** (a) Measurement setup. (b) Detection point of the magnetic flux density.

mm. In the figure, the error bars denote the maximum and minimum the measured values. It is concluded that the magnetic flux density determined by the proposed RNA model almost agrees with the corresponding 2D FEA calculated and measured values.

5. Conclusions

This study presented the demagnetization analysis of a ferrite magnet based on RNA. In the proposed model, the demagnetization curve of the magnet was approximated by two lines to estimate the magnetic flux density before and after demagnetization. The validity of the proposed RNA model has been demonstrated by comparing the calculated results with 2D FEA calculation results and experimental results.
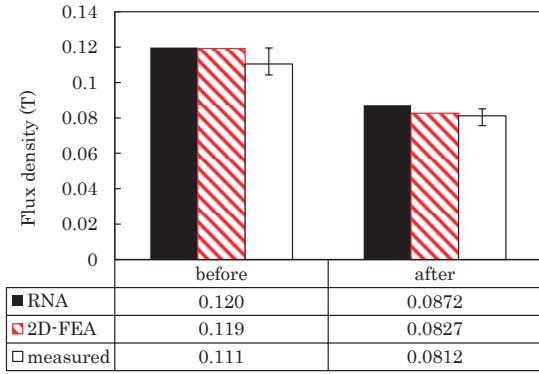
(a) Graph for the 2-mm-thick magnet.
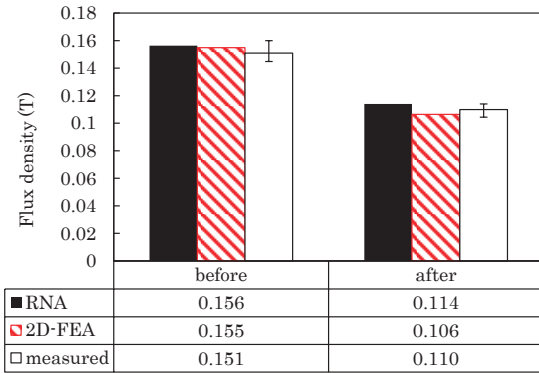
(b) Graph for the 3-mm-thick magnet.

Fig. 12 Comparison of magnetic flux densities of magnets.

References

1) M. Sagawa, M. Hamano, and M. Hirabayashi: Eikyujishaku −Zairyokagaku to Oyo− (in Japanese), p. 16 (Agune Gijutsu Center, Tokyo, 2007).
2) M. Sanada, Y. Inoue, and S. Morimoto: *IEEJ Trans. IA*, 13, 12, 1401-1407 (2011).
3) K. Nakamura, K. Saito, and O. Ichinokura: *IEEE Trans. Magn.*, 39, 3250-3252 (2003).
4) K. Nakamura, M. Ishihara, and O. Ichinokura: *17th International Conference on Electrical Machines (ICEM 2006)*, PSA1-16 (2006).
5) K. Nakamura and O. Ichinokura: *13th International Power Electronics and Motion Control Conference (EPE-PEMC 2008)*, 441 (2008).
6) Y. Yoshida, K. Nakamura, O. Ichinokura, and K. Tajima: *IEEJ Journal IA*, 3, 6, 422-427 (2014).
7) A. Yamagiwa, K. Aota, Y. Sanga, H. Takabayashi and M. Natsumeda: *IEE JAPAN*, RM-03-41 (2003) [in Japanese].
8) Y. Osawa and A. Yamagiwa: *IEEJ*, RM-13-62 (2013) [in Japanese].
9) https://www.hitachi-metals.co.jp/products/auto/el/pdf/hg-a2 -b.pdf (As of January 09, 2016) [in Japanese].

<Paper>

Improvement of induction motor analysis accuracy in reluctance network analysis

Tomoyuki Umesaka*, Katsubumi Tajima*, and Yukihiro Yoshida**

*Cooperative Major in Life Cycle Design Engineering, Graduate School of Engineering and Resource Science, Akita Univ., 1-1Tegatagakuen-machi, Akita 010–8502, *Japan*

**Department of Electrical and Electronic Engineering, Graduate School of Engineering and Resource Science, Akita Univ., 1-1Tegatagakuen-machi, Akita 010–8502, *Japan*

In previous studies, we applied reluctance network analysis (RNA) to the dynamic analysis of the induction motor. However, the accuracy of our analysis of the motor characteristics using the RNA model was not high because the detailed magnetic flux distribution in the rotor was not taken into account. In this paper, we propose a 3D RNA model that considers the detailed magnetic flux distribution in the rotor and skew of the rotor bar. Using the proposed RNA model, the winding currents of the induction motor under no-load and locked rotor conditions can be calculated with higher accuracy than with the previous RNA model.

Keywords: Induction motor, Reluctance network analysis, Analysis of dynamic characteristics, Squirrel cage rotor, Skew, High-speed calculation

1. Introduction

In Japan, the proportion of thermal power to the total amount of power used has become large since most of the nation's nuclear power plants have ceased operation. The proportion of fossil energy to total energy in Japan was about 90% as of in 2011, and most of the fossil fuels were imported. It has been pointed out that the stable supply of future power in Japan will not be easy [1] because the power consumption of the world is increasing due to population growth and economic growth in emerging countries.

Therefore, improving the efficiency of motors used in various applications is strongly required. Of particular interest are induction motors, which are used in extensive applications ranging from large industrial equipment to compact household appliances.

To improve the efficiency of such motors, a high-precision calculation method of the motor characteristics of all potential materials and dimensions is required. The finite element method (FEM) has generally been used for electromagnetic devices in the past, but for dynamic analysis of the induction motor, a great deal of computing time and memory are required. Therefore, in a previous work the authors applied reluctance network analysis (RNA) to the dynamic analysis of the induction motor [2].

In the current work, we present an analysis of the accuracy improvement of the dynamic characteristics of the induction motor based on RNA considering the detailed magnetic flux distribution and skew of the rotor.

2. Capacitor motor (single-phase induction motor)

⟨2·1⟩ Structure and principles of the capacitor motor

The basic circuit of the capacitor motor is shown in Fig. 1, where C_r is a running capacitor, C_s is a starting capacitor, v is the applied voltage, and i_m and i_a are the main winding and auxiliary winding currents, respectively.

By connecting C_r, the phase difference between the auxiliary and main winding currents is almost 90 degrees. As a result, the rotating magnetic field is generated around the squirrel cage rotor, and the motor generates a driving torque.

⟨2·2⟩ Specifications of analysis object

The test motor is a capacitor start-type capacitor run motor (SKD-DBKK8) made by Toshiba. Its specifications and dimensions are listed in Table 1. The main winding and auxiliary winding are both distributed windings. Figure 2 and Table 2 show the arrangement and number of turns, respectively [2].
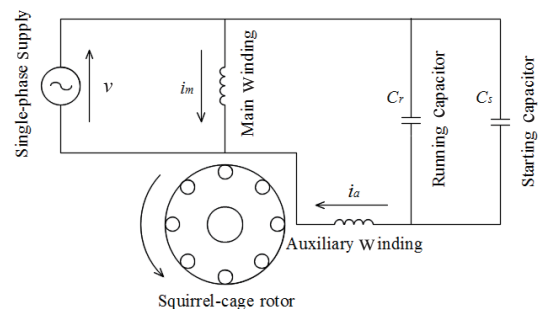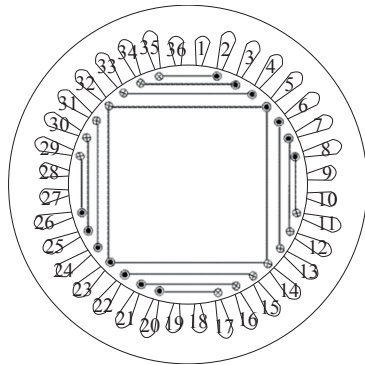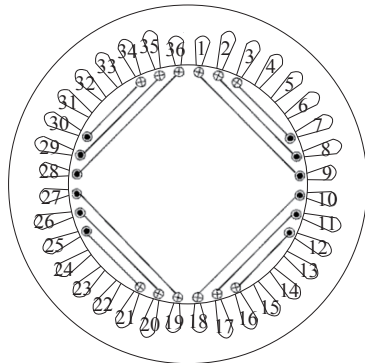

Fig. 1 Circuit configuration of a capacitor motor.

(a) Main windings

(b) Auxiliary windings

Fig. 2 Arrangement of main windings.

Table 1 Specifications of specimen motor.

Parameter	Value
Frequency	50 Hz
Voltage	100 V
Current	12.6 A
Output	750 W
Number of poles	4
Rated speed	1440 rpm
Running capacitor	40 µF
Starting capacitor	350 µF
Number of stator slots	36
Internal diameter of stator	90.0 mm
Outer diameter of stator	146.0 mm
Gap width	0.3 mm
Number of rotor slots	44
Outer diameter of rotor	89.4 mm
Iron core length	93.0 mm

Table 2 Number of turns of windings.

Main windings		Auxiliary windings	
Slot number	Turns	Slot number	Turns
35-2,11-8,17-20,29-26	7	1-9,18-10,19-27,36-28	36
34-3,12-7,18-21,30-25	11	2-8,17-11,20-26,35-29	18
33-4,13-6,15-22,31-24	14	3-7,16-12,21-25,34-30	5
32-5,14-5,14-23,32-23	7		

3. 2-dimensional RNA model of capacitor motor

⟨3·1⟩ Overview of Reluctance Network Analysis

The authors previously proposed a method of reluctance network analysis (RNA) that is suitable for dynamic simulations of an orthogonal-core type variable inductor, the SR motor and IPM motor, because of its simple modeling, high calculation accuracy, and ease of coupled analysis. Moreover, in calculation based on RNA, it is possible to use a general-purpose circuit simulation program such as SPICE.

We explain the flow of construction of the RNA model of the capacitor motor below.

⟨3·2⟩ RNA model of stator [3]

The cross section of the capacitor motor is roughly composed of a stator, a rotor, and the air gap, as shown in Fig. 3.

Because the stator has 36 slots in a circumferential direction, we divide it into 36 parts in the circumferential direction, as shown in Fig. 4. The division of each part includes the surrounding space so as to consider the linkage fluxes into multiple elements, as shown in Fig. 5. In the figure, each tooth is divided into two equal parts because the concentrated magnetomotive forces due to winding current are arranged as shown in Fig.5. The divided elements can be expressed by a unit two-dimensional magnetic circuit, as shown in Fig. 6.
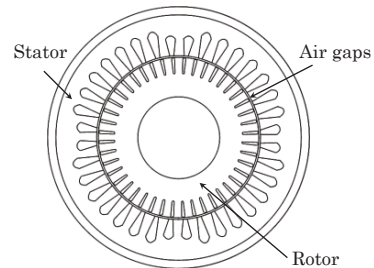
Fig. 3 Cross section of a capacitor motor.
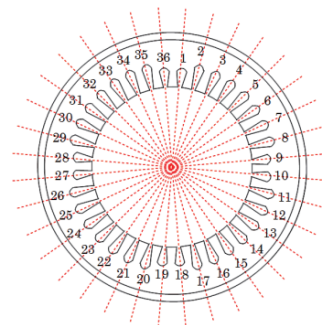
Fig. 4 Division in the radial direction of stator.
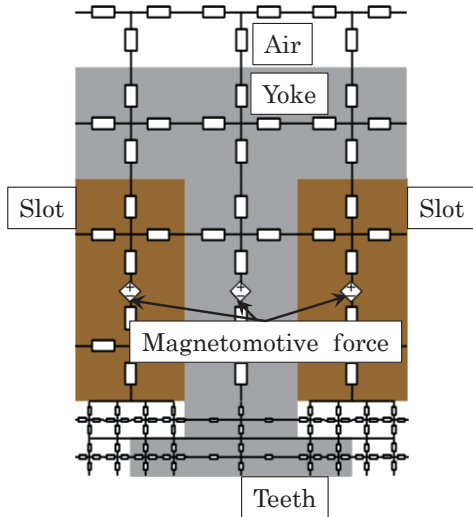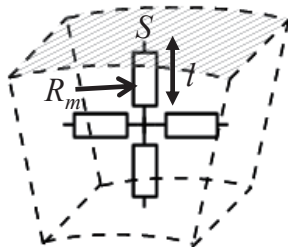
Fig. 5 RNA model of the stator (1/36).

Fig. 6 Magnetic circuit of element.

Reluctance R_m in this unit magnetic circuit can be represented by equation (1) with magnetic permeability μ, magnetic path length l [m], and sectional area S [m²]:

$$R_m = \frac{l}{\mu S} \qquad (1)$$

Magnetomotive force is proportional to the number of turns N and current i of the coil. The magnetomotive force source is placed in consideration of the distributed winding of the main and auxiliary winding between stator slots [2].

⟨3·3⟩ RNA model of the rotor [3]

The rotor of the capacitor motor used in this paper is the squirrel cage rotor. It has 44 slots in the circumferential direction, so we divide the rotor into 44 parts in the circumferential direction, as shown in Fig. 7, where each part is represented as a magnetic circuit network, as shown in Fig. 8. Therefore, by linking 44 circuits, we can derive the RNA model of the rotor.

The rotor has a chain structure consisting of end rings and conductor bars. The magnetic flux ϕ of the stator flows to the rotor and the electromotive force e is generated by Faraday's law of electromagnetic induction in the rotor to flow the eddy current i. In addition, according to the law of Lenz, eddy current i acts to prevent the change of the magnetic flux flow, and generates a magnetomotive force in the opposite direction of the magnetic flux. We obtained a chain electrical circuit composed of 44 circuits (Fig. 9), where the size of the conductor bar is $R_{bar} = 1.14 \times 10^{-4}$ Ω, the size of the end ring is $R_{end} = 4.54 \times 10^{-6}$ Ω, and the resistivity is 75℃ of aluminum.
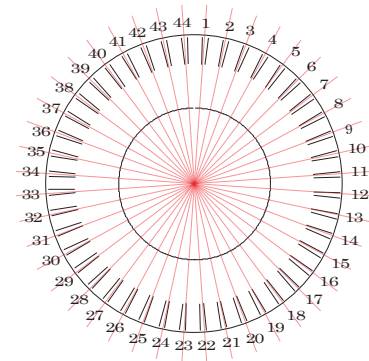
Fig. 7 Division in the radial direction of the rotor.
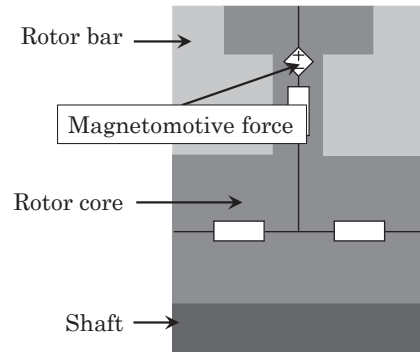
Fig. 8 RNA model of the rotor (1/44).
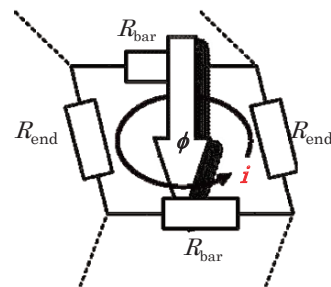
Fig. 9 Electric circuit model of the rotor.

⟨3・4⟩ Driving expression of the rotor [4]

In an earlier work [5], we proposed an RNA model of the rotor when the rotor is driving. This model consists of an electrical circuit to evaluate the induced currents on the rotor bars and end rings and a magnetic circuit to express the MMFs corresponding the induced currents on the rotor, as shown in Fig. 10. In the figure, there are eight stator slots and eight rotor slots .

The flux flowing into the first slot of the rotor ϕ_{r1} shown in Fig. 10 (a) is obtained by

$$\phi_{r1} = \frac{4}{\pi} \cdot \left\{ \left(\frac{\pi}{4} - \theta \right) \phi_{s1} + \theta \cdot \phi_{s2} \right\} \quad \left(0 \leq \theta \leq \frac{\pi}{4} \right), \qquad (3)$$

where θ is the rotating angle of the rotor. The magnetomotive force generated by the induced current in the rotor electric circuit MMF_1 shown in Fig. 10 (b) is expressed by

$$MMF_1 = \frac{4}{\pi} \cdot \left\{ \left(\frac{\pi}{4} - \theta \right) i_{r1} + \theta \cdot i_{r8} \right\} \quad \left(0 \leq \theta \leq \frac{\pi}{4} \right), \qquad (4)$$

where i_{r1} and i_{r8} are the electric currents calculated by the electric circuit model.

(a) Fluxes flowing into the rotor.

(b) MMFs acting on the stator
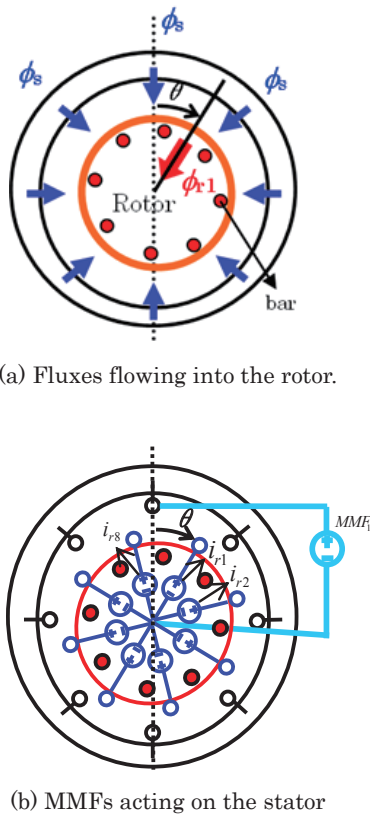
Fig. 10 Expression of coupling between the rotor and stator.

4. 3-dimensional RNA model[5]

⟨4・1⟩ New RNA model of the rotor

As described in <3.3>, the previous RNA model of the rotor in Fig. 8 is a reverse T-shaped simple magnetic circuit that did not consider the magnetic flux distribution of the core and skew of the rotor bars. To improve the analysis accuracy of the motor, we have developed a new RNA model that represents the flux distribution in the rotor and skew. We divide a part of the rotor shown in Fig. 8 into 19 elements corresponding to the shape of the conductor bar and the iron core of the rotor to make the new RNA model.

⟨4・2⟩ Driving expression of new RNA model

Here, we consider the magnetic flux ϕ_r passing through the rotor core. In the previous model (Fig. 8), all ϕ_r passed through the rotor core. In contrast, in the model proposed here (Fig. 11), ϕ_r flows in both the rotor core and the conductor bar. In other words, ϕ_r' passes through the rotor core between the conductor bars.

We calculate ϕ_r' on the rotating state as follows.

① Flux ϕ_r can be given by using Fig. 10 (a): it flows from the stator to 1/44 of the rotor model (Fig. 11).

② However, the magnetic flux ϕ_r' flowing between the conductor bars is different from ϕ_r. For this reason, we use another RNA model to calculate ϕ_r' from ϕ_r (Fig. 12).

③ To obtain a reaction field magnetomotive force i_r in the electric circuit model of the rotor using the ϕ_r, we give the original magnetic circuit MMF_1–MMF_{44} with reference to Fig. 10. (b).
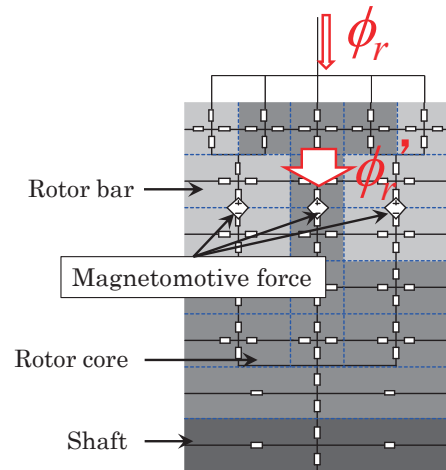

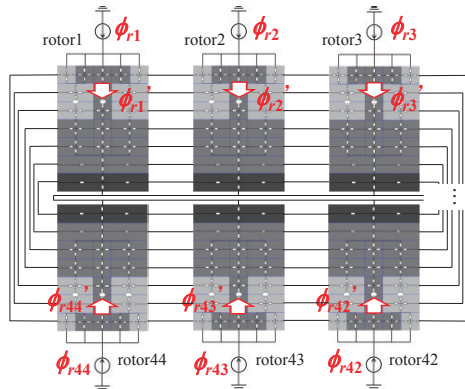**Fig. 11** New RNA model of the rotor(1/44).

Fig. 12 Calculation circuit of $\phi_{r1}'-\phi_{r44}'$ from $\phi_{r1}-\phi_{r44}$.

⟨4·3⟩ Consideration of skew

The conductor bars of the squirrel-cage rotor of the induction motor are skewed as shown in Fig. 13. Because the 2-dimensional RNA model cannot express the skew, a 3-dimensional model is needed to consider the axial direction structure. In this paper, we constructed a 3-dimensional RNA model representing the rotor structure of the axial direction to consider the skew of two slots. The rotor bar shape was approximated using a three-layer structure as shown in Fig. 14. The 3-dimensional unit magnetic circuit used is shown in Fig. 15. For the laminated structure of the rotor core, the reluctance R' in the laminated direction was calculated as a relative permeability of 25 using the methods of reference 6.
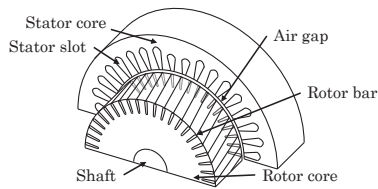
Fig. 13 Stator and rotor of capacitor motor.
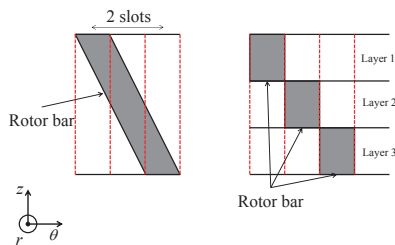
Fig. 14 Consideration of skew for the RNA model.
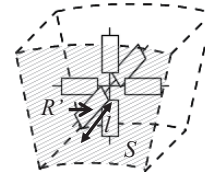
Fig. 15 3-dimensional magnetic circuit of element.

5.   Results and discussion

We examined the validity of the new RNA model of the capacitor motor by using the OrCAD PSpice 16.6 (Cadence Design Systems, Japan) as a solver for the analysis and a regular PC (Intel®Core (TM) i7-3770KCPU @ 3.5 GHz 3.5 GHz 16.0 GB RAM). Because the same flux distribution appears at every 180 degrees in the four-pole structure, we use a half model.

With the stator and rotor core material, we assume a non-oriented silicon steel sheet 50H600 (NIPPON STEEL CORPORATION) and a relative magnetic permeability of 4000. The rotor conductor bars were the same relative permeability as air because their material is non-magnetic.

In the case of applying the sinusoidal voltage of 50 Hz, the waveforms of the currents in the previous and proposed model with locked rotor and under no-load are shown in Figs. 16 and 17. As we can see, the calculation accuracy is improved. Moreover, from Fig. 17 shows that the current pulsation occurring the previous model is reduced. This pulsation is thought to stem from errors in the magnetic flux and the magnetomotive forces of the linear interpolation for use in driving expression, as described in <3.4>. However, by considering the detailed magnetic flux distribution and the skew, we are able to reduce the magnitude of the pulsation.

The effective values I_m, I_a obtained from these current waveforms are shown in Tables 3 and 4. Calculation errors of each winding current are compared with the calculation results by the previous model. Results show that they are greatly reduced. In particular, the calculation error of the main winding current of the motor with locked rotor is reduced.

Figure 18 shows the change of I_m, and I_a to slip s. As we can see in figure, there is good agreement around the synchronous speed. However, the error of the main winding current is increased with the increase of slip s.

Twenty cycles of computation took about 30 minutes with the locked rotor, and about one hour in the rotational state.
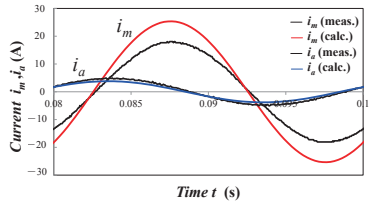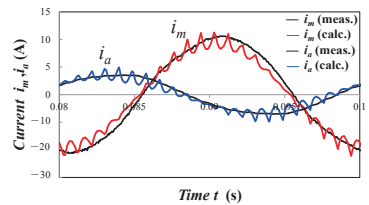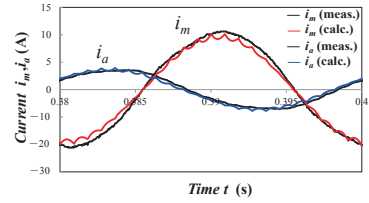
(a) Previous model
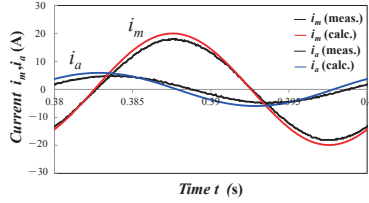
(b) Proposed model

Fig. 16 Current waveforms of the motor with locked rotor.

(a) Previous model

(b) Proposed model

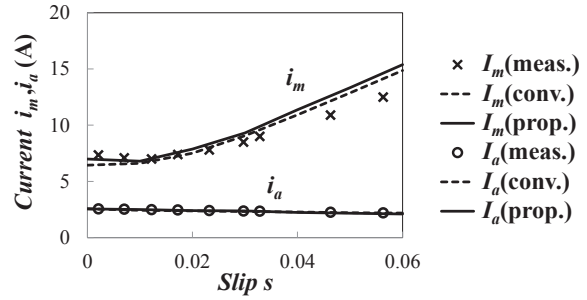**Fig. 17** Current waveforms of the motor under no-load.

Fig. 18 Load characteristics of motor.

6. Conclusions

We proposed a 3D RNA model that considers the detailed magnetic flux distribution in the rotor and skew of the rotor bar. Experimental results showed that the calculation accuracy of the winding currents under no-load and locked rotor conditions are improved compared with the previous RNA model. Also, the pulsation of winding current waveforms is reduced while maintaining high-speed calculation. This is much-needed progress in the high-precision characteristic calculation of the induction motor.

However, the calculation error of the main winding current of the motor with load became large in the low speed area. Therefore, in our future work we intend to improve the accuracy of the load characteristics of the induction motor to apply the proposed method to induction motor design.

Table 3 I_m and I_a of the motor with locked rotor.
(Input voltage 25.6[V_{rms}])

	I_m [A_{rms}]		I_a [A_{rms}]	
	previous	proposed	previous	proposed
Measurement	12.6		3.45	
Calculation	18.1	14.4	2.68	4.11
Relative error	43.7%	14.3%	22.3%	19.1%

Table 4 I_m and I_a of the motor under no-load.
(Input voltage 100[V_{rms}])

	I_m [A_{rms}]		I_a [A_{rms}]	
	previous	proposed	previous	proposed
Measurement	7.35		2.57	
Calculation	6.45	6.99	2.66	2.56
Relative error	12.2%	4.9%	3.5%	0.4%

References

(1) Ministry of Economy, Trade and Industry Agency for Natural Resources and Energy: "2013 fiscal year The annual report on energy (Energy White Paper 2014)", pp. 179–218 (2010).
(2) K. Tajima and T. Sato, *J. Magn. Soc. Jpn.*, Vol. 34, No. 3, pp. 367–373 (2010).
(3) T. Miyaji, K. Tajima, T. Taniguchi and T. Sato, *J. Magn. Soc. Jpn.*, Vol. 27, No. 9, pp. 976–981 (2003).
(4) K. Tajima, M. Hattori, T. Miyaji, T. Sato, and Y. Sakamoto, *J. Magn. Soc. Jpn.,* Vol. 29, No. 6, pp. 680–685 (2005).
(5) T. Umesaka, K. Tajima, and Y. Yoshida, The papers of Technical Meeting on Magnetics, *IEE Jpn*, MAG-15-116 (2015).
(6) S. Hayakawa, K. Nakamura, S. Akatsuka, T. Aoki, M. Kawakami, T. Ohinata, K. Minazawa, and O. Ichinokura, *J. Magn. Soc. Jpn.* 28, 425 (2004)

<Paper>

Heat generation of core–shell particles composed of biodegradable polymer and iron oxide

C. Oka, K. Ushimaru, N. Horiishi*, T. Tsuge, and Y. Kitamoto

Interdisciplinary Graduate School of Science and Engineering, Tokyo Institute of Technology, 4259 Nagatsuta-cho, Midori-ku, Yokohama 226-8503, Japan
*Bengala Techno Lab., 1-19 Kodai, Miyamae-ku, Kawasaki 216-0007, Japan

A suspension of core–shell particles composed of a biodegradable polymer core and iron oxide nanoparticles (IONPs) exhibits higher heat generation under an alternating magnetic field compared with a suspension of IONPs at the same IONP concentration. The improvement of the heat generation will be attributed to the change of the strength of dipolar interactions between adjacent IONPs. The IONPs in the core–shell particles were relatively isolated, in contrast with that in IONP suspension before the formation of the core–shell particles. Therefore, in the core–shell particles, the dipolar interaction is reduced, and the heat-generating capability is increased. This explanation is brought through investigating the influence of the agglomerate size of IONPs on the heat-generating capability.

Key words: magnetic hyperthermia, core–shell particle, iron oxide nanoparticle, dipolar interaction, hydrodynamic diameter, delta *M* plots

1. Introduction

Magnetic hyperthermia (thermotherapy), which kills cancer cells by heat generated from magnetic nanoparticles under alternating magnetic fields, is a type of cancer treatment under study in clinical trials[1]~[4]. In the magnetic hyperthermia, tumor tissues are exclusively affected by selective accumulation of the magnetic nanoparticles, which are heat agents, in the tissues. Hence, the magnetic hyperthermia has been attracting significant attentions as a more effective treatment than conventional hyperthermia methods; a lot of researchers have been investigating magnetic nanoparticles and an apparatus generating the magnetic field for the treatment to improve the efficiency[5]~[11].

In our previous study, a core–shell particle composed of a core of a biodegradable polymer particle and a shell of assembly of magnetic iron oxide nanoparticles (IONPs) has been prepared as a candidate for a drug carrier for magnetically guided drug delivery system (MGDDS)[12]. It can load hydrophobic drugs into its polymer core. We have already confirmed that the core–shell particles were strongly attracted to a NdFeB magnet, and will have magnetic properties enough for MGDDS.

In the present study, heat generation of the core–shell particles in the alternating magnetic field is investigated. The core–shell particle can act as a heat agent for magnetic hyperthermia as well as a MGDDS carrier because its structure includes magnetic nanoparticles. Therefore, the core–shell particle is expected to be a promising carrier having hybrid function of a drug carrier and a heat agent. The heat agent is an assembly of IONPs as a shell; the assembled structure of the IONP-shell is controlled by the
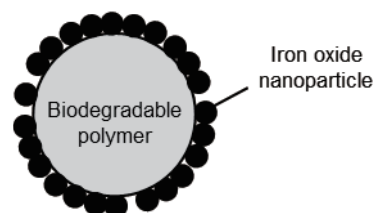

Fig. 1 Schematic illustration of core–shell particle composed of biodegradable polymer and iron oxide nanoparticles.

preparation conditions. The heat generation is induced by relaxation losses of IONPs, which are Néel and Brownian relaxation losses, and the relaxation dynamics is greatly affected by their agglomerate state due to dipolar interactions between IONPs[13],[14]. To discuss the heat-generating capability of the core–shell particles in view of the agglomerate status in their suspension, the capability was compared with that of IONP suspensions with various agglomerate sizes manipulated by adding a flocculant and by changing IONP concentrations.

2. Experimental

Two types of IONPs, whose sizes were 8 nm and 11 nm, were synthesized by a coprecipitation method using $FeCl_2$, $FeCl_3$ and NaOH. Blocking temperatures of the IONPs were about 240 K for the 8 nm IONPs, and higher than room temperature for the 11 nm IONPs at a powder state. Although the temperature of the 11 nm IONPs indicates being ferromagnetic, both of the IONPs seem to be superparamagnetic in these suspensions at the room temperature. The core–shell particles were prepared as reported in our previous report with the 8 nm IONPs[12]. To evaluate the heat-generating

capability, suspensions of the core–shell particles, the 8 nm IONPs, and the 11 nm IONPs were prepared at IONP concentrations of 0.1, 0.3, 0.5, 1, 1.5, and 2.0 mg Fe/mL. The IONP concentrations were determined by a concentration of Fe in the suspension. The agglomerate status, in particular, the size of the 11 nm IONPs was manipulated by adding polyvinyl alcohol (PVA) as a flocculant to the IONP suspension.

The heating curves of the suspensions were measured by a system with a coil generating the magnetic field at a frequency of 2 MHz and a field strength of 3.4 kA/m$_{rms}$, and temperature was measured with a fiber-optic thermometer. Since the frequency is considerably high, it is presumed that the Néel relaxation is dominant rather than the Brownian relaxation in the condition. The heat-generating capability was evaluated by the Box-Lucas equation[15]:

$$T(t) = T(0) + A(1 - e^{-Bt}) \qquad (1)$$

where T is temperature, t is time, and A and B are parameters related to the saturation temperature and the curvature of the heating curve. At $t = 0$, the product $A{\times}B$ represents an initial rate of temperature rise $\Delta T/\Delta t$. The specific absorption rate (SAR) is proportional to the product, expressed as

$$SAR = (\Delta T / \Delta t)\,(C/m_{Fe}) \propto AB \qquad (2)$$

where C is the heat capacity per unit mass of a specimen and m_{Fe} is the Fe mass per unit mass of a specimen. Therefore, the values of $A{\times}B$ were calculated from the heating curves of the suspensions of the core–shell particles and the IONPs as a substitute for SAR.

To elucidate the difference in magnetic interaction between IONPs and the core-shell particles, zero-field cooled (ZFC) and field cooled (FC) magnetization, isothermal remanent magnetization (IRM) and direct current demagnetization (DCD) of the 8 nm IONPs and the core-shell particles using the IONPs were measured. The ZFC and FC measurements were conducted at 8.0 kA/m from 5 K to 320 K. The IRM and DCD were measured at 5 K for delta M plots[16]. The IRM was obtained by the following protocol; 1) starting from a state of zero remanence, 2) applying a field, and 3) measuring magnetization (M_r) after decreasing the field to zero. For the DCD, the protocol was 1) saturating the specimen in a positive field, 2) applying a negative field, and 3) measuring magnetization (M_d) after increasing the field to zero. M_rs and M_ds were obtained by changing the applying field in each process. The magnitude of the applying fields was from 12.0 kA/m to 638 kA/m, and the field for the saturation was 798 kA/m. The delta M (ΔM) plots can be obtained by the following equation[16];

$$\Delta M = M_d - (1 - 2M_r) \qquad (3)$$

The ΔM expresses the degree of a deviation from a system without any magnetic interaction between magnetic nanoparticles. Generally, negative ΔM represents dipolar-like (demagnetizing) interactions, and positive ΔM indicates exchange-like (magnetizing) interactions.

3. Results and discussion

The capability of a suspension of the core–shell particles was superior to that of the 8 nm IONPs prepared at the same IONP concentration, which was 0.3 mg Fe/mL. Figure 2 shows heating curves of the suspensions, and Table 1 lists the product $A{\times}B$ calculated from the fitting parameters of these curves. The product was approximately doubled by the formation of the core–shell particles. We speculated this improvement would be induced by the change of the agglomerate state of IONPs. Indeed, the agglomerate state of IONPs in its suspension seemed considerably different from that in the core–shell particles. In the IONP suspension, IONPs agglomerate, resulting in the formation of a secondary particle; the hydrodynamic diameter measured by dynamic laser scattering (DLS) was 79 nm. On the other hand, the IONPs on the core–shell particles relatively exist with a gap and the assembled size is equal to the size of the core–shell particle as apparently observed in a TEM image of Fig. 3.

Table 1 Hydrodynamic diameter and the product $A{\times}B$ of fitting parameters for suspensions of 8 nm IONPs, and core–shell particles prepared using the 8 nm IONPs.

	Hydrodynamic diameter (nm)	$A \times B$ per Fe mass (K/(s·g Fe))
8 nm IONPs	79	37
Core-shell particles	-	64

Fig. 2 Heating curves of 0.3 mg Fe/mL of suspensions of 8 nm IONPs, and core–shell particles prepared using the 8 nm IONPs.

Therefore, we focus on agglomerate state, in particular, on the agglomerate size of IONPs as a parameter to strongly influence the heat generation in order to discuss the above-mentioned improvement of the capability in the core–shell particles. The 11 nm IONPs were employed for this experiment instead of the 8 nm IONPs to obtain larger amount of the heat generated from IONPs. The agglomerate size was manipulated by adding PVA. We selected a hydrodynamic diameter in the suspensions measured by DLS as a parameter strongly correlated with the agglomerate size. Open circles in Fig. 4 represent the hydrodynamic diameter of the 11 nm IONPs at PVA concentration of 0, 0.1, 0.2, 0.5, and 1.0 wt%. The diameter was increased with the increase of PVA concentration. The IONP concentration was 0.3 mg Fe/mL.

Figure 5(a) shows heating curves of the IONP suspensions with different concentrations of PVA. The curves were changed by an amount of PVA. However, it was found that the heat generation under the alternating magnetic field was observed even in PVA

aqueous solutions (aq.) without the IONPs as shown in Fig. 5(b). The heating of the PVA aq. would be caused by an eddy current loss[17),18)]. The temperature rise depends on the PVA concentration. Therefore, we drew new curves subtracting the temperature rise of PVA aq. from heating curves of IONP suspensions, so as to estimate the heat generation induced only by IONPs. Figure 5(c) shows the recalculated curves, and filled circles in Fig. 4 indicate the products $A \times B$ of these fitting parameters. The product was decreased with the

Fig. 3 TEM image of core–shell particle prepared using 8 nm IONPs.
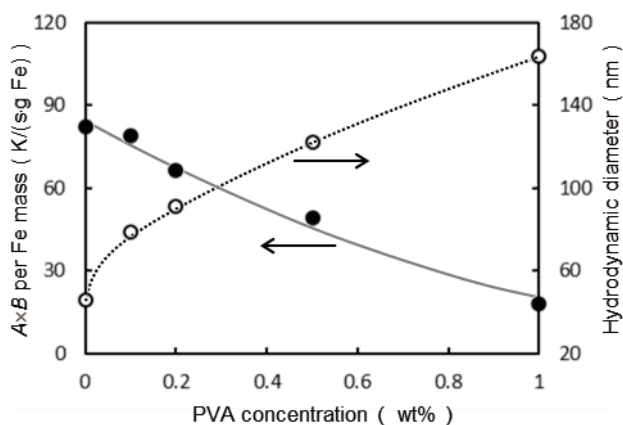
Fig. 4 Dependences of the product $A \times B$ (filled circles) and hydrodynamic diameter (open circles) of 11 nm IONPs on PVA concentration of the IONP suspension.
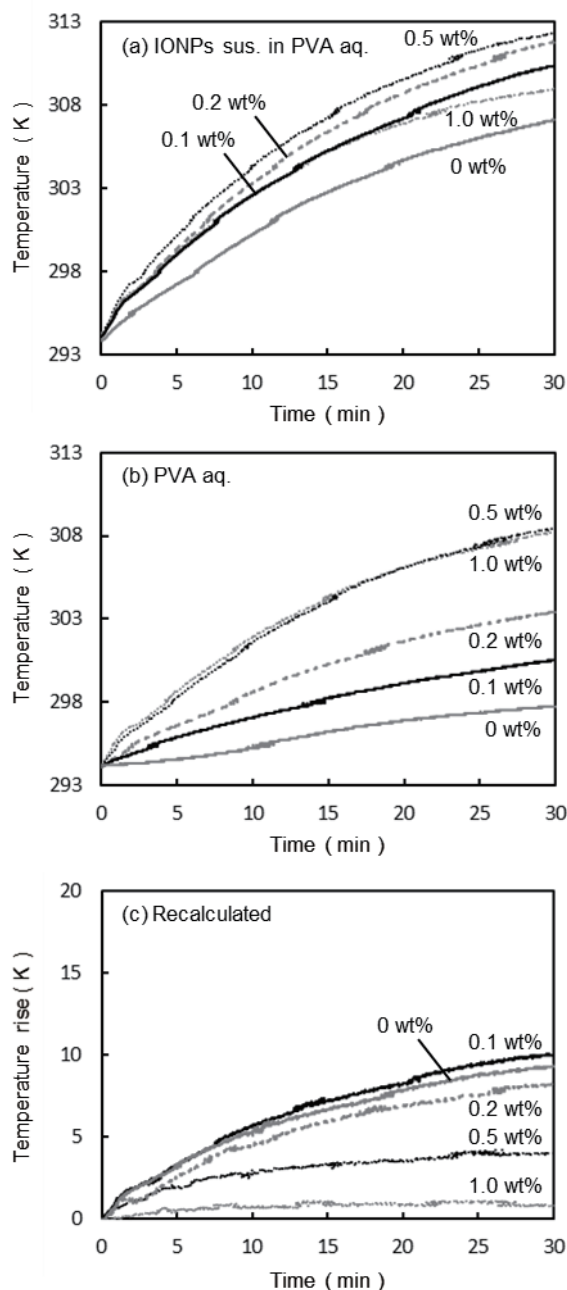
Fig. 5 Heating curves of (a) IONP suspensions prepared at different PVA concentrations, (b) PVA aqueous solutions at different concentrations without IONPs, and (c) curves recalculated by subtracting (b) from (a).

increase of the PVA concentration. This result suggests that the heat-generating capability is reduced by the agglomeration.

To corroborate the results about the negative influence of the agglomeration of IONPs on the heating capability, the heating capability of IONP suspensions with different IONP concentrations were evaluated. The agglomerate size of IONPs can be regulated not only by adding the flocculant such as PVA but also by changing the concentration of IONPs in the suspension based on DLVO theory. Hence, the IONP suspensions were prepared at different IONP concentrations. The hydrodynamic diameter was increased with the increase of the concentration as shown in Fig. 6 (open circles). These heating curves after removing the heating effect of the solvent are shown in Fig. 7. The curves were drawn by subtracting the heating of water, which is the same as the result of 0 wt% PVA aq. in Fig. 5(b). The product of the fitting parameters of the recalculated curves is indicated in Fig. 6 (filled circles). The product decreased exponentially with the IONP concentration. The product $A{\times}B$ is proportional to SAR. Therefore, this result indicates that the heat-generating capability of IONPs is reduced by the agglomeration induced by increasing the concentration of IONPs. The decrease of SAR at high concentrations has also been demonstrated in other papers[13),19),20)].

Figure 8 represents the relationship between the hydrodynamic diameter of IONPs and the product of the fitting parameters; the relationship was obtained from the dependences of the hydrodynamic diameter and the product on the PVA concentration and IONP concentration seen in Figs. 4 and 6. The product obviously exhibits a linear decrease against the increase of the diameter, indicating the reduction of the heating capability with the increase of the agglomerate size. The tendency has also been reported by other researchers although the reason has been unclear[21)]. In addition, the relationship from the PVA-concentration dependence (open circles) emerged above that from the IONP-concentration dependence (filled circles). Because the hydrodynamic diameter of IONPs with PVA was evaluated to be larger than that without PVA due to the existence of PVA, which was a hydrophilic polymer.

The reduction of the capability was probably related to dipolar interactions between adjacent IONPs in the agglomerate. Some researchers have reported that the dipolar interaction has a negative influence on SAR, and three dimensional cluster of magnetic nanoparticles exhibited the reduction of the heat generation[22),23)]. We speculate the reason why the interaction will become greater with the increment of the agglomerate size of IONPs in the following. One IONP in a larger agglomerate interacts magnetically with more other IONPs than that in a smaller agglomerate, resulting in the increase of dipolar interactions. Therefore, the heat generation was reduced with the increase of the agglomerate size of IONPs leading to the increase of
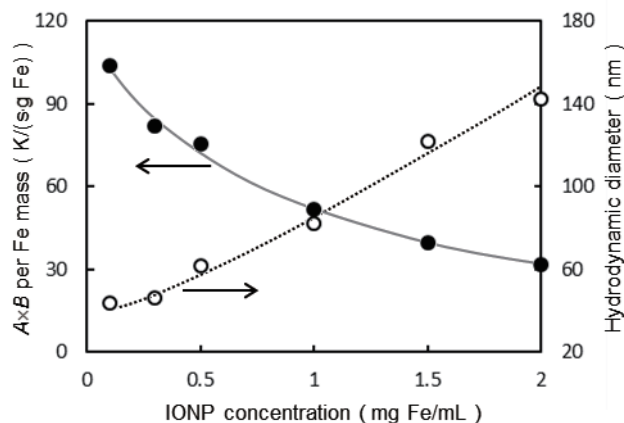

Fig. 6 Dependences of the product $A{\times}B$ (filled circles) and hydrodynamic diameter (open circles) of 11 nm IONPs on IONP concentration of its suspension.
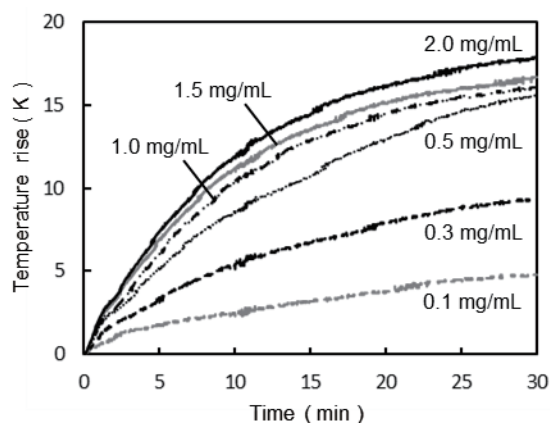

Fig. 7 Heating curves of IONP suspensions of different IONP concentrations after removing the heating effect of the solvent, that is the curves subtracting temperature rise of water.
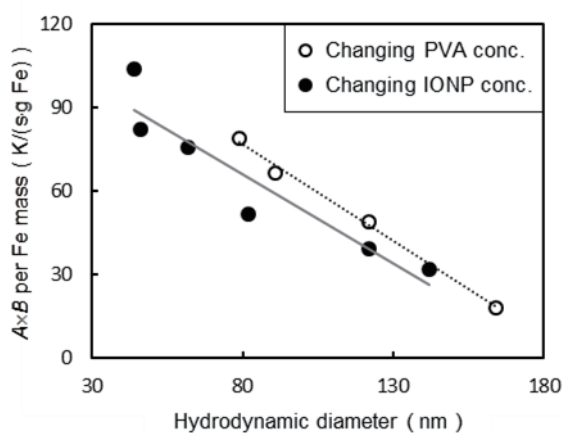

Fig. 8 The product $A{\times}B$ as a function of hydrodynamic diameter of IONPs in its suspensions changing PVA concentrations (open circles) and IONP concentrations (filled circles).

number of IONPs which one IONP interacted with.

We speculate that the improvement of the heat-generating capability by the formation of the core–shell particles seen in Fig. 2 and Table 1 was induced by a change of their agglomerate state of IONPs. The IONPs were deposited on the biodegradable polymer core with a gap between each IONP in the core–shell particles. Whereas the assembly of IONPs is a two-dimensional cluster in the core–shell particles, the agglomerate of IONPs is a three-dimensional cluster in the IONP suspension, because the IONPs spontaneously agglomerate in order to reduce surface energy. The number of IONPs interacting with one IONP in the core–shell particles is less than that in the agglomerate of IONPs, which is the three-dimensional cluster of IONPs. Thus, dipolar interactions in the core–shell particles are weaker than in the agglomerate of IONPs, resulting in the improvement of the heat-generating capability. Figure 9 shows ZFC-FC curves of the core-shell particles and the 8 nm IONPs. It indicates that magnetic property of the core-shell particles is obviously different from the 8 nm IONPs.
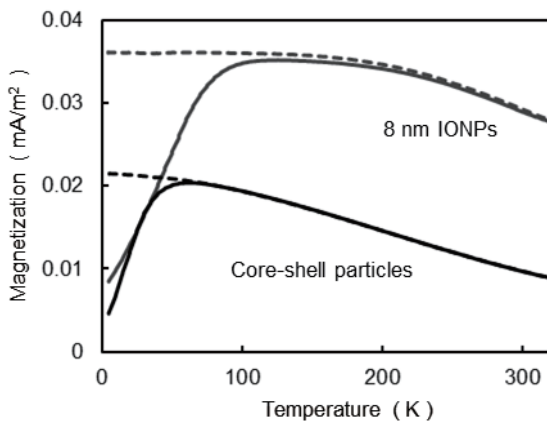
Fig. 9 ZFC (solid line)-FC (dotted line) curves of core-shell particles and 8 nm IONPs.
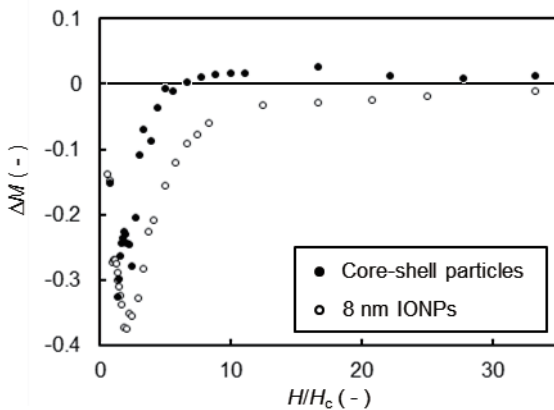
Fig. 10 Delta M plots for core-shell particles and 8 nm IONPs. H_c is coercivity at 5 K.

An energy barrier to magnetization reversal in the 8nm IONPs seems to be larger in consequence of strong agglomeration. Figure 10 exhibits delta M plots obtained from IRM and DCD measurements[16]. The magnitude of ΔM represents the degree of the magnetic interaction, and it is always zero in a system of non-interacting particles according to the Wohlfarth relationship. The maximum of the deviation from zero in ΔM was −0.33 for the core-shell particles, which was smaller than −0.38 for the 8 nm IONPs. The magnetic interaction, that is probably the dipolar interaction, was restrained by the formation of the shell assembly of the IONPs.

4. Conclusion

The heat-generating capability of the core–shell particles composed of the biodegradable polymer core and the iron oxide nanoparticles was discussed in the present paper. The capability of the core–shell particles was superior to that of the original IONPs used for the formation of the core–shell particles. The improvement by the formation of the core–shell particles were explained in view of the agglomerate state of magnetic IONPs correlating to dipolar interaction. We demonstrated that the heat-generating capability is inversely proportional to the hydrodynamic diameter, in other words, the agglomerate size of IONPs in the suspension. The dependence on the agglomerate size is probably explained by the number of IONPs interacting in the agglomerate. Finally, we concluded the higher capability of the core–shell particles was brought from the difference in the agglomerate state of IONPs between the core–shell particles and the original IONP suspension.

References

1) Q. A. Pankhurst, J. Connolly, S. K. Jones, and J. Dobson: *J. Phys D*, **36**, R167 (2003).
2) R. Hergt, R. Hiergeist, I. Hilger, W. A. kaiser, Y. Lapatnikov, S. Margel, and U. Richter: *J. Magn. Magn. Mat.*, **270**, 345 (2004).
3) B. Thiesen, and A. Jordan: *Int. J. Hyperthermia*, **24**, 467 (2008).
4) A. Jordan, R. Scholz, P. Wust, H. Fahling, and R. Felix: *J. Magn. Magn. Mat.*, **201**, 413 (1999).
5) C. P. Gooneratne, M. Kakikawa, T. Ueno, and S. Yamada: *J. Magn. Soc. Jpn,*. **34**, 119 (2010).
6) S. Vasseur, E. Duguet, J. Portier, G. Goglio, S. Mornet, E. Hadova, K. knizek, M. Marysko, P. Veverka, and E. Pollert: *J. Magn. Magn. Mat.*, **302**, 315 (2006).
7) S. Maenosono, and S. Saita: *IEEE Trans. Magn.*, **42**, 1638 (2006).
8) B. Mehdaoui, A. Meffre, J. Carrey, S. Lachaize, L. M. Lacroix, M. Gougeon, B. Chaoudret, and M. Respaud: *Adv. Funct. Mat.*, **21**, 4573 (2011).

9) S. Balivada, R. S. Rachakatla, H. Wang, T. N. Samarakoon, R. K. Dani, M. Pyle, F. O. Kroh, B. Walker, X. Leaym, O. B. Koper, M. Tamura, V. Chikan, S. H. Bossmann, and D. L. Troyer: BMC cancer, **10**, 119 (2010).

10) L. M. Lacroix, R. B. Malaki, J. Carrey, S. Lachaize, M. Reapaud, G. F. Goya, and B. Chaudret: *J. Appl. Phys.*, **105**, 023911 (2009).

11) C. C. Berry, and A. S. G. Curtis: J. Phys. D, **36**, 198 (2003).

12) C. Oka, K. Ushimaru, N. Horiishi, T. Tsuge, and Y. Kitamoto: *J. Magn. Magn. Mat.*, **381**, 278 (2015).

13) E. Lima, E. D. Biasi, M. V. Mansilla, M. E. Saleta, M. Granada, H. E. Troiani, F. B. Effenberger, L. M. Rossi, H. R. Rechenberg, and R. D. Zysler: *J. Phys. D*, **46**, 045002 (2013).

14) A. Roch, Y. Gossuin, R. N. Muller, and P. Gillis: *J. Magn. Magn. Mat.*, **293**, 532 (2005).

15) M. Kallumadil, M. Tada, T. Nakagawa, M. Abe, P. Southern, and Q. A. Pankhurst: *J. Magn. Magn. Mat.*, **321**, 1509 (2009).

16) C. B. Andujar, D. Ortega, P. Southern, Q. A. Pankhurst, and N. T. K. Thanh, *Nanoscale*, **7**, 1768 (2015).

17) S. A. Theron, E. Zussman, and A. L. Yarin, *Polymer*, **45**, 2017 (2004).

18) F. Liu, S. Crozier, H. Zhao, and B. Lawrence, *Concept. Magnetic Res.*, **15**, 26 (2002).

19) C. M. Boubeta, K. Simeonidis, A. Makridis, M. Angelakeris, O. Iglesias, P. Guardia, A. Cabot, L. Yedra, S. Estrade, F. Peiro, Z. Saghi, P. A. Midgley, I. C. Leboran, D. Serantes, and D. Baldomir: *Sci. Rep.*, **3**, 1652 (2013).

20) A. Urtizberea, E. natividad, A. Arizaga, M. Castro, and A. Mediano: *J. Phys. Chem.*, **114**, 4916 (2010).

21) X. Wang, H. Gu, and Z. Yang: *J. Magn. Magn. Mat.*, **293**, 334 (2005).

22) L. C. Branquinho, M. S. Carriao, A. S. Costa, N. Zufelato, M. H. Sousa, R. Miotto, R. Ivkov, and A. F. Bakuzis: *Sci. Rep.*, **3**, 2887 (2013).

23) D. Serantes, K. Simeonidis, M. Angelakeris, O. C. Fesenko, M. Marciello, M. P. Morales, D. Baldomir, and C. M. Boubeta: *J. Phys Chem.*, **118**, 5927 (2014).

Notice for Photocopying

複写をされる方へ